POLITECNICO DI TORINO

Corso di Laurea Magistrale in Ingegneria Civile

Tesi di Laurea Magistrale

Validation of time of liquefaction prediction models from geotechnical centrifuge tests results

Relatori

Prof. Sebastiano Foti

Prof. Antònio Viana da Fonseca

Prof. Sara Rios

Dott. Maxime Millen

Studente

Giuseppe Mudanò

Ottobre 2019

TABLE OF CONTENTS

AKNOWLEDGEMENTS

This work has been produced under the activities in the University of Porto (FEUP) of the LIQUEFACT project, and has received funding from the European Union Horizon 2020 research and innovation programme under the grant agreement No GAP-700748.

I would first like to thank Prof. Sara Rios for all the time she dedicated to me and for all the endless advice she gave me during the whole realization of this document. Her kindness and humanity have been the base of my inspiration during the writing of my thesis, and I will never forget her limitless patience and passion in supervising me.

A very special gratitude goes out to Prof. Antonio Viana da Fonseca for the exceptional hospitality. I deeply appreciated the way he spent his time in order to make my experience in the university of Porto as fulfilling as possible. I will always remember his advice, and thank him for his reassurance and humour which accompanied the crucial moments of my work.

I am grateful to Prof. Sebastiano Foti for having given me the opportunity to take this exciting path abroad. I thank him for the passion and all the things he taught me in the “Soil dynamics” course. The background knowledge he gave during his classes has been crucial for the analysis performed in this work.

I must express my profound gratitude to Dr. Maxim Millen, whose role in this document has been extremely fundamental. Despite being on the other side of the world, his valuable knowledge was kindly made available to me in the crucial points of the data analysis. For this reason, I owe him a big thank you.

Immense recognition goes to my family, especially my parents, Nino and Cettina, for the trust and love they give me, which are the basis of every single step I make.

I will always carry in my heart all the kind people I met during my experience in Portugal, all the friends I made, who, among other things, have made me fall in love with this beautiful country.

And finally, last but by no means least, my thanks also go to my lifetime friends. I have always appreciated their deep affection and I am sure they will still support me in every single step I will make in the future.

ABSTRACT

Recent events have demonstrated that Earthquake Induced Liquefaction Disasters are responsible for significant economic and social losses. Unfortunately, while the causes of liquefaction triggering are known, the accurate prediction of its occurrence is not always possible and, also, mitigations techniques still need to be implemented in order to reduce the consequences of the liquefaction triggering.

In this context, results from a set of thirty-seven centrifuge tests carried out at ISMGEO are treated in depth. On each test, consisting in a reduced-scale physical model, the behaviour of a real soil deposit subjected to a seismic motion is simulated and, thus, liquefaction triggering conditions can be analysed. The soil response to the seismic motion is described through the analysis of three main variables, corresponding to the three types of sensors used in the models: acceleration, pore pressure and settlements.

An analysis of the ground motion change with the increase of pore pressure is performed through the analysis of the *Fourier amplification function* and the *S-transform*. In fact, if high values of the pore pressure ratio are reached during the motion, the *FAF* is modified in amplitude and frequency content: the peaks are attenuated and translated towards low values of frequency. The mentioned drop of the high frequency content is also observed on the Stockwell transformation function along the time.

From the pore pressure analysis, it was observed that the prototype initial pore pressure distribution is, in all the cases, smaller than the theoretical hydrostatic one due to the difference between the top and the bottom acceleration of the centrifuge box. The pore pressure ratio in free field was also compared to the cases with mitigation measures. For instance, in the case of horizontal drains, it was observed that the pore pressure amplitude peaks are halved and a sudden decrease of the pore pressure peak values along the vertical axis in the box is generated. Finally, the presence of seepage toward the top of the model was verified explaining some trends of the pore pressure distribution along depth.

Concerning the settlement, the effectiveness of the mitigation techniques in terms of settlements attenuation is also analysed. The settlement in presence of mitigation measures is observed to be up to one third compared to the one occurred in absence of countermeasures.

Two simplified pore pressure models are analysed and compared with the centrifuge data, the Strain Energy Based Method (SEBM), proposed by Millen et al. (2019), and the Stress Based Method (SBM), proposed by Seed et al. (1975). Both methods are also analysed separately along their calibrations in order to ascertain their accuracy. Since these methods do not take into account seepage that might occur during the earthquake this subject is also discussed when comparing the pore pressure predicted by these methods with the centrifuge results.

SYMBOLS AND ACRONYMS

In this section a list of simbols and abbreviations used on the thesis are shown. In some cases, the same symbol could represent different meanings, depending on the context in which it is emplyed.

Latin Letters

a – Scale parameter for the number of uniform cycles

b – Scale parameter for the number of uniform cycles

C_Q – Normalization factor of the cone resistance

D_R – Relative densities

e_c – Critical void ratio

f – Frequency

f – Parameter employed on the calculation of kσ depending on the relative densities and the age of the soil

g – gravity acceleration

G_0 – Initial Stiffness modulus

Δh - Hydraulic head

i – Hydraulic gradient

I_c – Index of soil behaviour

k – Calibration parameter depending on the soil type

k_c – Corrective parameter for the tip resistance

k_σ – Corrective parameter for the vertical effective stress

k_0 – Coefficient of earth pressure at rest

l – Lenght

M - Magnitude

n_{liq} – Number of uniform cycles at which liquefaction occurs

N – Scale factor fo the centrifuge acceleration

N – Number of equivalent cycles

N_L – Number of cycles needed to liquefy a soil sample

p_a – athomospheric pressure

q_c – Tip resistance on CPT test

q_{1cN} – Normalized tip resistance

r – radial distance form the epicenter of the earthquake

r_d – Reduction coefficient for the depth

r_u – Pore pressure ratio

S_r – Strain factor

t – time [s]

u –Pore pressure

$\ddot{u}$ – Seismic acceleration

Δu – Pore pressure excess

V_S – Shear wave velocity

W – Strain energy

ΔW – Dissipated energy

z – Depth

A - Shear wave aplitude

Greek letters

α – Coefficient employed in the calculation of r_d

β – Coefficient employed in the calculation of r_d

β – Coefficient employed in the calculation of r_u

ε – Deformation

σ – Pressure

σ' - Effective stress

τ – Shear stress

γ – Shear strain

ρ – volumic mass [kg/m^3]

ω – Angular frequency [rad/s^{-1}]

γ_w – Volumic weight of the water

λ – Reduction factor of the Stiffness Modulus

χ – Error

Abbreviations

BPT – Becker Penetration Test

CE – Correct Estimations

CPT – Cone Penetration Test

CRM – Centrifuge Reduced Model

CRR – Ciclic Resistance Ratio

CSR – Ciclic Stress Ratio

ESB – Equivalent Shear Beam

FAF – Fourier Amplification Function

FC – Fine Content

FEUP – Faculdade de Engenharia da Universidade do Porto

FS – Safety factor

GM – Ground Motion

IPS – Induced Partial Saturation

ISMGEO - Instituto Sperimentale Modelli Geotecnici

LL – Liquid Limit

MSF – Magnitude Scale Factor

NCASE – Normalised Cumulative Absolute Strain Energy

NSE – Normalized Strain Energy

OCR – Over Consolidation Ratio

PEC – Pseudo-Energy Capacity

PPT – Pore Pressure Transducer

PGA – Peak Ground Acceleration

SBM – Stress Based Method

SEBM – Strain-Energy Based Method

SPT – Standard Penetration Test

1. INTRODUCTION

1.1 Preface

Earthquake-induced soil liquefaction is the main responsible for significative economic loss as well as social during recent earthquake (Kobe in Japan, Christchurch in New Zealand, Adapazary in Turkey); in fact, it has been recently observed that earthquake-induced liquefaction disasters are often responsible for half of the economic loss cause by the earthquake (Airoldi et al., 2018).

Nowadays, the causes of the liquefaction triggering are well known. Unfortunately, an accurate assessment of where liquefaction is likely to happen is not fully recognised, as well as an estimation of what the liquefaction consequences may be. More complete knowledge of the liquefaction consequences would be crucial for the development of the appropriate mitigation techniques to deal with the triggering of the phenomenon.

Basing on this background, LIQUEFACT project, financed by the European Commission in commission to the Horizon program 2020, aims to contribute to reduce the Liquefaction induced damage by adopting a holistic approach to recognise the factors that contribute to the occurring of liquefaction. In this context, an in-depth study of the phenomenon is performed: the analysis provides a complete description of the phenomenon, including the effectiveness of mitigation measure or the presence of a building in the soil deposit. One of many studies carried out in this project, constituted in the execution of centrifuge tests, will be the subject of analysis in the present work.

1.2 Executive summary, objectives and goal of this document

The aim of this document is to treat in depth data resulting from physical geotechnical modelling activities performed at the ISMGEO (Istituto Sperimentale Modelli Geotecnici, formerly ISMES- Italy) laboratory in the frame of LIQUEFACT project, Work Package 4, Task 4.2, “Small scale centrifuge modelling”.

Particularly, a set of thirty-seven centrifuge tests is analysed, each one consisting in a reduced-scale model, i.e. a physical model which can simulate the behaviour of a real soil

deposit (prototype). Also, the application of a cyclic shaking at the base of the model allows to reproduce the seismic response of a site and, thus, to analyse the triggering of liquefaction.

Having said that, after the results have been converted, they are singularly analysed and then compared with the objectives listed below:

- produce a database of results converted to prototype units to be used as a benchmark for future analyses;
- analyse the alteration of the ground motion passing through a liquified soil (local seismic response);
- characterize the use of drains and IPS (Induces Partial Saturation) as a countermeasure and explore possibility of optimising the performance by varying the geometry and the location of the mitigation measure;
- study the pore water behaviour, i.e. the increase of the pore pressure and the water flow inside different soil deposits;
- show and comment liquefaction-induced settlement in different soil conditions;
- compare the evolution of pore pressure observed in different centrifuge tests with the correspondent pore pressure values obtained by simplified methods.

1.3 Layout of the thesis

The first chapter of this theses addresses the importance of liquefaction and the objective of this analyses, in the scope of the liquefaction studies that have been done since its discovery.

In the second chapter, it is explained in depth the phenomenon of liquefaction as well as its preponderating factors. There is at first a characterization of liquefaction, followed by a distinction of the main liquefaction phenomenon, static and cyclic, being that the ladder is further explained as it is the focus of the thesis. Then it is explained the behaviour of different soils under cyclic stress. Liquefaction susceptibility and its consequences are also addressed and explained, as well as some mitigation techniques. Finally, the methods to assess liquefaction triggering that will be used in Chapter 5 are enumerated and explained in depth.

The third chapter serves to clarify and simplify the several denominations and assumptions needed to understand the following chapters. In this chapter the centrifuge machine and the

several model details (soil properties, soil profiles, structural properties, sensors, mitigation techniques and input ground motions) are described and explained.

In the fourth chapter, it is done a validation of the centrifuge model through a pore pressure analyses and it is analysed the effect that the different model parameters have on the pore-pressure, acceleration and displacement variations between tests.

In the fifth chapter there is a validation of the Strain energy based method and the Stress based method, by analysing the pore pressure evolution of these methods and correlating them to the centrifuge reduced model results.

2. LIQUEFACTION

2.1 Historical field evidence

” […] Giungemmo in una larga pianura, che dianzi vi esisteva, incontrammo un ruinoso rivolgimento di sabbia e di arena. Erasi squarciato l’antico suolo ...Ciò che noi credemmo a prima vista un’avventura particolare e circoscritta, tosto vedemmo che era un’alterazione, divenuta comune a tutta l’antica pianura e ciò in un’estensione molto significante.”

The previous lines are reported from Michele Sarconi’s book named “Istoria”, in which the Italian scholar describes the consequences produced by the series of 5 earthquakes occurred in the south of Italy between the 5th of February and the 28th of March 1783. The writer is depicting an image of huge sandy mass noticed during the exploration of the areas affected by the shocks. The landscape of Piana di Gioia Tauro (Calabria), initially formed by large flat lands, was upset by the earthquake and, particularly, many sandy accumulations covered the original appearance of the zone (Figure 2.1). The phenomenon described in the previous lines, naturally, remained unexplained at the time; nowadays, it is well known that Sarconi was dealing with a clear example of a sandy soil liquefaction.

Figure 2.1-Sand boils on Mesima riverside, Calabria (Istoria)

Looking at more recent earthquakes, many disastrous events have been caused by liquefaction. It is definitively noteworthy to mention the liquefaction phenomenon following the Niigata (1964) earthquake (Richter magnitude 7.5) during which several buildings tilted despite of their robustness under the seismic point of view (rigid frames); indeed, these building were founded on saturated sandy deposits which were entirely subjected to liquefaction. During

the same seismic event the Showa Bridge's pile foundation, founded on a coarse-grained soil, moved due the lateral spreading (Figure 2.2).

(a)

(b)

Figure 2.2- (a) Tilting of apartment buildings, Niigata (1964). (b) Showa bridge's pile foundations moved due to lateral spreading, Niigata (1964)

The liquefaction was also the cause of sand boils appearance during the famous earthquakes of El Centro (1979, USA), Guatemala (1979) and Christchurch (New Zeeland, 2011). In fact, when such strong earthquakes occur the confined sand in pressure is able to create a fissure in the upper layer (silty and/or clayey) and thought that hole reaches the surface forming a volcano-shaped accumulation (Figure 2.3).

(a)  (b)  (c) 

Figure 2.3- (a) Sand boils in El Centro, USA (1979). (b) Sand boils in Guatemala (1979). (c) Sand boils in Christchurch, New Zealand (2011)

2.1.1 Liquefaction in Italy

Many cases of liquefaction affected Italy in the past along its whole extension with a peak in the eastern coast of Sicily and in the south-east part of the peninsula.

The homogeneous diffusion of liquefaction phenomena was completely mutated by the disastrous earthquake occurred in Emilia Romagna on the 20th of May 2012. The earthquake produced many soil liquefaction phenomena, particularly in the area between Reggio Emilia and Ferrara where the soils are predominantly sandy of alluvial origin and thus with a high liquefaction susceptibility. As a consequence of the event many buildings were damaged, and a huge area was covered by sand and lime coming from the underground. Furthermore, it was possible to observe phenomena such as soil swelling, significant settlements, soils cracks linked with lateral spreading as well as lifting of many sidewalks.

That event attested the high susceptibility of some zones in the Italian territory to liquefy and enhanced the importance of studying the techniques to limit its consequences.

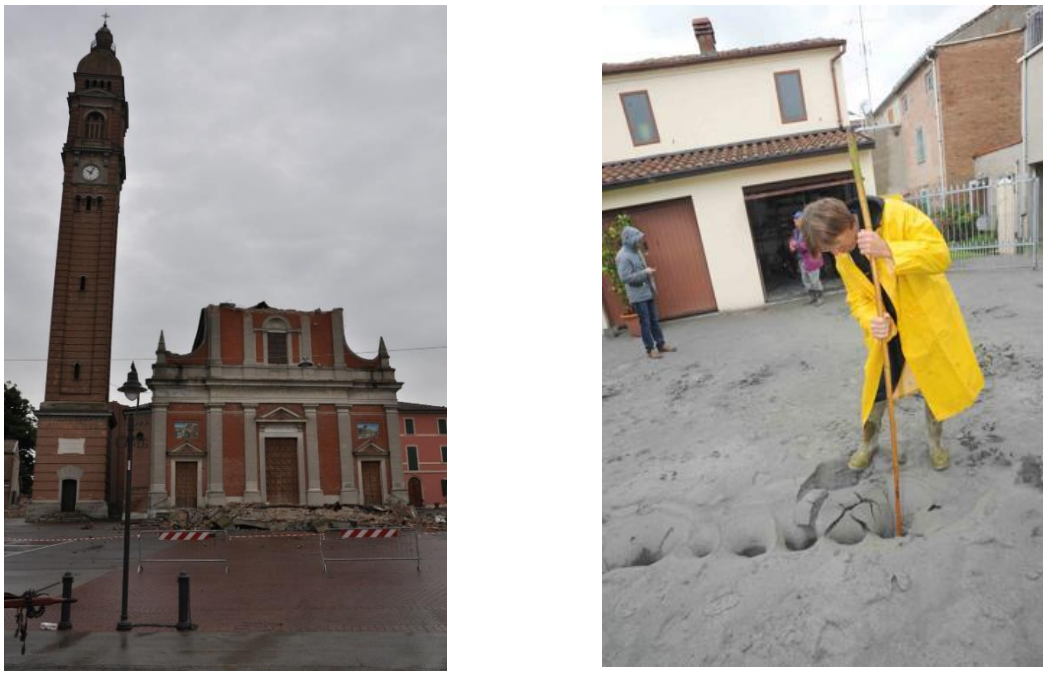

(a) (b)

Figure 2.4- (a) Church damaged by liquefaction on the undelaying soil. (Emilia-Romagna, 2012). (b) Urban area covered by sand coming from the underground (Emilia-Romagna).

2.2 Description of the phenomena

2.2.1 Introduction

The term “liquefaction” in its broad sense refers to the phenomenon that can occur in saturated coarse-grained soils subjected to static or cyclic shear stresses.

Liquefaction phenomena can be divided into two main categories: static liquefaction and cyclic liquefaction, depending if the liquefaction is triggered by static or cyclic stresses. (Kramer, 1996).

Liquefaction can also be divided in flow liquefaction and cyclic mobility. In the first, which can be triggered by both static or cyclic stresses, there is a quick collapse of soil masses and conveyance of this masses for large distances. In the latter the deformations can occur without complete reduction of effective stresses. The phenomena, called lateral spreading, can occur on very gentle sloping or natural discontinuities and can produce displacement of variable amplitude (Kramer, 1996).

2.2.2 Static liquefaction

Static liquefaction is a well-known phenomenon related to the soil behaviour under monotonic semi-static load conditions. The mentioned phenomenon occurs in undrained conditions and, therefore, it is a sudden event.

The occurring of static liquefaction can be followed by large deformations when the shear stress required for static equilibrium of the soil mass is greater than the shear strength of the soil in its liquified state. This can be a case of flow liquefaction.

As mentioned above, these failures are coupled with huge consequences, such as quick collapses of soil masses and conveyance of this masses for large distances. One of the most important historical events connected to flow liquefaction is the collapses of the Lower San Fernando Dam, its consequences are showed in Figure 2.5.

Figure 2.5- Collapse of the St. Francis dam, 1928 (Los Angeles Times, 2003)

2.2.3 Cyclic liquefaction

Cyclic liquefaction indicates the partial or total loss of bearing capacity of a soil subject to cyclic shear stresses. Particularly, the ground motion generates an increase of the pore pressure which can nullify the shear resistance of a saturated coarse-grained soil.

The behaviour of a loose sandy soil sample subjected to a cyclic stress is analysed to clarify the way in which liquefaction happens. The earthquake is represented as a ground motion acting on the base of the sample. Geostatic conditions are reduced as soon as the motion affects the

portion of soil. As a result of this cyclic action the soil tends to reduce the voids until e_{min} is reached and thus a denser structure is obtained after the shock (Figure 2.6).

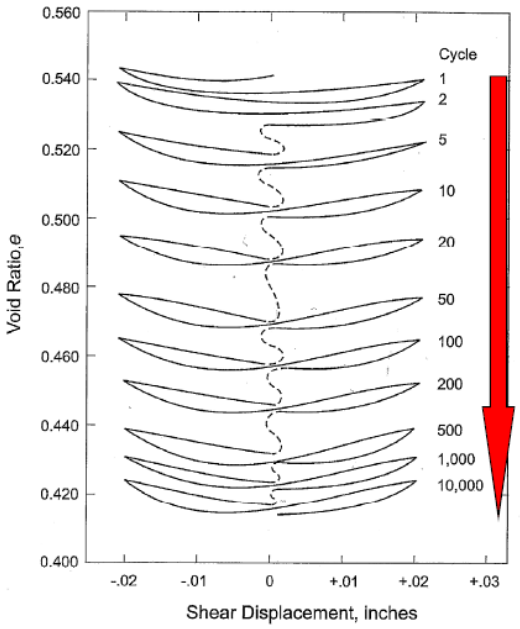

Figure 2.6- Densification path of a loose sand (Youd et al., 1972)

The same procedure is described for a saturated soil sample. It is possible to notice that under a slow static or semi-static process the water would have enough time to get out of the sample and the pore pressure would be dissipated; since a high frequency event is described the fluid does not have the ability to escape from the pores during the motion. In this case the densification process is obstructed by the interstitial fluid, thus the water forms a kinematic constraint (Figure 2.7).

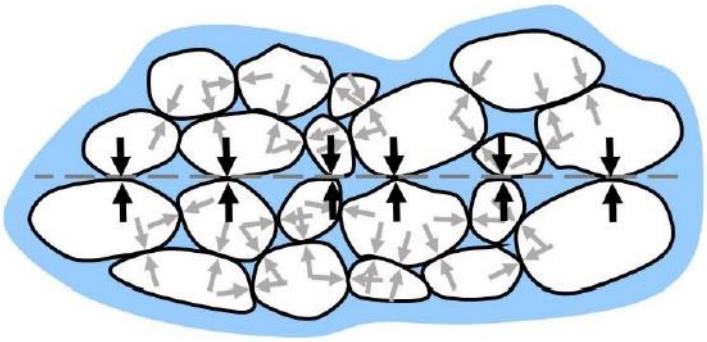

Figure 2.7- Densification is prevented due to pore pressure (NASEM, 2015)

The pore pressure of the fluid rises, which prevents the immediate densification of the sand:

$$u = u_0 + \Delta u \tag{1}$$

Because of the pore pressure increase, the contact stresses among the grains decrease as well as the effective stress:

$$\sigma' = \sigma_{tot} - u \tag{2}$$

According to Terzaghi's Principle the stiffness and the resistance of the soil are linked to the effective stresses; thus, as soon as the final pore pressure matches the total stresses ($u = \sigma$), the bearing capacity of the soil becomes null, and liquefaction condition is reached:

$$u = \sigma \tag{3}$$

$$\sigma' = 0 \tag{4}$$

In liquified soils, the particles cannot sustain the load anymore since they are not in contact and therefore the soil behaves as a fluid. The shear resistance of a coarse-grained material in its geostatic condition is:

$$\tau_R = \sigma' \cdot tan\Phi' \tag{5}$$

In a liquified state the effective stress is null and the shear resistance will be zero as well, such as the resistance of a fluid.

When the seismic event is over, the excess of pore pressure dissipates, and the geostatic condition is restored but not in the same exact conditions as the final void ratio is now smaller. The amount of time in which the soil remains in liquified conditions depends on the drainage conditions and on the duration of the shock. Moreover, that amount of time rises with the increase of the thickness of the sandy deposit and the fineness of the sand, hence its permeability.

Finally, even if the soil recovers the stiffness, the damages on the superstructures are permanent, since the reduction in void ratio led to surface settlements. For this reason, precautions against liquefaction must be carried out.

In the following paragraphs the term "liquefaction" will be exclusively referred to the cyclic phenomenon linked to seismic events. Anyway, a short description of static liquefaction will be provided in the lines below.

2.3 Behaviour of the sands under cyclic stresses

2.3.1 Introduction

The behaviour of loose and dense sands under torsional cyclic stresses can be observed in laboratory tests carried out on soil samples with different densities. Particularly, results of torsional shear tests on isotropically consolidated soils are described in this section.

To correctly describe the behaviour of the sample approaching to the failure envelope a division is necessary in this topic: medium loose sand, very loose sands and dense sands are separately analysed. Particularly, the behaviour of a medium loose soil will be shown to be half way between a dense and a very loose sandy soil. The distinction will be based on the behaviour

once instability condition is reached, i.e. when the amplitude of the shear strain increase considerably at constant load amplitude.

Finally, clayey soils cannot liquefy because the electrochemical bonds between their particles avoid the volume reduction during the ground motion.

2.3.2 Behaviour of medium loose sands ($D_R = 50\%$)

The pore pressure increases steadily each cycle in the initial phase, while effective stress is decreasing. After a certain number of cycles, the instability condition (phase transformation point) is reached and the soil stiffness starts to decrease more and more each cycle; during this phase, the soil turns from a contractive behaviour to a dilative one and a quick fluctuating increase of the pore pressure can be observed (Figure 2.8a). When the instability point is crossed, the sample quickly reaches quickly the failure line, hence it moves to the origin in few cycles (Figure 2.8b). As soon as the stress path reaches the origin, the sample liquefies, as $\sigma_v' = 0$ and $r_u = 1$ (where $r_u = {\Delta u}/{\sigma_v'}$).

The shear strain maintains a small value during the stable section of the test up to the point of instability, where the strain level is much higher cycle by cycle (Figure 2.8d), due to the stiffness drop.

It is also interesting to describe the path of the sample on the $\tau - \gamma$ plane (Figure 2.8d): the soil shows a quasi-linear response during the initial part; in the instable part, the linear behaviour moves to a hysteretic one. In this phase, the soil stiffness increases and decreases within each loading cycle, i.e. it becomes lower when the effective stress is low and then increases significantly as the effective stress increases and soil dilates. The result is a succession of closed curves characterized by a quasi-horizontal initial part and an increase of the strain amplitude cycle by cycle: a horizontal initial part is associated to a value of the shear modulus G close to 0, since it can be also seen as the slope of shear-strain curve. Moreover, the increase of the strain amplitude produces an enlargement cycle by cycle of the close area enclose by the shear-strain curve, thus, the damping ratio D increases during the test (*NASEM*, 2016).

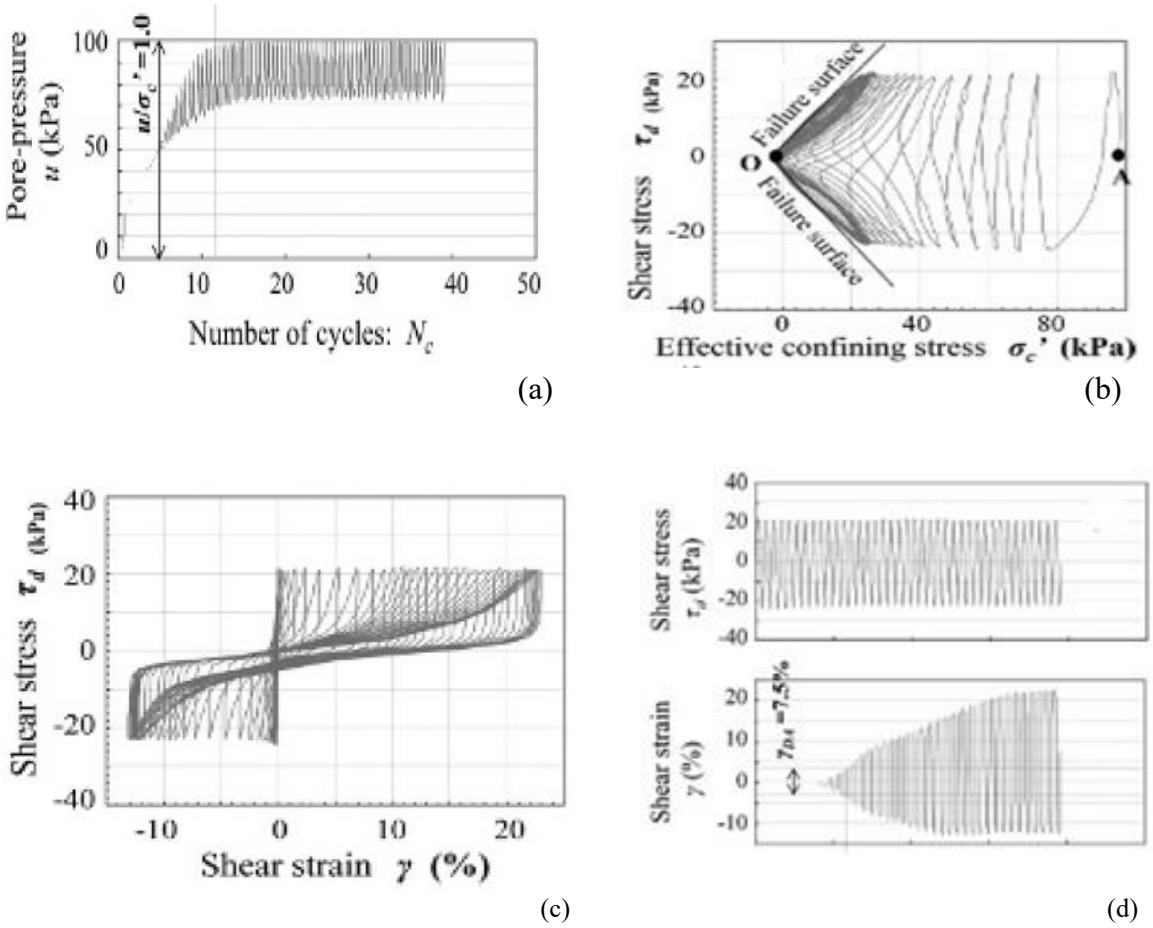

Figure 2.8-Torsional shear test in clean sands (Dr=50%): (a) Pore pressure trend. (b) Effective stress-path. (c) Stress-strain curve. (d) Stress and strain paths (Kusaka, 2012)

2.3.3 Behaviour of a very loose soil ($D_R = 30\%$)

Very loose soils, such as clean sands looser than D_r =30% or sands not so loose but containing a lot of non-plastic fines, tend to be contractive without positive dilatancy under high effective confining stresses, developing fully or partially flowtype failures like liquid. In very contractive soils, soil specimens in test devices tend to be nonuniform during undrained shearing (loosening or forming the water film at the top of the specimen) due to "void redistribution'', making soil element tests on uniform specimens almost meaningless. (Kokusho, 2017).

2.3.4 Behaviour of dense soils ($D_R = 75\%$)

While liquefaction failure can occur in only few cycles in a loose specimen subjected to cyclic shear stresses, thousands of cycles may be required to cause liquefaction failure of a dense specimen. In fact, in this case, as soon as the sample tends to reduce its volume the dilation take place. The occurring of the dilative behaviour generate a negative pore pressure, which is opposed to the positive one caused by contraction. In this case the excess of pore pressure Δu will come near to the soil effective stress σ_v' , then the ratio r_u will decrease due to dilative behaviour and the sample will move away from the liquefaction condition (Kokusho, 2017), as shown in Figure 2.9.

The amplitude of the strain will rise in steady state conditions during the whole duration of the test.

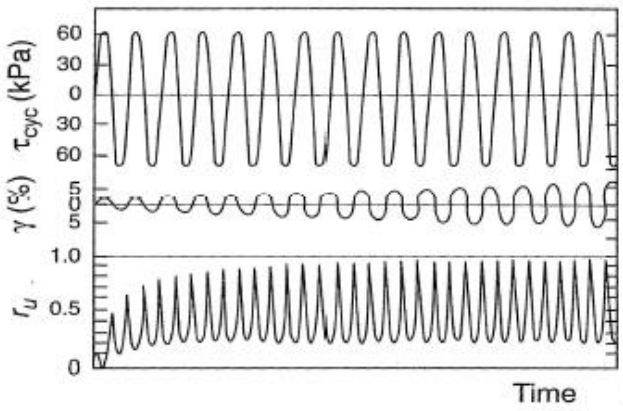

Figure 2.9- Dense sands (Dr=75%): stress-path, strain path and ru trend along time (Kramer, 1996)

2.4 Liquefaction susceptibility

2.4.1 Introduction

Looking at the liquefaction events occurred in the past it is possible to notice that not all the soils are subject to the described phenomenon during a seismic event. In fact, liquefaction occurs only in certain soil type and soil conditions. A set of criteria establishing if a soil could be affected by liquefaction are discussed in the following. Accordingly, if a site is not predisposed to liquefy, the designer is exempted from undertaking the liquefaction hazard assessment. The available criteria to provide a preliminary estimation of the liquefaction hazard

are related to the characteristics of the investigated deposit, particularly to its history, geology, composition and state.

2.4.2 Historical criteria

The first criterion for the liquefaction hazard assessing is the historical one. According to it, all the soils affected to the phenomenon in the past have a high susceptibility to liquefy again in the future. Moreover, it was shown that liquefaction damages are confined within a recurrent distance of the seismic source. In this regard, Ambraseys (1988) carried out a research comparing the epicentral distance and the moment magnitude of earthquakes which took the soil into a liquefied condition (Figure 2.10). Although such assessment is ineffective for a punctual analysis, it can be helpful to undertake a regional scale evaluation (Kramer, 1996).

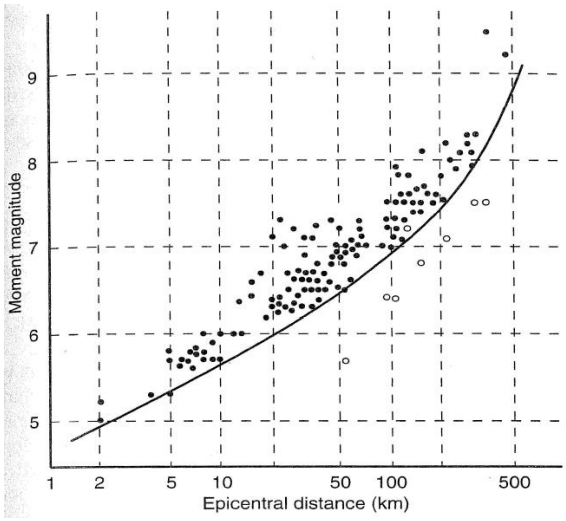

Figure 2.10-Relationship between limiting epicentral distance in sites at which liquefaction has been observed and moment magnitude (Ambraseys,1988)

2.4.3 Geologic criteria

As it will be shown in this paragraph, soil liquefaction is highly influenced by the local geology of a soil. In fact, the depositional environment, the hydrological environment and the age of a deposit are head factors in the assessment of liquefaction hazard. (Youd and Hoose, 1977)

Regarding the depositional process, soil characterized by a uniform grain size assortment are more prone to liquefy. In fact, a uniform grain size distribution implies a higher minimum

void ratio, i.e. a contractive behaviour when subject to shear forces. Therefore, fluvial deposits as well as colluvial and aeolian ones are the most affected by the phenomenon (Kramer, 1996).

The age of the deposit is also a key aspect in the risk evaluation: older soil deposits are less prone to liquefy due to higher degree of compaction usually associated to its old age.

Concerning the hydrological conditions, as previously explained, the presence of the groundwater level close to the ground surface is essential for the occurring of soil liquefaction; thus, attention must be paid to constantly saturated soils and deposits with a fluctuating groundwater level.

Finally, human-made deposits deserve more caution. In fact, these are likely the most susceptible, especially when poorly compacted (Kramer, 1996).

2.4.4 Compositional criteria

Liquefaction triggering is associated with the tendency of a soil to reduce its volume under shear stresses. For this reason, compositional characteristics and particles shape associated with a volume instability are often coupled with a high liquefaction susceptibility. As previously mentioned, sandy deposits are the most prone to reduce their volume during shearing. However, liquefaction of silty soils has been also observed in the past by Ishihara (1984). This is justified by the fact that the occurring of the phenomenon is also related to the plasticity index, thus, silty soils can liquefy if cohesionless and non-plastic. Clays remain anyway non-susceptible to liquefaction, thus only the fine-grained soils which satisfy the following Chinese criteria (Wang, 1979) can be considered susceptible:

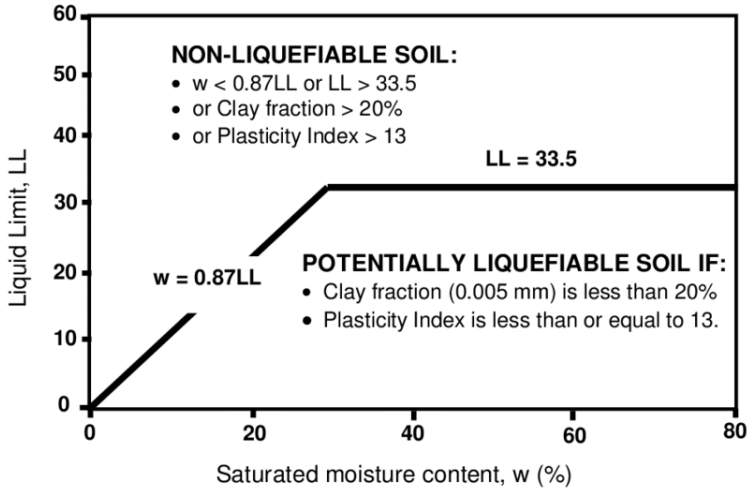

Figure 2.11- Chinese Criteria (Wang, 1979)

Fraction finer than $0.005\ mm \leq 15\%$

Liquid limit , $LL \leq 35\%$

Natural water content $\geq 0.9LL$

Liquidity index ≤ 0.75

This criterion was demonstrated to be ineffective by Bray and Sancio (2006). In fact, looking at the consequences of the most recent earthquakes, an alternative liquefaction assessment criterion was proposed in terms of soil composition. According to it, in order to be susceptible a soil must show:

Plasticity index $IP \leq 12$

Natural water content $w_n \leq 0.85LL$

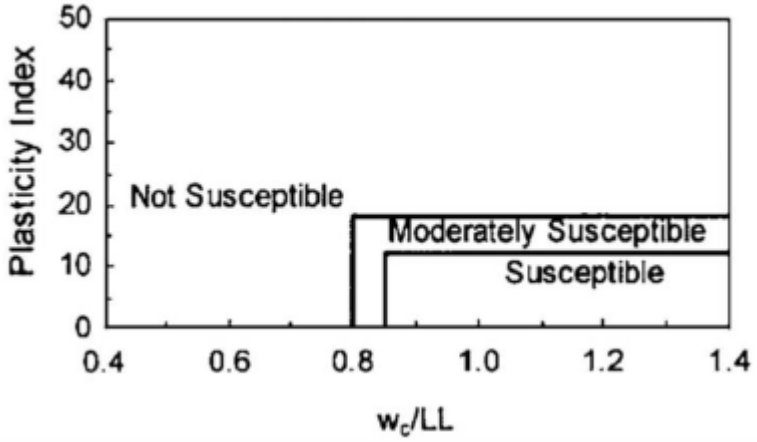

Figure 2.12- Liquefaction susceptibility criteria proposed by Bray and Sancio (2006)

Concerning gravelly soils, several cases of liquefaction have been notified in the past. Thus, if impermeable topping layer obstruct the pore pressure excess dissipation, a gravelly soil must be considered as susceptible.

The particles graduation also plays an important role in the assessment. Indeed, a heterogeneous grain size distribution reduces the liquefaction hazard, since the small particles fill the soil voids, reducing the volume instability.

Finally, liquefaction susceptibility is influenced by particles shape, since rounded particles are more prone to densify than the sharped one (Kramer, 1996).

2.4.5 State criteria

The last criterion to establish the susceptibility to liquefaction of a sandy soil is related to its state, since not every sandy soil tends to reduce its volume during a cyclic shear force. According to the critical state theory the soil behaviour can be related to its initial state parameters, i.e. the void index and the initial stress state. Consequently, the critical state curve, in Figure 2.13, will separate the graph into two zones: the area above the curve will present soils with a tendency to contract during the earthquake and so with a high tendency to liquefy, while the soils in the area below the curve will show a dilating behaviour during the ground motion with a higher resistance against liquefaction (Kramer, 1996).

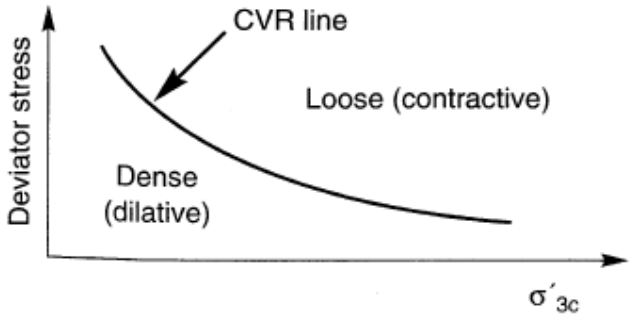

Figure 2.13- Use of CVR line as a boundary between dilative and compressive behaviour (Kramer, 1996)

2.5 Consequences of liquefaction triggering

2.5.1 Introduction

The analysis of the consequences of the liquefaction phenomena which occurred in the past provide a valid starting point to estimate its possible damages.

An evident example of this working process is given by the survey results along a national road passing through a liquified soil, provided by Kokusho and Fujita (2002). The analysed road section, founded on a area subjected to an extensive liquefaction during Niigata earthquake, presents a difference in elevation of one meter, i.e. measured in the same point before and after the seismic event.

As it is remarked in the previous example, a first relevant consequence of liquefaction is the existence of large settlements.

In this section different ways in which the liquefaction triggering can change the initial appearance of a site will be shown. Particularly, a frequent phenomenon related to soil instability will be described: it is known as lateral spreading. As it will be shown, the occurring of this phenomenon produce massive soil deformation, which can bring to the sinking or tilting of heavy structures as well as failures of retaining walls or floating of light structures.

It will be also possible to observe that a ground motion passing through a liquefied soil changes its natural time history appearance.

Finally, a description of sand boils will be provided, despite their almost negligible significance under an engineering point of view.

2.5.2 Settlement of saturated sands

The liquefaction-induced settlement is not a sudden occurrence, since it occurs only after the end of the seismic event, when the pore pressure excess in the soil layer can is dissipated. The time frame needed to reach the equilibrium condition depends on three main factors: the permeability of a soil, its compressibility and the length of the drainage path; thus, the pore pressure excess can take many hours to reach a null value. Anyway, giving an exact estimation of the liquefaction-induced settlement is a difficult task. Basically, the settlement of the ground surface is related to the volumetric variation of the several layers constituting the deposit. This approximate estimation gives an error which can range from 25% to 50% of the total estimation. For this reason, the liquefaction-induced settlement calculation should be only used to have an order of magnitude of the damages that a structure on the ground surface can suffer and not to have a certain datum available for the design (Foti et al., 2009).

Ishihara and Yoshimine (1992) related the entire settlement of a deposit with the level of damage on the overlying structure. The result obtained are showed in Table 2.1.

Level of damage	Settlemet [cm]	Phenomena observed on the ground surface
From negligible to null	0÷10	Reduced cracks
Medium	10÷30	Small cracks, small sandy spills
High	30÷70	Large cracks, significant sandy spills

Table 2.1- Effects of liquefaction-induced settlements on the overlying structures (Ishihara and Yoshimine, 1992)

For the liquefaction-induced settlement calculation the empirical method proposed by Tokimatsu and Seed (1987) is described as representative. The methods are based on the fact that the settlement depends on:

- *Relative density* D_r: a loose material has a higher tendency to reduce its volume during the seismic motion;

- *Shear deformation* γ: it is a measure of the ground motion intensity;
- *Excess of pore pressure* Δu*:* as it is said previously, the settlement is directly related to the dissipation of the pore pressure excess;

Since it is difficult to deal with laboratory samples, all the previous properties are summarized in the value $(N_1)_{60}$ and $CSR_{7.5}$, which entities will be discussed in the following. To have a closer correlation between the mentioned properties and the empirical results many seismic phenomena occurring in several soil types were observed, as well as many laboratory experiments were carried out.

The resulting chart for the estimation of volumetric strain in saturated sands from cyclic stress ratio and standard penetration resistance is shown in Figure 2.14.

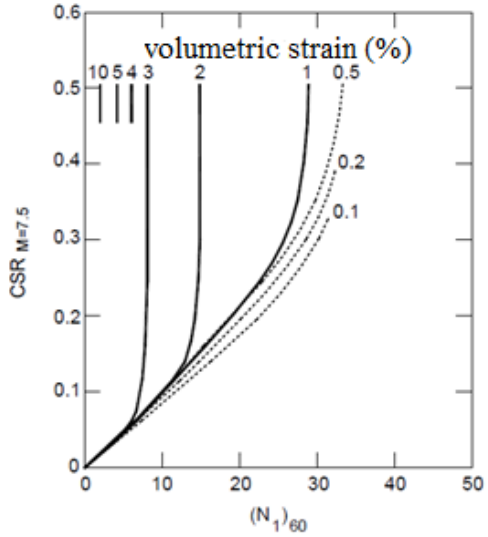

Figure 2.14- Relationship between volumetric strain, $CSR_{7.5}$ and $(N1)_{60}$, adapted Tokimatsu and Seed (1987)

It was observed that volumetric strain can range from 2 to 3% for medium-loose sands, it can be higher for very loose ones. Once volumetric strain is obtained, the settlement is deduced by integrating the volumetric strain on the thickness of each layer.

In order to have a representative value of $(N_1)_{60}$ in each section, the practical procedure requires the division of the analysed soil layer into several sublayers and, then, extend the calculation of the volumetric strain to all the sublayers. The final step consists to multiply all the obtained volume deformations times the thickness of the correspondent sublayers.

Recently, other methods to estimate settlements have been proposed by Karamitros, Bouckovalas, & Chaloulos, (2013) and Bray & Macedo (2017); however, it is worth to notice

that, if sand boils are produced during the ground motion, post-earthquake settlements are likely to be irregular (Kramer, 1996).

2.5.3 Lateral spreading

Lateral spreading is a phenomenon closely connected to liquefaction, which should always be considered when soil liquefaction hazard is evaluated.

Several cases of lateral spreading have been observed in the past, coupled with damage levels ranging from null to high. As well as most of the effects of liquefaction phenomena, it is caused by the soil shear strength degradation induced to the soil by liquefaction. In fact, it occurs when, during the seismic event, the shear strength of the liquified soil get to a number below the value of the shear stresses required for the equilibrium. When this instable state is reached large masses of soil are affected by significant deformations. These displacements increase during the earthquake until a stable configuration is restored (Kramer, 1996).

Lateral spreading can occur on lightly sloping grounds or in presence of lateral discontinuities in the environment, such as flat ground adjacent to a water source.

When human-made constructions are founded on a deposit affected to lateral spreading large damages are produced (figure 2.15).

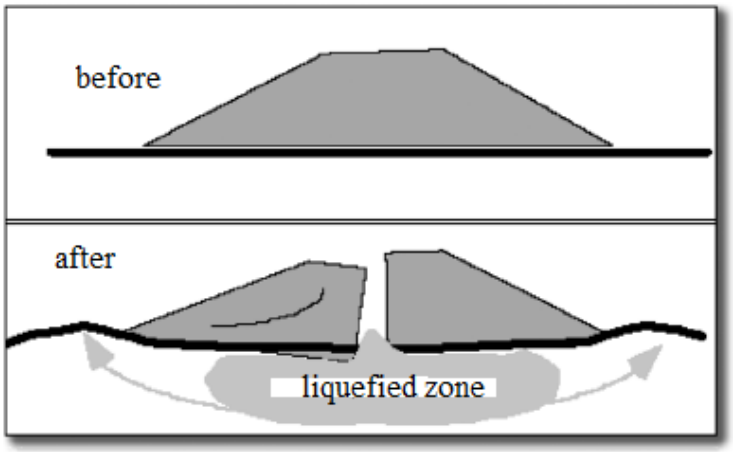

Figure 2.15- Lateral spreading in a road embankment
(http://www.ce.washington.edu/~liquefaction/html/main.html)

A famous disaster closely related to lateral spreading is represented by the failure of San Fernando Dam, in 1971. Lateral spreading was also the reason of many other events, such as the failure of Showa Bridge's pile foundation (Figure 2.16) during Niigata earthquake, in 1964.

Figure 2.16- Failure of Showa bridge's piles foundation (Tokimatsu et al., 2014)

It is relevant to note that, as well as in the settlement calculation, only empirical methods are available for the estimation of deformation. Thus, large uncertainties are always implicit on the evaluation methods.

2.5.4 Alteration of the ground motion

It is well known in the soil dynamics that a softer soil deposit responds differently to the ground motion compared to a stiffer one. Moreover, a deposit of liquefiable soil which is relatively stiff at the beginning of the earthquake becomes softer at the end of the motion; as it is known, this behaviour is due to the degradation of the *shear modulus* G (Figure 2.17), contemporaneous with the increase in the shear deformation γ induced by the motion and the decreasing of the vertical effective stresses σ'_v. The immediate consequence of the shear modulus degradation in the *Fourier Amplification Function* (*FAF*) is the translation of the peaks of towards lower values of frequency (Figure 2.18). This translation is due to the proportionality between the frequency peak values *f* of the function and the *shear waves velocity* V_s, which in turn is proportional to G_0 ; thus, the softer is the soil, the more to the left the peaks will be shifted in the *FAF*. It could happen that the vertical effective stress decrease as much as the high frequency components are zeroed by the transfer function.

Furthermore, the decreasing in the soil stiffness is followed by an increase of the *damping ratio D.* Since the *FA* function is $f(1/D)$, the increasing of γ generates a decreasing in the amplitude of the motion amplification. Anyway, it is difficult to give a quantitative value of the amplification produced by a specific site.

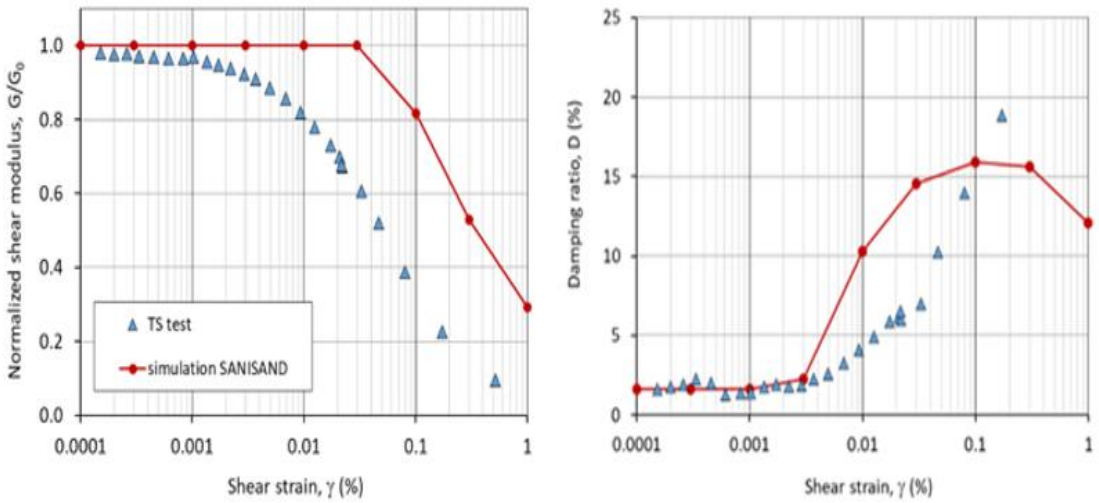

Figure 2.17- Shear modulus degradation model and Damping ratio model (Airoldi et al., 2018)

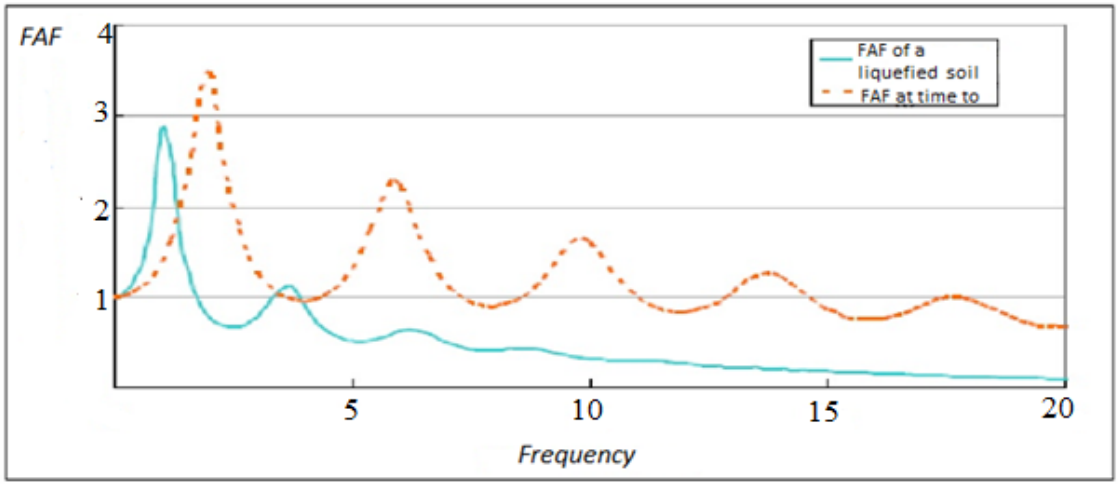

Figure 2.18- Fourier Amplification function pre and post liquefaction triggering

The most significant example which explains how the liquefaction modify the aspect of the ground motion is given by the accelerometer located near an apartment building in 1964 Niigata earthquake. Figure 2.19 clearly shows that the aspect of the time series changes dramatically 7 seconds after the beginning of the motion, i.e. as soon as liquefaction occurs. This recording is a representative case in which the vertical effective stress decrease as much as the transfer function makes null all the high frequency components (Kramer, 1996).

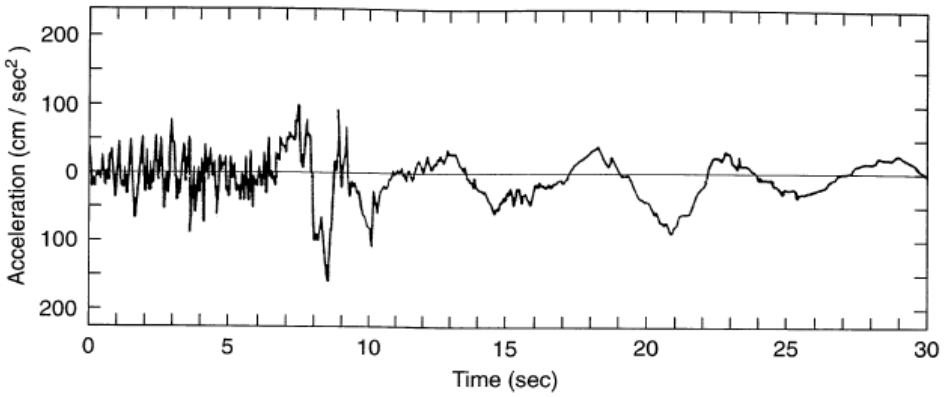

Figure 2.19- Accelerogram near apartment building resting on liquefiable soil in Niigata earthquake,1964 (After Aki, 1988).

Subsequently, Youd and Carter (2005) found amplified values of the motion in frequencies in the range $1 \div 1{,}5\ Hz$, analysing results obtained from acceleration series from liquefied soils. On the other hand, Gingery et al. (2015) found amplification peaks in frequencies around $20\ Hz$. This phenomenon is associated with the dilative part of the soil behaviour. In fact, as aforementioned, the soil shows a stiffening part when the dilation occurs.

Unfortunately, the limited field data and analytical studies on the effect of liquefaction on the ground motion do not provide enough information for the development of a simplified empirical or semiempirical approach to properly predict the effect of liquefaction on site response, either before or after the triggering.

Finally, even if we are dealing with a partially liquefied soil, the fact that the peak of *FAF* is reduced does not imply a reduction in the damages; in fact, the amplification of the low frequency components implies the occurrence of large cyclic oscillations in the deposit. These displacements could cause large damages on buried structures or pile foundation embedded on the liquefied soil. The occurrence of liquefaction in a soil layer underlying a thinner superficial layer could also produce a decoupling of the relative displacement between the two layers. The result is the formation of several blocks in the superficial soil, separated by fissures of variable spacing (Kramer, 1996).

2.5.5 Sand boils

As it has been previously explained, settlements are a consequence of the excess pore pressure dissipation. A different consequence, discontinuous in the space, will be described in this subchapter, i.e. the sand boils generation.

During the shaking, the pore pressure in the liquefiable soil builds up and, if a high level is reached, the liquefied soil can flow through the fine-grained layer, reaching the surface. Anyway, if the impermeable layer is thicker enough to avoid the liquid flow, sand boils will not appear in the surface, even if the sand is in a complete liquified state. On the contrary, the presence of sand boils has been observed in the case of a thin superficial fine-grained layer and a pore pressure in the deeper sandy soil far from value of the initial vertical stress, $r_u \approx 80\%$ (Kramer, 1996).

The afore explained concept is graphically represented by Ishihara in Figure 2.20, which relates the relative thickness of the sandy soil and the clayey layer with an index of the hazard level, such as the peak value of the acceleration a_{max}.

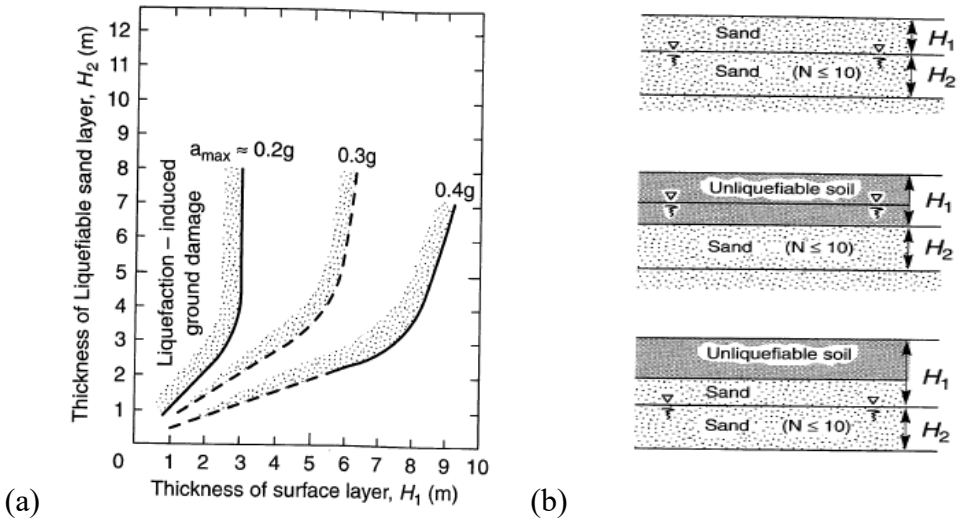

Figure 2.20- (a) Relationship between thickness of liquefiable layer and thickness of overlaying layer at sites for which surface manifestation of level-ground liquefaction has been observed, and (b) guides to evaluation od respective layer thickness, (ishihara, 1985)

As it has been previously said, sand boils are of little engineering significance by themselves; however, they represent a significant index of the pore pressure excess level. An example of sand boil accumulation on the surface is shown in Figure 2.21.

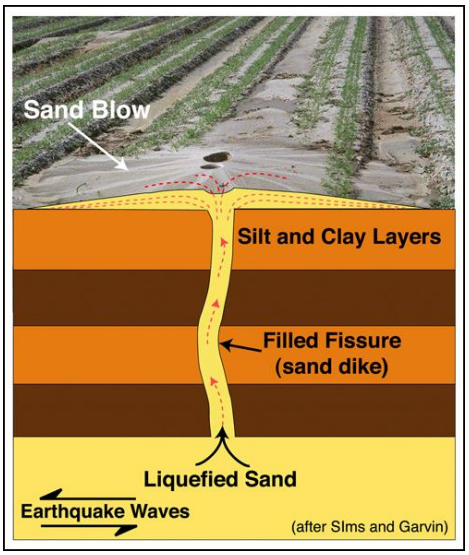

Figure 2.21- Sand boil (modified from Sims and Garvin, 1995)

A meaningful example is shown in the image below, it is possible to observe a 30 cm-layer of sand coming from sand boils in the site of San Carlo (Emilia -Romagna).

Figure 2.22- 30cm- layer of sand coming from sand boils in the site of San Carlo, Emilia- Romagna (Airoldi et al., 2018)

2.6 Mitigation measures

2.6.1 Introduction

Every time the safety factor against liquefaction (*FSL*) does not reach a safe value, i.e. the liquefaction is expected in a large soil layer, some mitigation measures against should be carried out.

Nowadays, several measures to oppose the occurring of liquefaction are available. The first one described is related to the design of structures to resist to the liquefaction-induced settlements, which produce to the partial loss of bearing capacity of the underlaying layer.

Then, techniques to reinforce the liquefiable soil will be mentioned: in this case, the is improved by the injection of materials which will change the initial structure of the soil.

Finally, ways to mitigate the susceptibility to liquefaction by preventing the pore pressure build up are treated.

These last methods consist in lowering the degree of saturation of the soil.

2.6.2 Counter measures for foundations and superstructures

In this subchapter, measures to reduce liquefaction consequences under the structural point of view are analysed; it will be possible to observe that the main target consists in avoiding the rise of differential settlement in the soil underlaying the structure.

The first available effective measure to undertake against liquefaction is given by the realization of a pile foundation: tip-bearing piles are the best solution, since their the entire bearing capacity is given by tip. These piles must pass through the liquefied zone. reaching a soil layer with a high bearing capacity. In fact, if liquefaction occurs in a shallow soil layer, this layer must be able to bear the entire load. Thus, the pile foundation must be designed considering only the tip resistance and the shaft resistance of the pile portion embedded in the non-liquefiable layer. Moreover, if a soil is subjected to liquefaction, the sandy layer gets thinner and thus a negative friction will be generated; this additional load must be considered in the design of the pile foundation. The underestimation of this phenomenon could be crucial: it will result in a superficial settlement which is detrimental for the stability of the superstructure. Finally, even if the application of pile foundation can be considered an effective

measure to protect against the ultimate limit state caused by liquefaction, an eventual liquefaction-induced settlement could cause serviceability problems on the structure.

The opposite solution, in terms of stiffness, is given by building the superstructures as stiff as possible to absorb the differential settlement suffered by the underlaying soil. In this case, the structure is affected by high internal forces, mainly acting on its lower part. Thus, very stiff structural elements are needed in the foundation and in the superstructure. These measures are represented by the addition of braces on the lower floors and the stiffening of the shallow foundation.

Another possible choice is represented by a raft-foundation with friction piles stopping in the middle of liquefiable deposit. This measure can be considered as a middle way compared to the previous two. In fact, the structure is partially supposed to settle together with the surrounding soil; the remaining part of the settlement will not occur, since it is transferred as constraint action through the foundation (Kokusho, 2017).

2.6.3 Reinforcement interventions by mixing with chemical substances

The soil improvements by solidification of injected substances (such as cement mortars or colloidal resins) is an effective measure against the soil liquefaction. It produces a reduction of the interstitial voids due to the action of chemical mixtures. The direct consequence of the soil void reduction is the decreasing of the tendency to densify and the increase of the soil cohesion. Although the densification is an optimal measure concerning the clean sands, its effectiveness is reduced in fine grained cohesionless soils. Thus, in case of silty soils, the technique described in the following must be adopted. It is essential to recommend that, because chemical agents are added to the soil in these methods, the side-effect is linked with the contamination of the natural environment. Particularly, the contamination of the ground water is caused; so, these techniques should be very carefully employed nearby urban urbanized areas.

Having said that, the three main reinforcement interventions by mixing with substances described in this section are: permeation grouting, jet grouting and deep soil mixing.

The permeation grouting injects grout fluid of lower viscosity into the interstitial voids of coarse-grained soils. This method improves the soil in two ways: primary, a bond between the soil particles is set, thus, an initial cohesion is given to the soil; moreover, the higher is the

interstitial voids reduction, the lower will be the permeability of the treated soil. Columns and diaphragms of grouted soil can be designed to confine and/or reinforce portions of soil.

The jet grouting uses high-pressure fluid jetting from nozzles of rotating drilling rod moving vertically to cut in situ soils and form cement-mixing soil columns; these columns will replace liquefiable soil portions. The arrangement of the cement columns in the soil can be regular or irregular; with an irregular arrangement portions of liquefiable soil are confined. The jet grouting can be used in every soil type, regardless of the grain size distribution.

The deep soil mixing consists in solidifying liquefiable soils by mixing cement in slurry or dry powder by rotating a large auger; thus, large diameter soil-cement diaphragms are formed in deeper grounds. In this way, the shear stresses by the earthquake are in part transferred to the grouted columns. Consequently, the shear strains are reduced, so the soil densification is inhibited. As well as the jet grouting, this technique can be used in every kind of soil (Foti et al., 2009).

2.6.4 Densification processes

The densification of coarse-grained soils is a very effective measure to improve the resistance against liquefaction. In fact, during the process, the interstitial voids are decreased and, thus, the tendency of the soil to liquefy will be reduced. Since the higher is the void ratio the more effective is the densification, the effectiveness of these methods is fully obtained only if applied in clean coarse-grained soils (Kokusho, 2017).

The most common densification techniques are treated in the following, particularly: deep dynamic compaction, vibro-compaction, vibro-replacement, compaction grouting.

In the deep dynamic compaction, the potential energy of a heavy hammer falling from several meters is employed to produce the compaction of the underlying soil. The improved soil layer is usually 12 meters-deep; anyway, this depth depends on many factors, such as the grain size distribution, the degree of saturation, the permeability, the relative density as well as the height of fall and the weight of the hammer. The vibrations and the shocks produced by the hammer make this method impracticable in sites near existing buildings (Martin, 2003).

The vibro-compaction provides that the soil is densified by means of a steel tubular casing. The casing is lowered down into the soil by vibrations; then, as soon as it is raised up, filling

material is added to the densified soil. In order to reach a high level of compaction, this method must be employed in soil with a value of clay content lower than 2%.

The vibro-replacement is a measure similar to the vibro-compaction; in fact, the same procedure is followed, and the same tools are employed. During the vibro-replacement, unlike the previous method, 1 m-diameter gravel columns are created while the casing is raised up. The benefit of the columns concerns not only in the increasing of the density but also in the improvement of the drainage conditions and the shear resistance of the treated soil. The effectiveness of the method is lost in case of fine content percentages higher than 20%.

The compaction grouting of the soil consists in injecting a mixture of sand, cement and water into the liquefiable soil layer. This way, the soil confinement is achieved thanks to the soil mass moved by the applied pressure. Furthermore, the mixture replaces the empty portions of soil generated by the densification. This method is particularly useful in case of inaccessible areas, i.e. where the use of the previously described instrumentations is inconvenient (Foti et al., 2009).

2.6.5 Pore-pressure dissipation

In this method, named “Gravel drains”, an arrangement of gravel columns is created into the susceptible soil. By means of these columns, during the seismic event, the pore-pressure excess is drained before the effective stress achieve a null value. The spacing of the grids is designed basing on the soil permeability (Kokusho, 2017).

A gravel drain is put in place by means of an external casing, driven into the soil and filled by gravel; the casing is subsequently pulled up during the column composition.

Concerning the drainage measures it must be pointed out that only permanent measures of water table lowering can be considered as fully effective against the occurring of liquefaction. In fact, the use of drainage measures does not imply neither the inhibition of the pore pressure increasing nor the occurring of settlement.

2.6.6 Dewatering and desaturation

The last-mentioned measures for liquefaction mitigation are dewatering and desaturation.

Dewatering is an effective technique, which consists in inhibiting the liquefaction hazard on the shallow soil layers by lowering the water table level. As it is known, the occurring of liquefaction into a deep soil layer has no effect on the overlaying facilities. Thus, the water table lowering is carried out up to a level where the occurring of liquefaction has no relevant effects. However, attention must be paid dealing with highly compressible soils (Kokusho, 2017). In fact, in these situations, the ground settlement induced by the dewatering could itself cause damages on the human facilities.

Desaturation is a widespread measure thanks to its effectiveness and inexpensiveness. It is known that the liquefaction resistance tends to rise considerably by lightly lowering the saturation degree from 100% to 90%. An effective way to desaturate the soil is given by the "*Induced Partial Saturation*". This technique consists in injecting air bubbles into liquefiable soil layers; in this way, the degree of saturation is reduced and the liquefaction resistance CRR is increased. (Kokusho, 2017)

3. EVALUATION METHODS TO LIQUEFACTION TRIGGERING ASSESSMENT

3.1 Description of the available methods

The evaluation methods to liquefaction triggering assessment aim to determine the behaviour of a soil during the shearing induced by the ground motion. In broad terms the liquefaction assessment methods can be distinguished between: simplified methods, methods based on laboratory testing, computational mechanics approaches and reduced scaled models.

The studies, carried out in laboratory, have shown that the occurring of liquefaction is mainly related to the soil conditions and the load conditions. As it will be subsequently explained, the dynamic analyses represent the most complete and reliable evaluation method. Nevertheless, if the possibility to carry out dynamic analyses is neglected, the use of simplified method is suggested by the Eurocode 8 (EN 1998-5).

The simplified methods can be divided into 3 main categories: stress-based, strain-based, energy-based.

The most used stress-based method was idealized by Seed and Idriss (1971) and further developed over time (Boulanger and Idriss, 2015). This method transforms the irregular time history of a seismic event to an equivalent regular one; then, the resulting regular cyclic load must be compared with a cyclic resistance index, obtained by the observation of the liquefaction phenomena occurred in the past. In this way, a global safety factor (*FS*) against liquefaction triggering is defined and a deterministic assessment of the liquefaction hazard can be performed.

Liquefaction triggering approaches that employ ground motion intensity measures other than the peak ground acceleration (PGA) commonly have been classified as “energy-based approaches”, regardless of whether the intensity measure is truly a measure of energy. Many of the proposed procedures were developed using an approach like the one used for the simplified stress-based method; i.e., correlations relating in situ test measurements of liquefaction resistance derived from case histories (*NASEM*, 2016).

The cyclic strain approach assess liquefaction triggering trough the prediction of pore pressure generation as function of the earthquake-induced shear strain. The approach takes

advantage of the fact that cyclic compression (for drained conditions) and pore pressure generation (for undrained conditions) are related more closely to shear strain than shear stresses. As shown in the figure 3.1, the relationship between excess pore pressure ratio (r_u) and cyclic strain (γ_{cyc}) for a given number of constant amplitude strain cycles in strain-controlled tests falls in a relatively narrow band. The volumetric threshold shear strain, defined as the shear strain below which no pore pressure develops, is consistently about 0.01% for normally consolidated sands (NASEM, 2016).

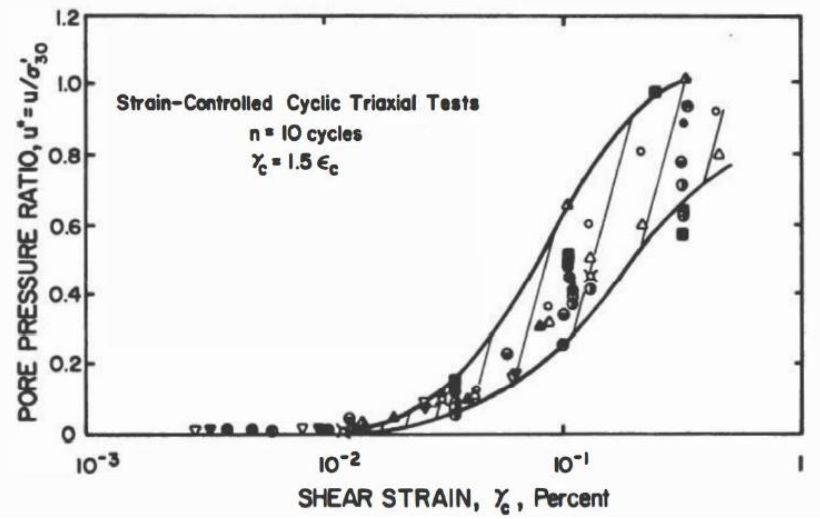

Figure 3.1- Relationship between pore pressure ratio and cyclic strain for 10 cycles of loading in strain-controlled testing (NASEM, 2016).

As mentioned above, an alternative way of liquefaction triggering assessment is based on laboratory testing. This approach consists in sampling a soil portion and submit it to a cyclic triaxial (CTX) test or a direct simple shear (CDSS) test; these tests are carried out under undrained conditions and their duration depends on the needed time to reach the liquefaction state. It could be possible to subject a sample to the characteristic load history of the sampling site and evaluate the pore pressure evaluation. However, this approach only allows to assess the liquefaction occurring for a particular situation and therefore it is inappropriate to get an overview of the site behaviour under any unknown cyclic load history; in fact, evaluating the pore pressure development for a particular load configuration, the safety factor (FS) is not obtained and, accordingly, a safety margin is not established. Therefore, it is usual to submit the sample to several stress values exploring the soil behaviour under a certain range of admissible amplitude values. In each test, a cyclic load history with a particular amplitude is imposed to the sample and the pore pressure excess is evaluated. This procedure is repeated for

a significant number of amplitude values and then these values are represented in a graph in function of the number of cycles at which liquefaction take place (Figure 3.2). Trough the interpolation of the obtained results the τ_{cyc}-N plane is divided into two regions: the part above the curve contains the pairs of values τ_{cyc}-N that produce liquefaction, the lower half plane contains values representing safe conditions against liquefaction.

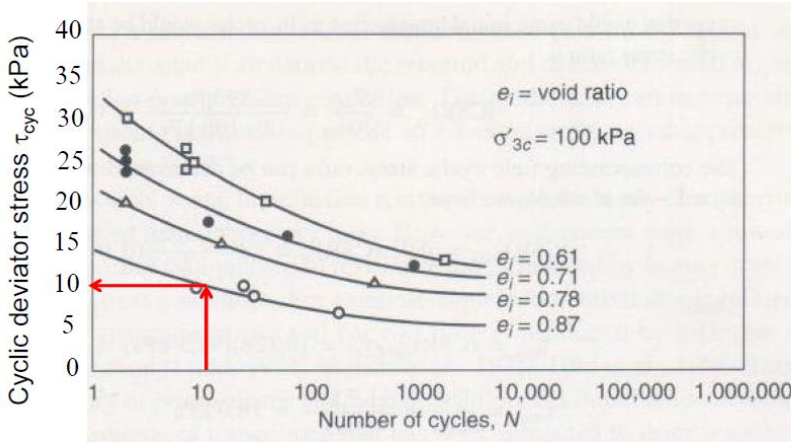

Figure 3.2- Results of direct shear tests on frozen samples (Seed and Lee, 1965)

The drawbacks of laboratory tests are:

- difficulties to preserve the soil structure in sampling of coarse-grained soils;
- the sample reconsolidation in the triaxial load cell alters the sample response;
- difficulties to build homogeneous samples;
- difficulties to guarantee the full saturation, since the soil response changes significantly with a saturation degree S_r slightly less than 100%.

A more precise evaluation of the soil behaviour in shearing is obtained with a dynamic 1-D or 2-D Finite-Element-Method analysis based on the local seismic response of the site. In this way, the trend of shear stress and shear strain during the ground motion is evaluated and an accurate estimation of the pore pressure excess is obtained. In order to get such a detailed estimation of the soil behaviour, equally detailed input data are needed to define the geotechnical model; for this reason, several in situ tests and laboratory tests must precede the construction of the FEM model.

The last-mentioned approach is the use of reduced scale models. This approach is based on the principle that, if a model whose linear dimension is reduced by a factor N, is subjected to a

centrifuge acceleration of $a = Ng$ (where g is the gravity field), the self-weight of any material used for the model is N times larger than in a 1g gravity field. Therefore, a 1/N model at a centrifuge acceleration of $a = Ng$ achieves the equivalent vertical stress of the full-scale prototype, assuming that a material with the same mass density is used in the model. If the stress-stain characteristic of the model material is the same as in the prototype, for example if the same soil is used in the model, similarity of strains is also achieved. Having said that, if a load history is applied to the soil model through a 1g shaking-table, the increasing of the pore pressure can be simulated and the occurring of liquefaction can be assessed (*NASEM*, 2016).

3.2 Description of two simplified methods

In this section, the stress-based method of Seed and Idriss (1971) and the energy-based method proposed by Millen et al. (2019) are be described in detail, since they will be later compared on chapter 6.

3.2.1 Stress-based method

The proposed approach concerning the stress-based method is the one proposed by Seed and Idriss [1971]. As previously mentioned, the design acceleration history of a site is turned into an equivalent one characterized by constant amplitude cycles; then, this measure of the demand is compared with a measure of the soil cyclic resistance, which is obtained from in situ tests. The deterministic procedure is based on the calculation, at different depths of a site, of two main variables:

- the seismic demand represented by the *Cyclic Stress Ratio* (“CSR”);
- the resistance capacity against liquefaction, given by the Cyclic Resistance Ratio; this value can be also seen as the maximum CSR which a site can suffer.

If the seismic demand (CSR) exceeds the cyclic resistance it can be assumed, in a deterministic way, that liquefaction occurs in the site. The ratio between CSR and CRR provides the safety margin against liquefaction (Eq. 6):

$$FSL = \frac{CRR}{CSR} \tag{6}$$

The EC8 [EN1998-5, 2005] imposes a minimum value of the safety factor of 1.25 (Foti et al., 2009).

3.2.1.1 Evaluation of the Cyclic Stress Ratio

The earthquake-induced solicitation CSR is empirically obtained by the experience on the field, based on test carried out on several samples.

A soil element with a depth equal to *z* from the ground surface is considered (Figure 3.3):

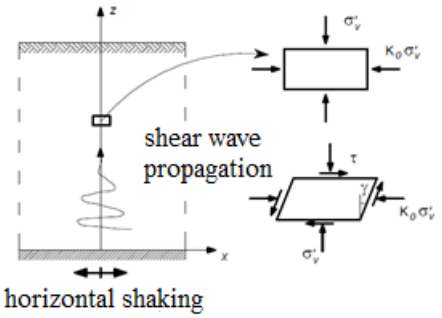

Figure 3.3- Stresses acting on a soil element at a depth z (adapted from Foti, 2009)

The earthquake causes an increase in the sample stress, which can no longer be considered in geostatic conditions. In order to obtain the induced stresses in the soil element, i.e. at a depth *z*, a seismic local response of the entire analysed soil column should be carried out. Unfortunately, local site response analyses are too expensive and thus, not widespread in the common design. If these analyses are not available, the considered acceleration on the soil element is the characteristic one for the analysed site. Then, the stress on the mentioned soil portion is obtained by means of an equation of dynamic equilibrium of the entire soil column overlying the element. Handling the equation, the maximum shear stress τ_{max} at a depth *z* is obtained in function of the maximum acceleration on the ground surface, which is often the only available data:

$$\tau_{max} = \sigma_{vo} \cdot \frac{a_{max}}{g} \cdot r_d \tag{7}$$

where:

a_{max} is the peak ground acceleration (*PGA*) induced by the earthquake;

g is the gravity field;

σ_{vo} is the initial vertical stress at a depth *z*;

r_d is a reduction coefficient, which decreases the *PGA* in order to evaluate the maximum acceleration at a depth *z*; this reduction is due to the amplification phenomena produced by the total reflection of the seismic waves on the ground surface. In the daily design r_d can be evaluated as (Idriss,1999):

$$r_d = \exp[\,\alpha(z) + \beta(z) \cdot M] \tag{9}$$

$$\alpha(z) = -1.012 - 0.126 \sin\,(z/11.73 + 5.133) \tag{10}$$

$$\beta(z) = +0.106 + 0.118 \sin\,(z/11.28 + 5.142) \tag{11}$$

where M is the magnitude.

Since the maximum stress through the time belongs to an irregular time series, it must be reduced, in order to turn the load history into a regular one. This process is due to the fact that a regular cyclic time history is easier to reproduce in laboratory and, in addition, results from different earthquakes can be compared. Conventionally, the amplitude of the applied regular cycles is considered as the 65% of the peak amplitude, i.e.:

$$\tau_{cyc} = 0.65\tau_{max} \tag{12}$$

$$\tau_{cyc} = 0.65 \cdot \sigma_{vo} \cdot \frac{a_{max}}{g} \cdot r_d \tag{13}$$

Finally, the cyclic stress ratio is defined as the obtained τ_{cyc} normalized to the reference geostatic effective stress:

$$\tau_{cyc} = 0.65 \cdot \frac{\sigma_{vo}}{\sigma'_{vo}} \cdot \frac{PGA}{g} \cdot r_d \tag{14}$$

On the other hand, the number of reduced-amplitude regular cycles which make the solicitation equal to the irregular one must be defined. Assuming that the magnitude of the cycles is related to the earthquake duration, Seed et al. (1975) have built a relationship between the equivalent number of cycles which produce a pore pressure increase equal to the irregular time series, and the magnitude associate to this time series (Figure 3.4).

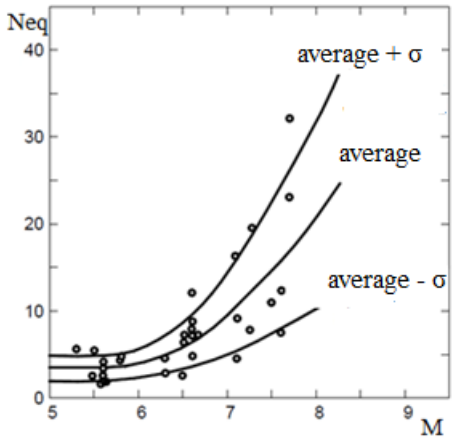

Figure 3.4- Relationship between equivalent number of cycles to 0.65 τ_{max} and Magnitude (adapted from Seed et al., 1975)

The curve is calibrated in order to make the 7.5 magnitude corresponding to 15 cycles. In this way, the stress history is fully defined, i.e. amplitude and duration are settled (Foti et al., 2009).

3.2.1.2 Evaluation of the cyclic resistance ratio

The following step concerning the liquefaction triggering assessment is represented by the evaluation of the soil resistance. It is common practise to rely on empirical correlation, based on in situ tests carried out in the past. The more widespread tests in this compound are (Foti et al., 2009):

- standard Penetration Test (SPT);
- cone Penetration Test (CPT);
- in situ test available for the shear wave velocity estimation (V_S);
- Becker Penetration Test (BPT).

Only the correlation concerning the CPT will be analysed in this paper, as considered the most reliable. Although the SPT has been used for 75 years, CPT results are preferred to SPT; this is mainly due to the lack of repeatability of the SPT, raising because of two factors: the variability in the input energy and the dynamic nature of the test. On the other hand, thanks to the explosion of knowledge and technology associated with the CPT, a continuous data record and accuracy is nowadays offered by the results obtained from the Cone Penetration Test (Jefferies, 2016).

All the previously mentioned available procedures for the CRR evaluation are referred to an earthquake with a magnitude of 7.5, equivalent to 15 load cycles. Therefore, every estimation must be carried out considering the expected magnitude of the site.

Such correlation is introduced by means of the *Magnitude Scale Factor* (MSF). Among the several correlation present in literature, the one from Boulanger and Idriss (2015) is proposed in equations 15 and 16:

$$MSF = 1 + (MSF_{max} - 1) \cdot \left[8.64\ exp\left(\frac{-M}{4}\right) - 1.325\right] \tag{15}$$

$$MSF_{max} = 1.09 + \left(\frac{q_{c1Ncs}}{180}\right)^3 \leq 2.2 \tag{16}$$

where

q_{c1Ncs} is the penetration resistance of a soil corrected by some factors described in the following.

Another correction to make on the available database concerns the depth from the ground surface of the analysed soil portion. Laboratory test have shown that, the higher is the depth and the higher is the liquefaction resistance; for this reason, a reductive factor is applied in the to the soil portion with a high confining pressure (Youd et al., 2001):

$$\begin{cases} k_\sigma = \left(\frac{\sigma'_{vo}}{p_a}\right)^{(f-1)} & if\ \sigma'_{vo} > p_a \\ k_\sigma = 1 & if\ \sigma'_{vo} \leq p_a \end{cases} \tag{17}$$

Where σ'_{vo} is the vertical effective stress, p_a is the atmospheric pressure, *f* is a parameter depending on the site condition (Table 3.1), the relative density and the age of the deposit.

f	**D_R [%]**
0.8	≤40%
0.5-0.005·(D_R-40)	40<D_R<80
0.6	D_R>80%

Table 3.1- Values of f depending on the relative density (Youd ed al., 2001)

With the correction of the two previous corrective factor the new formula for the safety factor of a soil portion against liquefaction is:

$$FSL = \frac{CRR}{CSR} = \frac{CRR_{7.5}}{CSR} \cdot MSF \cdot k_\sigma \tag{18}$$

3.2.1.3 CRR evaluation with Cone Penetration test results

The correlations between CPT test results and CRR are based on normalized values of the cone resistance, referring to the depth at which the test is carried out. The normalized value is produced by the following expression [Robertson and Wride, 1998]

$$q_{c1N} = C_Q \left(\frac{q_c}{p_a}\right) \tag{19}$$

Where q_c is the static end resistance, p_a is the atmospheric pressure and C_Q is the normalization factor for the cone resistance, expressed as:

$$C_Q = \left(\frac{p_a}{\sigma_{vo}}\right)^n \leq 1.7 \tag{20}$$

Where *n* depends on the soil type [Olsen, 1997] and it can be expressed as:

$$\begin{cases} n = 0.5 \; for \; clean \; sands \\ n = 1.0 \; for \; clayey \; soils \\ 0.5 \leq n \leq 1.0 \; for \; silt \; and \; silty \; sand \end{cases} \tag{21}$$

In the case of silty sand, a correction coefficient must be introduced on the calculation of q_{1cN}, obtaining:

$$(q_{c1N})_{CS} = k_c \cdot q_{c1N} \tag{22}$$

where k_c is defined in below [Robertson and Wride, 1998]

$$\begin{cases} k_c = 1.0 & for\ I_C \leq 1.64 \\ k_c = -0.403I_c^4 - 5.581I_c^4 - 21.630I_c^4 + 33.750I_C - 17.88 & for\ I_C \geq 1.64 \end{cases} \tag{23}$$

where I_C is an index of the soil behaviour (further information about this index can be found ISSGSC, 2009).

Several values of q_{1cN} coming from sites affected by seismic events have been collected and related to the magnitude M=7.5; these values are represented in a graph in function of the corresponding CSR and a curve is traced (Figure 3.5). The mentioned curve divides the plane into two parts: in the upper zone all the points related to sites where liquefaction occurred during the seismic event are contained; on the other hand, below the curve, points with a certain safety margin against liquefaction are represented. In this way, the CSR of the points represented along the curve can be also seen as the CRR of the site, since it is the limit CSR value that the site can sustain. The separation line can be also analytically expressed as:

$$\begin{cases} CRR_{7.5} = 0.83 \cdot \left[\frac{q_{c1N}}{1000}\right] + 0.05 & if\ q_{c1N} < 50 \\ CRR_{7.5} = 93 \cdot \left[\frac{q_{c1N}}{1000}\right]^3 + 0.08 & if\ 50 < q_{c1N} < 160 \end{cases} \tag{24}$$

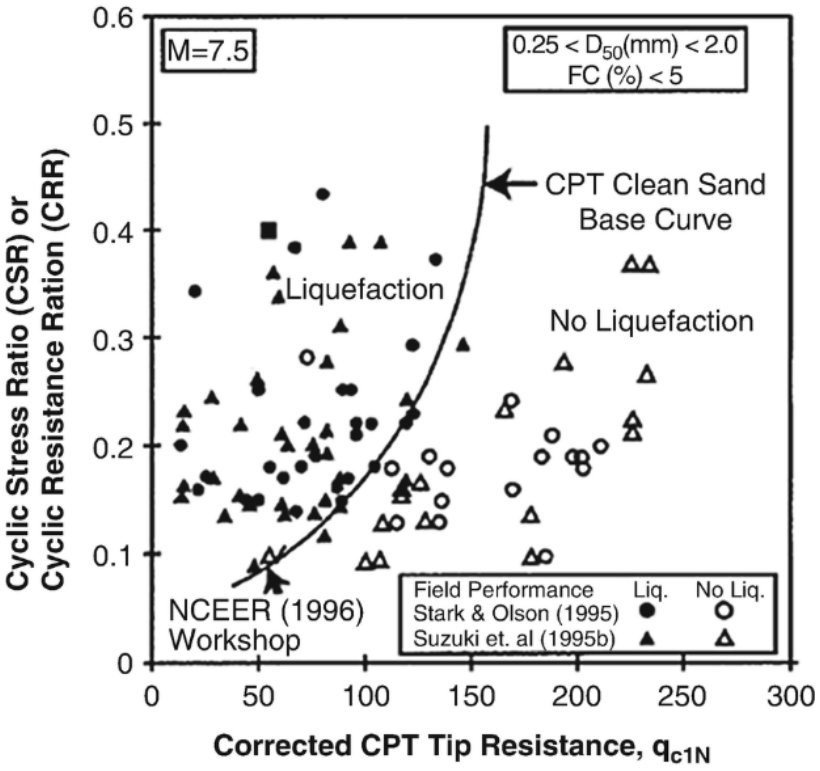

Figure 3.5- Relationship between CRR and CPT results (Youd et al., 2001)

Once the solicitation and the resistance are defined, a punctual deterministic analysis of liquefaction triggering assessment can be carried out evaluating the FSL in function of the depth.

3.2.1.4 Evaluation of the pore pressure excess

Until now, a deterministic evaluation of the liquefaction triggering has been carried out considering the PGA (on the CSR evaluation) and the cone resistance (on the CRR evaluation) as central parameters. However, as it has been previously described, the central value concerning the liquefaction triggering is the pore pressure. In fact, the measure of the *u* value increase is the more physically consistent way to deal with the phenomenon. Thus, a qualitative description regarding the pore pressure evaluation of the point contained in Figure 3.5 can be provided. The graph contains values scaled on magnitude 7.5, i.e. an equivalent number of cycles to apply in laboratory of 15. Hence, if we represent the pore pressure evolution of these points, the following behaviour will be obtained: all the points contained on the upper part of the graph (values circled in green on Figure 3.6a) will reach a unitary value earlier than 15

cycles, while the other points (values circled in green on Figure 3.6a) will resist for a number of cycles bigger than 15. The concept is graphically showed Figure 3.6.

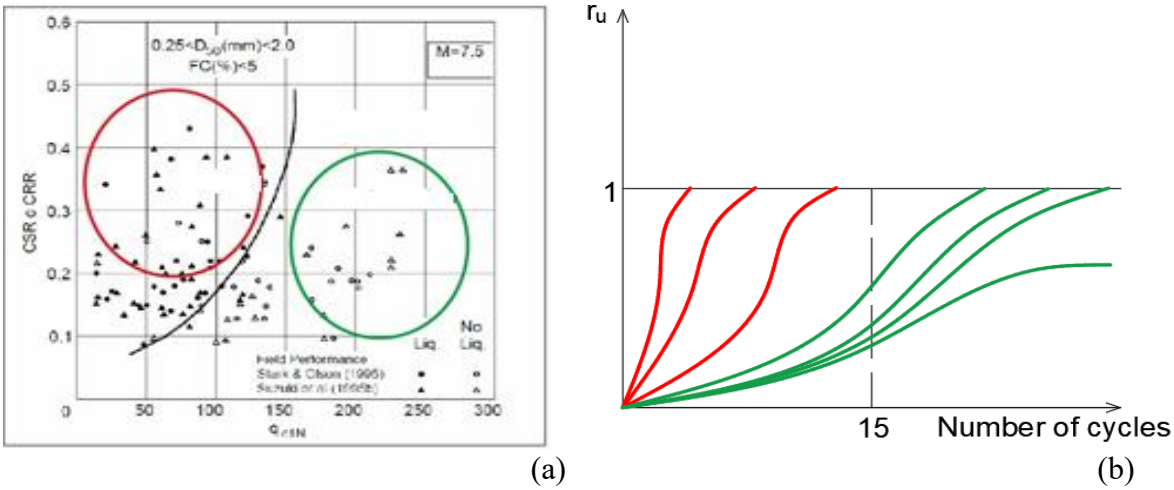

Figure 3.6- (a) Relationship between CRR and CPT results (Youd et al., 2001). (b) Idealized pore pressure trend of the point on Figure (a)

An analytical representation of the pore pressure increasing model on Figure 3.6b was idealized by Seed at al. (1975, Eq. 25) and later simplified by Booker et al. (1976, Eq. 26) with equations:

$$r_u = \frac{1}{2} + \frac{1}{\pi}\, arc\sin\left[2\left(\frac{N}{N_L}\right)^{\frac{1}{\beta}} - 1\right] \tag{25}$$

$$r_u = \frac{2}{\pi}\, arc\sin\left[\left(\frac{N}{N_L}\right)^{\frac{1}{2\beta}}\right] \tag{26}$$

Where:

r_u is the pore pressure ratio

N is the equivalent number of uniform cycles

N_L is the number of cycles required to cause liquefaction

β is an empirical parameter

N_L and β, can be determined by cyclic triaxial tests. For a given soil, N_L increases as relative density increases and decreases as the magnitude of loading increases, with the magnitude of

loading expressed in terms of Cyclic stress ratio (CSR). The use of N_L has its drawbacks as it can only be applied to liquefiable soils (Polito et al., 2008). However, "non-liquefiable" soils, such as dense sands and soils with plastic fines, can still undergo significant pore pressure increases and deformations as a result of cyclic softening (Boulanger and Idriss, 2006). Booker et al. (1976) proposed a value of 0.7 for β, while Polito et al. (2008) proposed the following empirical equation:

$$\beta = c_1 FC + c_2 D_r + c_3 CSR + c_4 \tag{27}$$

where F_C is the fines content, D_r is the soil relative density, and c_1, c_2, c_3 and c_4 are regression constants which vary with the fines content. For FC<35%: c_1=0.01166; c_2=0.007397; c_3=0.01034; and c_4=0.5058; and for FC≥35%: c_1=0.002149; c_2=−0.0009398; c_3=1.667; and c_4=0.4285.

The number of uniform cycles (N) equivalent to an irregular earthquake ground motion can be obtained by the weighting scheme proposed by Seed et al. (1975) which was later used by Idriss (1999), Liu et al. (2001), Boulanger and Idriss. (2006), Kishida et al. (2014). The Seed stress-based model considers a power relationship between the cyclic stress ratio and the number of cycles (Eq. 28):

$$CSR = a \cdot N^{-b} \tag{28}$$

where a and b are fitting parameters.

Therefore, for two individual stress cycles with CSR_A and CSR_B, the relative number of cycles to cause failure at these two stress ratios is easily obtained (equation 29). Assuming a reference value of uniform cycles for the magnitude of 7.5 ($N_{M=7.5}$), the obtained ratios of CSR correspond to the definition of a magnitude scaling factor (MSF) used in the Seed simplified procedure to calculate the seismic demand of liquefaction potential with equation 30. The MSF can also be calculated using equation 31 from Boulanger and Idriss (2015). There have been several proposals for the b parameter such as b =0.34 for sands D

$$\frac{N_A}{N_B} = \left(\frac{CSR_B}{CSR_A}\right)^{\frac{1}{b}} \quad MSF = \frac{CSR_M}{CSR_{M=7.5}} = \left(\frac{N_{M=7.5}}{N_M}\right)^b \tag{29}$$

$$CSR_{M=7.5} = 0.65 \cdot \frac{\sigma_{vo}}{\sigma'_{vo}} \cdot \frac{PGA}{MSF} \cdot r_d \quad (30)$$

$$MSF = 1 + (MSF_{max} - 1) \cdot \left[8.64\ exp\left(\frac{-M}{4}\right) - 1.325\right] \quad (31)$$

$$MSF_{max} = 1.09 + \left(\frac{q_{c1Ncs}}{180}\right)^3 \leq 2.2 \quad (32)$$

where

PGA is the peak ground acceleration in g

r_d is parameter related with the depth

$\frac{\sigma_{vo}}{\sigma'_{vo}}$ is the overburden stress ratio

(Airoldi et al,2018).

3.2.1.5 Liquefaction Potential Index (LPI)

It is important to observe that the calculation of FSL provides a punctual evaluation of the liquefaction hazard. However, a punctual analysis of the phenomenon could lead to evaluation errors. In fact, the liquefaction of a thin soil layer does not affect the stability of the overlaying facilities.

The actual consequences of the liquefaction triggering depend on the extension of the affected soil and the depth at which liquefaction occurs. Therefore, the punctual analysis is carried out on several depths and, then, the results are handled in order to obtain a global estimation.

A significant evaluation of the global effect of liquefaction is provided by the *Liquefaction Potential Index* (*LPI*) (Iwasaki et al.,1978). The main parameters affecting this index are: the thickness of the liquefiable layer, its proximity to the ground surface and the FSL values along the affected thickness. The LPI is defined by the equation 33 (Iwasaki et al., 1978):

$$LPI = \int_0^{20} F(z) \cdot\ w(z)\ dz \quad (33)$$

Where z is the distance from the ground surface expressed in meters, $F(z)$ is calculated as:

$$F(z) = \begin{cases} 1 - FSL(z) & if\ F(z) \leq 1 \\ 0 & if\ F(z) < 1 \end{cases} \quad (34)$$

And $w(z)$ is a function of the depth of the analysed soil element, calculated as:

$$w(z) = 10 - 0.5 \cdot z \quad (35)$$

As it is possible to note in equation 35, the global factor is only calculated on 20 m from the ground surface, since the liquefaction of a soil portion deeper than 20m does not cause consequences on the superficial facilities.

The index can be associated to the damage on the surface by means of the correlation provided by Iwasaki et al. [1982] which are showed in the table below.

Finally, a value of $LPI \geq 5$ indicate the need of mitigation measures (Table 3.2).

LPI	Damage potential
≤5	low
5-15	high
≥15	very high

Table 3.2- Correlation of LPI with damage potential (adapted from Foti et al.,2019)

3.2.2 Energy-based methods

Energy based methods are formulated on different set of assumptions to stress based methods and therefore have some unique advantages (Millen et al, 2019):

- while stress based methods typically rely on instantaneous quantities such as peak ground acceleration (PGA), energy-based methods use cumulative intensity measures, which typically have lower dispersion.
- energy based methods are typically load amplitude independent, and therefore can quantify liquefaction resistance as a single value, compared to stress-based methods which use a relationship between amplitude and number of constant stress cycles.
- for constant amplitude input motion, stresses decrease as pore pressure increases, whereas energy is conserved.

The development of an strain energy-based liquefaction triggering method was first proposed by Davis et Berril (1985) following the assumption made by Nemat-Nasser et al. (1979) that the pore pressure build-up is linearly correlated to the amount of dissipated seismic energy per unit volume of soil, which is a function of the standard penetration value, the initial effective overburden stress and the energy arriving at a site. The full expression for the pore pressure increase is shown in equation 36:

$$\Delta u = \frac{C(N_1)}{r^2\sqrt{\sigma_0'}} 10^{1.5M} \tag{36}$$

where,

M is the earthquake magnitude

r is the distance of a site from the centre of energy release

σ_0' is the initial effective overburden stress

$C(N_1) = c_1 \cdot c_2 \cdot \lambda(N_1) \cdot 10^{1.8}$ determined empirically from a study of liquefaction case histories being N_1 the average corrected standard penetration value.

Later on, Berril et al. (1985) have proposed another relationship:

$$r_u = \beta \cdot W^{\zeta} \tag{37}$$

where W is the energy dissipated per unit volume of the soil normalized by the initial effective confining pressure, defined as follows:

$$W = \frac{1}{\sigma_0'} \int_0^t \tau \, d\gamma \tag{38}$$

being τ the shear stress and γ the shear strain. For undrained cyclic triaxial test loadings W is the cumulative enclosed area of the shear stress–strain loops, which can be computed by equation 39:

$$W = \frac{1}{2\sigma_0'} \sum_{i=1}^{n-1} (\sigma_{d,i+1} + \sigma_{d,i})(\varepsilon_{a,i+1} - \varepsilon_{a,i}) \tag{39}$$

where σ_d is the applied deviator stress at a load increment and ε_a is the axial strain at a load increment.

Green et al. (2000) proposed a simplified relationship to estimate pore pressure based on the dissipated energy and PEC the "pseudo-energy capacity":

$$r_u = \sqrt{\frac{W}{PEC}} \leq 1 \tag{40}$$

where, PEC is basically the dissipated energy at liquefaction and it can be determined from cyclic test data by simply dividing the value of W at r_u=0.65 by 0.4225. In 2008, Polito et al. (2008) proposed a new equation to calculate PEC.

More recently, Kokusho (2013) proposed a simplified liquefaction triggering procedure. For the estimation of the soil capacity, CSR_{20} is evaluated with correlations with SPT blow counts and then normalised dissipated energy is estimated as indicated by Figure 3.7 for two different liquefaction criteria defined by double amplitude axial strains of 2% and 5%.

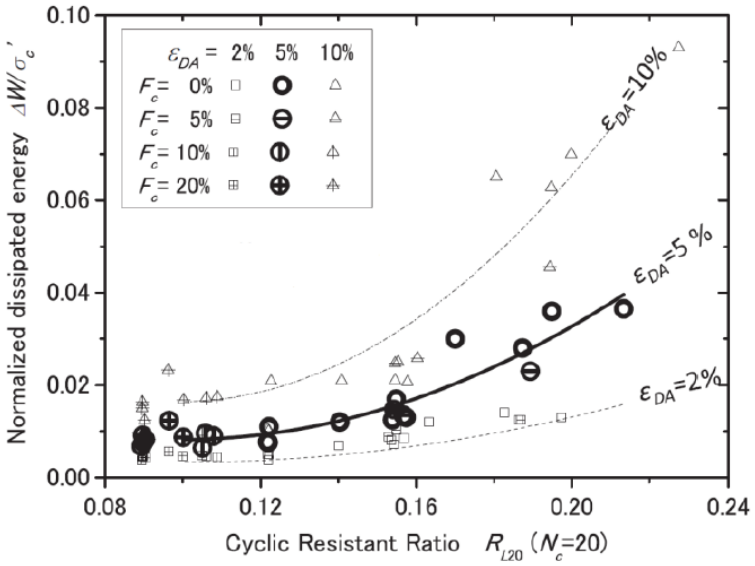

Figure 3.7- Relationship between normalized dissipated energy and CSR_{20} (Kokusho, 2013)

The dissipated energy (ΔW) is then converted to the strain energy (W) by equation 41:

$$\frac{W}{\sigma_c'} = 5.4 \cdot 10^{1.25 \cdot \log(\Delta W/\sigma_c')} \tag{41}$$

From the strain energy, the strain capacity of the soil is computed by multiplying the strain energy by the thickness of the layer, which is compared to the upward energy.

In fact, in this method the demand is estimated by the upward energy density calculated by equation 42:

$$E_u = \rho V_S \int (\ddot{u})^2 \, dt \tag{42}$$

where,

ü is the particle velocity of seismic waves propagating in the upward direction, obtained by integration of base acceleration;

ρ is the soil density;

Vs is the S-wave velocity.

To identify liquefaction triggering the energy ratios of individual layers are numbered sequentially starting from the lowest ratio and summed up. According to Kokusho (2013) liquefaction occurs in that sequence and in those layers for which the sum is lower than 1, because the upward energy can liquefy individual sand layers in the mentioned sequence until it is totally used by the energy capacities.

Methods that adopt dissipated energy have two major drawbacks, one is that the estimation of the dissipated energy within a soil profile from a seismic shear wave is far from trivial and very dependent on soil characteristics and changes as pore pressure increases. Secondly, the dissipated energy rapidly increases as the soil approaches liquefaction, and therefore a small change in the criteria for liquefaction triggering (e.g. change the limiting pore pressure ratio from 0.95 to 0.98), can have a large impact on the evaluated capacity.

In order to overcome this problem, Millen et al. (2019) proposed a new method to estimate pore pressure development based on the principles of conservation of energy. The liquefaction resistance is measured in terms of normalised cumulative absolute strain energy (NCASE), which is shown to be constant with loading amplitude, but sensitive to soil properties. NCASE was calculated as the cumulative change in absolute elastic strain energy divided by the vertical effective stress – equation 43. Graphically it can be obtained as the sum of the absolute change in elastic strain energy between two peaks in the response (Figure 3.8).

$$NCASE = \sum_{j=0}^{n_{peaks}} |\tau_{av,j}| \cdot |\gamma_{j+1} - \gamma_j| / \sigma'_{vo} \quad (43)$$

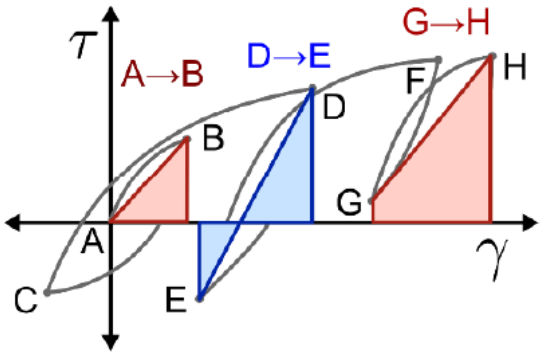

Figure 3.8- Calculation of NCASE graphically (Millen et al.,2019)

The pore pressure time series can be computed by the square root relationship presented in equation 44 where the NCASE at liquefaction ($NCASE_{liq}$) and the NCASE each cycle ($NCASE_i$) can be obtained by equations 45 *and* 46:

$$r_{u,i} = \sqrt{\frac{NCASE_i}{NCASE_{liq}}} \cdot r_{u,liq} \quad (44)$$

$$NCASE_{liq} = \frac{2 \cdot CSR^2 \cdot \sigma'_{vo} \cdot n_{liq}}{G_i \cdot \left(1 - \frac{CSR \cdot s_{r,ru=0}}{\tan(\varphi) \cdot (1 + s_{r,ru=0})}\right)} \kappa \quad (45)$$

$$NCASE_i = \frac{2 \cdot CSR^2 \cdot \sigma'_{vo}}{G_{s.ru=ru,i}} \quad (46)$$

Where $r_{u,liq}$ is the value of r_u reached during the test at which liquefaction is predicted, k is a calibrating parameter that can be taken equal to 1 (Kramer el al., 2016), S_r is a strain factor, λ is a reducing factor of the shear modulus, n_{liq} is the number of cycles required to liquefy for a given value of CSR, G_i is the maximum shear modulus (Millen et al, 2019).

3.3 Reduced scale models

As described earlier, reduced-scaled models can be used to simulate the increase of pore pressure in a soil deposit and, therefore, these models are also suitable to analyse the condition of liquefaction triggering. A shaking table can also be connected to the model in order to reproduce the real motion at the model scale.

A 1-g model relies on the gravity to apply body forces to the model: a 0.3 meters-tall model tested on a 1-g shaking table behaves exactly as a 3 meters-depth soil column subjected to the same ground motion. Having said that, centrifuge testing is usually conducted at a centrifugal acceleration of 20g or more. This procedure, called "Multi-g physical modelling", is based on a key principle: a model in which each linear dimension is reduced by a factor N, subjected to a centrifuge acceleration of $a = N \cdot g$, achieves the equivalent vertical stress of the full-scale prototype. The previous statement is valid only if a material with the same mass-density is used to build the model. Hence, a 0.3 meters-tall soil model, accelerated to 50g in a centrifuge, will be suitable to study the behaviour of a 15 meters-depth soil layer at a prototype scale. Moreover, if the stress-strain law of the tested soil model is the same as in the prototype, similarity in strain is achieved.

The theoretical reason behind the equivalence of the physical model and the equivalent prototype is in the fact that the soil behaviour is only dependent on the state parameters. Therefore, if nature (e.g. mineralogical composition), physical properties (diagenesis, cementation), effective stress state and stress history of the model are the same of the ones of the respective prototype, all the reduced-test results can be converted to the prototype scale.

Accordingly, to sum up: if the scaling factor for a generic quantity is defined as $x^* = \frac{x_{prot}}{x_{mod}}$ (where x_{prot}= the value of the quantity x at the prototype scale), in a soil prepared for the prototype material (i.e. identical material rheology in the model as in the prototype and density scaling factor $\rho^* = \frac{\rho_{prot}}{\rho_{mod}} = 1$), geometrically scaled down N times with respect to the prototype (geometrical scaling factor $g^* = \frac{g_{prot}}{g_{mod}} = \frac{1}{N}$), the centrifuge acceleration reproduce the same stress (Figure 3.9, Eq. 47) and strains as in the prototype so that the model exhibits identical mechanical behaviour as the prototype soil (Schofield, 1981).

$$(\sigma_v)_{prot} = \rho \cdot g \cdot z_p \approx \rho \cdot (N \cdot g) \cdot \left({}^{z_p}/_{N}\right) \approx \rho \cdot N_g \cdot z_m = (\sigma_v)_{mod} \qquad (47)$$

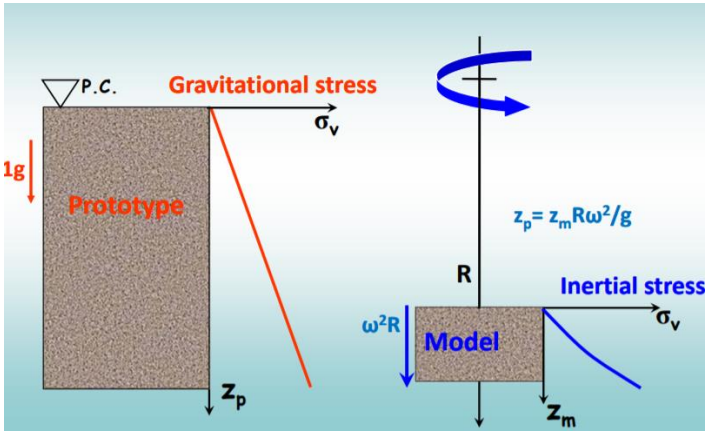

Figure 3.9- Trend of the stress through the depth in the model and prototype scale (Fioravante, 2012)

where:

N is the scale factor

z_p is the depth of the prototype scale

z_m is the depth at the model scale

The observations from the model can related to the prototype using the similarity relationship reported in the Table 4, which are valid within the continuum mechanics (Garnier et al. 2007).

	Variable	Scale factor $X^*=X_{prototype}/X_{model}$	Ng model
L	Length	L^*	N
ρ	Soil density	ρ^*	1
ε	Strain	ε^*	1
σ	Stresses (effective and total)	$\sigma^*=x^*\rho^*g^*$	1
G	Stiffness	$G^*=x^*\rho^*g^*/\varepsilon^*$	1
ρ_f	Fluid density	ρ^*	1
p	Fluid pressure	$p^*= x^*\rho^*g^*$	1
u	Soil displacement (continuum)	$u^*=x^*\varepsilon^*$	N
v	Velocity	$v^*=(x^*\varepsilon^*g^*)^{0.5}$	1
ü	Acceleration	g^*	N^{-1}
t	Time (diffusion phenomena)	$t^*=\mu^*L^{*2}/G^*$	N^2
t	Time (creep)	t^*	1
t	Time (dynamic)	$t^*=(x^*\varepsilon^*/g^*)^{0.5}$	N
μ	Dynamic viscosity of fluid	$\mu^*=\rho^*(g^*/x^*\varepsilon^*)^{0.5}$	N^{-1}
K_f	Compressibility modulus of soil	$K_f^*=x^*\rho^*g^*/\varepsilon^*$	1

Table 3.3- Principal scaling ratio for geotechnical centrifuge modelling (Airoldi et al.,2018)

Regarding the centrifuge modelling, the following key aspect should be always considered:

- since the centrifuge acceleration applied to the model is radius-dependent, the vertical stress distribution is parabolic, thus it diverges slightly from the linear distribution of the overburden stress in the prototype:

$$N_g = \omega^2 \cdot R \tag{48}$$

where ω is the centrifuge angular velocity and R is the distance from the centrifuge axis of rotation. Thus, the stress field must be computed according equation 49 with reference to figure 3.10:

$$d\sigma_v = \rho \cdot g \cdot N \cdot dR \tag{49}$$

$$\sigma_v = \int_{R_s}^{R_1} \rho \cdot \omega^2 \cdot R \cdot dR = \frac{1}{2}\rho \cdot \omega^2 [R_1^2 - R_s^2] \tag{50}$$

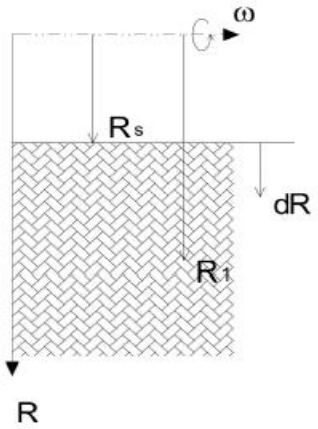

Figure 3.10- Distortion of centrifugal field (Airoldi et al., 2018)

where σ_v is the vertical overburden stress (Airoldi et al.,2018)

- The soil surface and the free water surface of the model are not flat.
- The boundary conditions of the model must be carefully designed in order to avoid side-effects during the test.
- For flow and dissipative events, the seepage velocity through a centrifuge model is subjected to an increase of self-weight of N times, it is N times larger than that in the prototype if the same soil and pore fluid are used and identical gradient applied. This inconsistency on velocity means that simulation of dynamic and diffusion events is not possible. In order to couple these two analyses, soil and pore fluid should be properly chosen. The most commonly adopted strategy consists in using the same soil and pore fluid with higher viscosity, but similar density of the prototype fluid (Allard and Shenkeveld 1994).

4. DESCRIPTION OF THE ISMGEO CENTRIFUGE TRIALS

4.1 Introduction

This work will focus on the treatment and interpretation of the data provided by thirty-seven centrifuge tests performed by the Istituto Sperimentale Modelli Geotecnici S.R.L. (ISMGEO) for the European project H2020-LIQUEFACT (GA. 700748) (www.liquefact.eu). In that sense, this chapter is dedicated to the introduction of those tests, including the description of the centrifuge machine, the input ground motions, the soil properties, the soil models and the mitigation techniques used, as well as the necessary assumptions used in the data treatment.

In the framework of the LIQUEFACT project, the centrifuge tests were aimed to produce a consistent set of experimental data to be used as a benchmark for seismic response studies, numerical simulations and in situ trial tests. The input motions were calibrated to bring the soil in a liquefied state and then to verify the effectiveness of different liquefaction mitigation techniques selected for the project.

A ground response analysis was carried out in the reference site to compute a series of representative ground motions suitable to be applied to the centrifuge models.

The thirty-seven tests, shown in Table 1, were organized in three series: the first one aimed at investigating the liquefaction triggering, the second and third ones finalized at analysing the effectiveness of three selected liquefaction mitigation techniques. Particularly, during the first test series, three sandy soils and five different earthquake input motions were tested, to define under which conditions liquefaction occurred. Some tests were carried out under free field condition, while in other tests a simple structure based on shallow foundations was modelled as well, in order to study the effects of soil structure interaction. In the second test series, vertical and horizontal drains were installed in the models, in order to analyse their effectiveness in reducing the pore pressure build up as function of their spacing. In the last series of tests, the effectiveness of the "Induced Partial Saturation" (IPS) technique on the soil liquefaction resistance was tested, i.e. the soil models were partially desaturated by air injection from the bottom of the models varying the number and position of the injectors.

Table 4.1- Model parameters of the 37 tests (Airoldi et al., 2018)

Series	Test Number	Test Name	Model Type	Sand	Ground Motion	Structure	Drains	IPS
1	1	M1_S1_GM17	1	1	17	-	-	
	2	M1_S1_GM34	1	1	34	-	-	
	3	M1_S1_GM31	1	1	31	-	-	
	4	M1_S2_GM17	1	2	17	-	-	
	5	M1_S2_GM23	1	2	23	-	-	
	6	M1_S2_GM34	1	2	34	-	-	
	7	M1_S3_GM17	1	3	17	-	-	
	8	M1_S3_GM23	1	3	23	-	-	
	9	M1_S3_GM34	1	3	34	-	-	
	10	M2_S1_GM34	2	1	34	-	-	
	11	M2_S1_GM31	2	1	31	-	-	
	12	M2_S3_GM34	2	3	34	-	-	
	13	M1F_S1_GM31	1	1	31	yes	-	
	14	M1F_S1_GM31+	1	1	31+	yes	-	
	15	M2F_S1_GM31+	2	1	31+	yes	-	
2	16	M1_S1_VD1_GM31	1	1	31	-	Vert. S=5D	-
	17	M1_S1_VD2_GM31	1	1	31	-	Vert. S=10D	-
	18	M1_S1_HD1_GM31	1	1	31	-	Horiz. S=5D	-
	19	M1_S1_HD2_GM31	1	1	31	-	Horiz. S=10D	-
	20	M2_S1_VD1_GM31	2	1	31	-	Vert. S=5D	-
	21	M2_S1_VD2_GM31	2	1	31	-	Vert. S=10D	-
	22	M2_S1_HD1_GM31	2	1	31	-	Horiz. S=5D	-

	23	M2_S1_HD2_GM31	2	1	31	-	Horiz. S=10D	-
	24	M1F_S1_VD1_GM31+	1	1	31+	yes	Vert. S=5D	-
	25	M1F_S1_HD1_GM31+	1	1	31+	yes	Horiz. S=5D	-
	26	M2F_S1_VD1_GM31+	2	1	31+	yes	Vert. S=5D	-
	27	M2F_S1_HD1_GM31+	2	1	31+	yes	Horiz. S=5D	-
3	28	M1_S1_IPS1_GM31	1	1	31	-	-	1 inj.
	29	M1_S1_IPS1_GM31+	1	1	31+	-	-	1 inj.
	30	M1_S1_IPS4_GM31	1	1	31	-	-	4 inj.
	31	M1_S1_IPS4_GM31+	1	1	31+	-	-	4 inj.
	32	M2_S1_IPS1_GM31	2	1	31	-	-	1 inj.
	33	M2_S1_IPS1_GM31+	2	1	31+	-	-	1 inj.
	34	M2_S1_IPS4_GM31	2	1	31	-	-	4 inj.
	35	M2_S1_IPS4_GM31+	2	1	31+	-	-	4 inj.
	36	M1F_S1_IPS4_GM31+	1	1	31+	Yes	-	4 inj.
	37	M1F_S1_IPS4_GM31++	1	1	31++	Yes	-	4 inj.

All the models are composed by a sand layer with or without an over consolidated clay crust in profiles of different heights of about 15 meters.

Different layouts of the pore pressure transducers, displacement transducers and accelerometers were arranged among the models, as described model by model in the following.

The chapter is composed by a description of the centrifuge machine as well as a description of the models divided by soil properties, soil profiles, structural elements, sensor arrangement and instrumentation of the mitigation techniques. A further section about the applied ground motions will be contained in this chapter, concluding wih the treatment of the data that is analysed in this work.

4.2 Centrifuge machine description

The ISMGEO geotechnical centrifuge is a beam with a symmetrical arm. A swinging basket is positioned into a part of the arm, where the soil model will be subsequently placed into the basket. A weight is placed into the opposite side of the arm in order to guarantee the equilibrium during rotation. The length of the whole arm is 6 m, the height is 2 m, and the width is equal to 1m. It is also important to underline the distance of the model base from the central axis of the centrifuge, which is 2.2 m. More technical details and dimensions can be found in the illustrative scheme below, Figure 4.1.

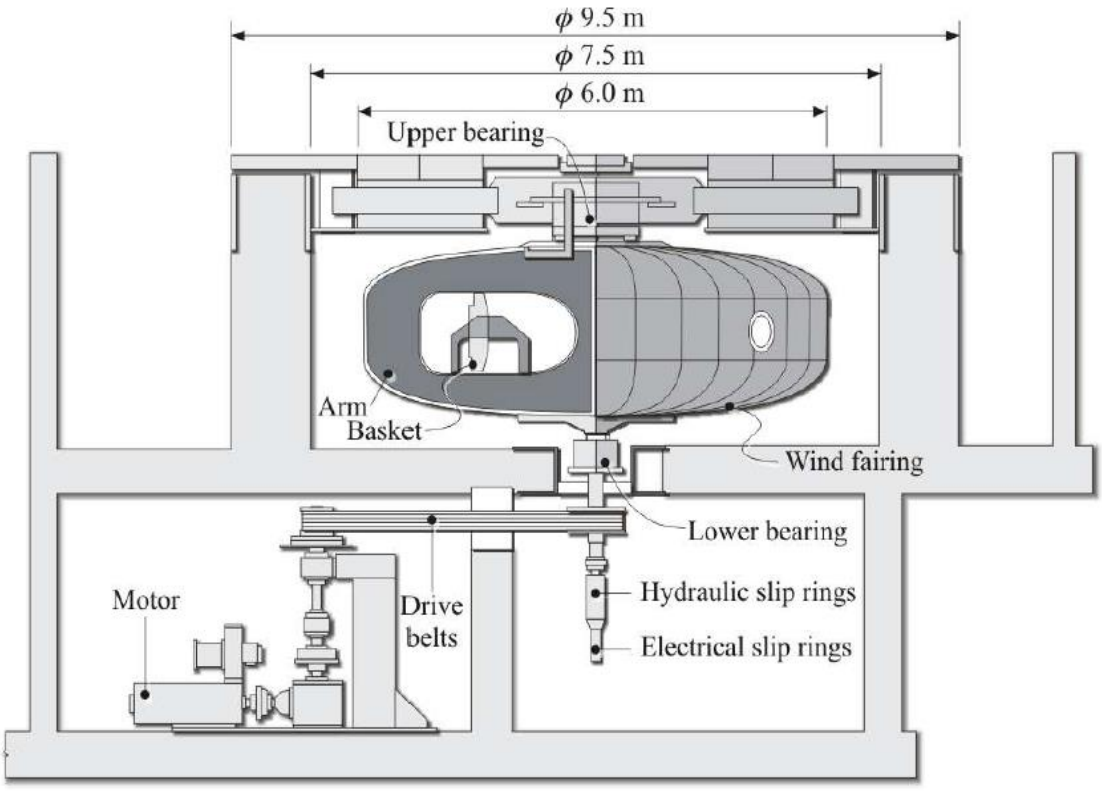

Figure 4.1-Cross section scheme of ISMGEO geotechnical centrifuge (Airoldi et al., 2018)

An outer fairing covers the arm and they concurrently rotate limiting the air friction during the flight. The capacity of the centrifuge is 240 g-ton, i.e. the machine can reach an acceleration of 600 g with a payload of 400 kg. Moreover, the unusual shape of the ISMGEO centrifuge gives it the following features: small distortion of the centrifugal field in the model, since its main dimension is parallel to the rotation axis; low deflection of the support plane of the swinging basket; easy location of the instruments close to the rotation axis because of the absence of a central shaft across the arm.

During the flight, the basket containing the model turns of 90° reaching a position perpendicular to the main rotation axis. A shaking table is also fixed on the extremity of the arm housing the model. The shaker is single-degree-of-freedom table able to simulate a real strong motion at the model scale. As soon as the container reaches the vertical position, the shaking table is moved into contact with the model and the shock is simulated.

It is also useful to give a small description of the model container: an Equivalent Shear Beam (ESB) container was designed on purpose. The main goal of the design was to impose to the box a boundary condition suited to simulate the real behaviour of the soil column. In order to mitigate the boundary effects, the ESB box was conceived with a laminar configuration; actually, it is composed by a high number of very thin rigid frames connected by rubber inter-layers, which have the function of avoiding the boundary effects.

4.3 Soil properties

In order to analyse the seismic behaviour of loose sands three representative sandy soils were selected.

Ticino clean sand was one of the chosen soils since it is a well-studied soil in geotechnical laboratories specially in the last years. Ticino Sand is a uniform coarse-to-medium sand of angular to sub-rounded particles, composed by 30% quartz, 65% feldspar and 5% mica. The dry densities and the relative densities of Ticino Sand were provided test by test (in the table it is shown the interval of the values). The permeability coefficient k, the maximum void index (e_{max}) and the minimum one (e_{min}) were reported in the test description and the shear friction angle was obtained from Mele et al. (2018). The initial shear modulus G_0 was calculated by the shear wave velocity V_s (provided in the test results) as:

$$G_0 = \rho V_s^2$$

The second tested sand was a clean sand retrieved from the site of Pieve di Cento, located near to the localities of San Carlo and Mirabello, where liquefaction phenomenon occurred during the Emilia-Romagna earthquake 2012. This site was also the place of a field trial prepared in the scope of LIQUEFACT project, where liquefaction was induced by a mega-shaker. However, from grain size analysis, Pieve di Cento sand resulted slightly different from the sand that liquefied during the 2012 earthquakes. This sand was obtained by natural Pieve di Cento sieved at the N.200 ASTM sieve. As already mentioned for the Ticino Sand, the dry and relative densities were attached in the test (in the table it is shown the interval of the values);

the permeability coefficient k, the maximum void index (e_{max}) and the minimum one (e_{min}) were reported in the test description; finally, the shear modulus G_0 and the shear friction angle were obtained from Mele et al. (2018).

The third and last tested sand was natural Pieve di Cento, i.e. a fine sand with a fine content of 12%. The same properties of clean Pieve di Cento Sand were adopted for natural one, with exception of the maximum void ratios (e_{max} and e_{min}), the dry and relative densities (in the table it is shown the interval of the values), whose values were summarized in the test result sheets.

In order to simulate a soil profile with a surface layer of fine-grained soil Pontida clay (Fioravante and Jamiolkowski, 2005) was adopted. Each layer was prepared as follows: dry clay powder was placed in a mixer and the appropriate amount of deaired tap water was added to achieve a water content equal to 42% (1.75 times the liquid limit). Mixing was continued for about two hours under a vacuum of 750 mm Hg. The clay slurry was then transferred with a spoon into a consolidometer until an unconsolidated specimen height of 50 mm was obtained. Filter paper and porous disks were placed at the top and bottom of the specimen. During the loading stage, the consolidometer was placed under a rigid reaction frame. The loading steps applied were: 6, 12.5, 25, 50, 100, 200 kPa. The specimen height after consolidation was approximately equal to 30 mm. The time required to achieve full consolidation was about 13 days. After the consolidation phase the specimen was unloaded, removed from the consolidometer and placed above the sand model surface just before the test. Under the centrifugal field the clay layer had an over consolidation ratio OCR larger than 20.

Table 4.2- Soil properties of the 4 soils and origin of the data (Airoldi et al., 2018)

	Ticino Sand	Clean Pieve di Cento	Natural Pieve di Cento	Pontida Clay
Dry density ρ_d [kg/m^3]	1503 to 1552[1]	1388 to 1491[1]	1425 to 1500[1]	2160[1]
Relative density D_r [-]	0.46 to 0.57[1]	0.46 to 0.7[1]	0.46 to 0.7[1]	(-)
Poisson ratio ν [-]	0.3[3]	0.3[3]	0.3[3]	0.35[3]
Soil cohesion c' [kPa]	0[3]	0[3]	0[3]	50[3]
Soil dilation Ψ [°]	0[3]	0[3]	0[3]	(-)
Soil tension σ_t [kPa]	0[3]	0[3]	0[3]	(-)
Shear angle ϕ_{cv} [°]	34[2]	33[2]	33[2]	(-)
Permeability K [m/s]	1.66 E-03[1]	8.69 E-05[1]	8.69 E-05[1]	1.00 E-08[2]
e_{min} [-]	0.574[1]	0.674[1]	0.674[1]	(-)
e_{max} [-]	0.923[1]	1.101[1]	1.101[1]	(-)
G [MPa]	94.4[1]	45[2]	45[2]	50[2]

[1]	Airoldi et al. (2018)
[2]	Mele et al. (2018)
[3]	Tipycal values

4.4 Soil profile

Two main soil profiles were tested in the 37 cases: model 1 consists of an homogeneous sandy deposit and model 2 is a two layer profile with a sand layer topped by a 1.5 m clayey soil layer. Since model 1 has some variations in the height, it was decided to divide it into three separate sub-models. In this way, a soil profile results from a combination of these three sub-models and the model 2. A more effective visual description is provided in Table 4.3 and Figure 4.2.

Table 4.3- Model 1 with 3 sandy profiles (a, b and c) and model

		Depth (m)	Soil
Model 1	Sub-model a	12.5	sand
	Sub-model b	14	sand
	Sub-model c	15.5	sand
Model 2		1.5	clay
		14	sand

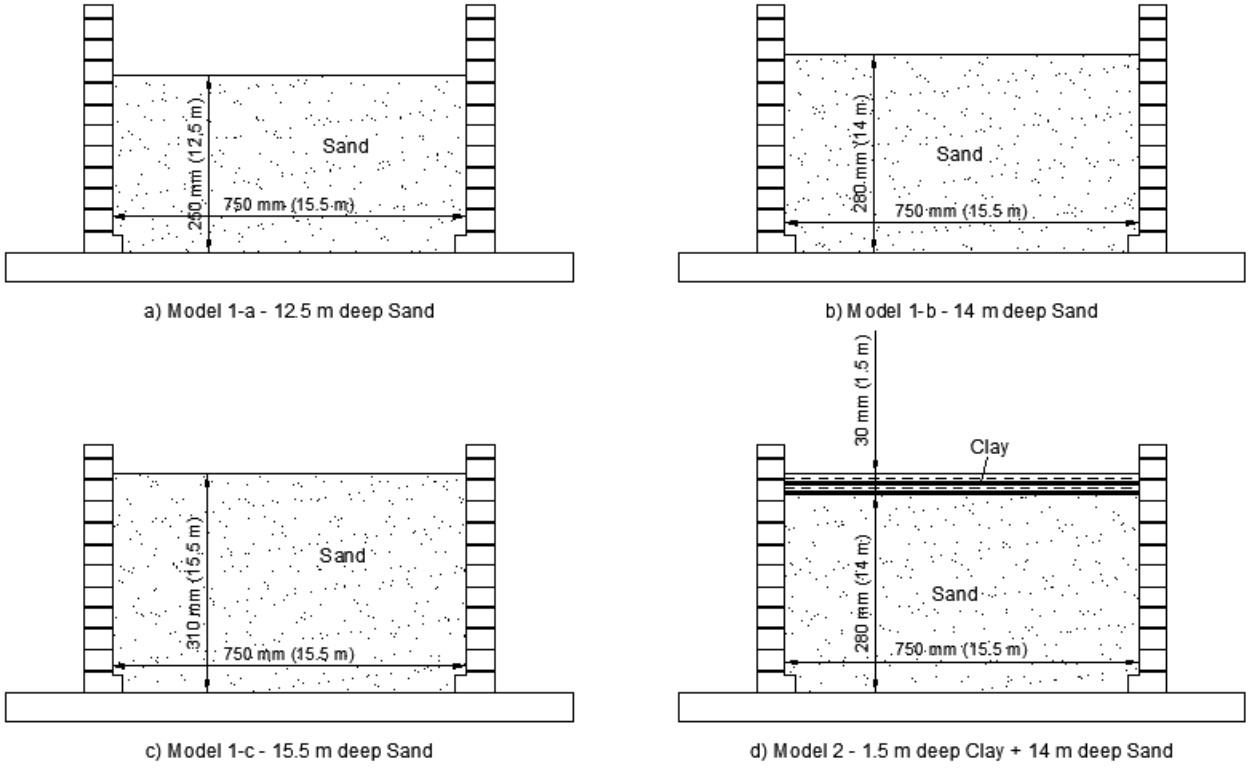

Figure 4.2-Model 1 with 3 sandy profiles (a, b and c) and model 2

4.5 Structural properties

The single-degree of freedom structure was designed comprising two different materials for the foundation and the oscillating part. The oscillating part is formed by steel plates as beam and columns; the strip foundations, made by aluminium, are embedded 3 cm (1.5 m at prototype scale). The entir model has mass of 2 kg. A graphic illustration with the geometrical properties of the building is showed in Figure 4.3.

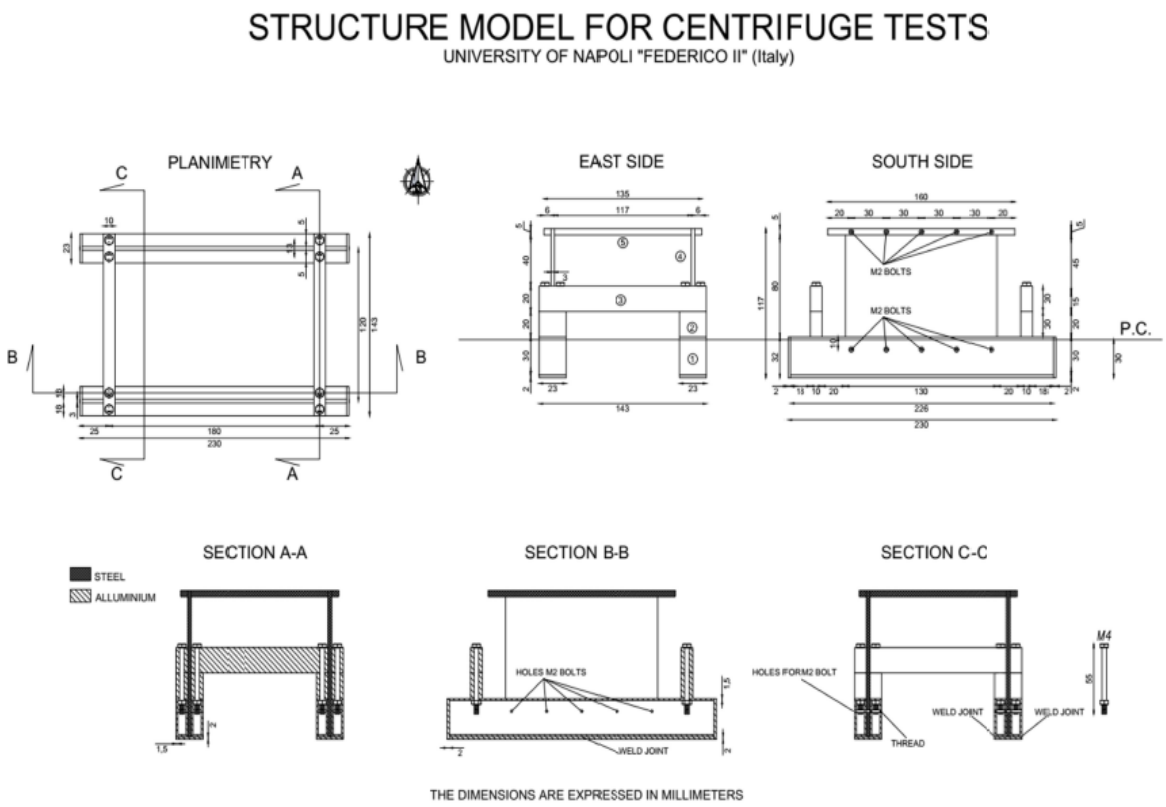

Figure 4.3- Structure Model (Airoldi et al., 2018)

Since only the weight of the entire building was available and the properties of the structural material were not known, the relative mass percentages for the building and the foundations were determined based on the volume ratio, obtained from the drawing. Moreover, the geometrical dimensions of the structural elements were evaluated from the given graphic illustration and a characteristic Young modulus of plain concrete was assumed for the foundations, as it is the most realistic Young modulus when compared with the aluminium used for the foundation.

A shear type behaviour was assumed for the superstructure, consequently the mass ratio has a unitary value and the effective height is equal to the entire one; it is also highlighted that in a shear type model the centre of mass is in the geometric centre of the upper plate.

The main oscillation frequency of the superstructure was provided by Airoldi et al. (2018) and thus the period was calculated.

A complete representation of the structural properties is provided in Table 4.4.

Table 4.4- Structural properties in prototype scale: a) superstructure and b) foundation

Superstructure	
Effective height [m]	4.25
Effective mass [t]	140
Period [s]	0.32
Mass ratio [-]	1

a)

Foundation	
Length [m]	11.3
Width [m]	2.3
Height [m]	1.5
Young Modulus E [GPa]	200
Depth [m]	1
Mass [t]	93

b)

4.6 Location of the sensors

The name of the sensors was standardised so that the user can easily understand where the sensor is, and to improve communication between different researchers as defended by Millen et al. (2018) and Rios et al. (2019). In that sense, a set of default names proposed in eng-tools (2018) was adapted for the present case as explained in what follows.

All the sensors follow the same naming system, “sensor’s name” - “X coordinate” - “Y coordenate” - “Z coordenate”, whose axis system is represented in Figure 4.4.

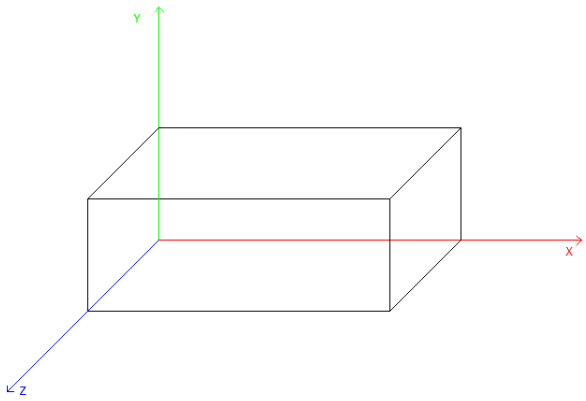

Figure 4.4-Axis system

There are three types of sensors that were used in the test program: Acceleration transducer, named “ACCX” as the acceleration values are determined for the X axis; Pore Pressure

Transducer, named “PPT”; Displacement transducer, named “DISPY” as the displacement was measured in the Y axis.

For the X coordinates, a division of the codes was made as to whether the model had a structure or not. Being so, the soil was divided in vertical columns located and named from North to South, including, when existent, the indication of the area influenced by the structure. In Figures 4.6 and 4.8 it is shown the models with building and in Figures 4.5 and 4.7 it is shown the models without building. In the figures it is also shown the length in percentage of each coordinate and on Table 4.5 are the full names of the codes used for the X coordenates.

Table 4.5-Convention for the X coordinate codes

X Coordinates	
FF	Free Field
FFN	Free Field North
FFS	Free Field South
FFNW	Free Field North Wall
FFSW	Free Field South Wall
UB1	Under Building 1
UNB1	Under North Building 1
USB1	Under South Building 1
FFB1N	Between Free Field and Building 1 North
FFB1S	Between Free Field and Building 1 South

In terms of the Y coordinates, two divisions of the profile had to be distinguished, as to wether it was Model 1 or Model 2. For the division concerning the Model 1, the surface and bottom sublayers amplitude were fixed at 5% of the total profile depth and the remaining 90% was equally divided into five more sublayers, as shown in Figures 4.5 and 4.6. In the second one, related to Model 2, the surface sublayer is only on the clayey layer and the bottom sublayer is exclusively in the coarse-grained layer. In order to compare the two layer model with the one layer model so that transducers that are at the same relative position in both models get similar names, the percentages of layer height associated to each sub-layer were adjusted as indicated in the figures 4.5 and 4.6. In particular, the percentage associated to the bottom of the clay layer was joined with the one immediately above (L1B), as well as the percentage associated to the surface sublayer of the sand layer which was joined with the sublayer immediately below (L2T).

This way the center sublayer are in the same position in both models and therefore, a sensor located in the layer center is in the same relative position in both models. In the figures it is also shown the height in percentage of each coordinate and on Table 4.6 are the full names of the codes used for the Y coordinates.

Table 4.6- Convention for the Y coordinate codes

Y Coordinates	
S	Surface
L1T	Layer 1 Top
L1TC	Layer 1 Top Centre
L1C	Layer 1 Centre
L1BC	Layer 1 Bottom Centre
L1B	Layer 1 Bottom
B	Bottom
L2	Layer 2

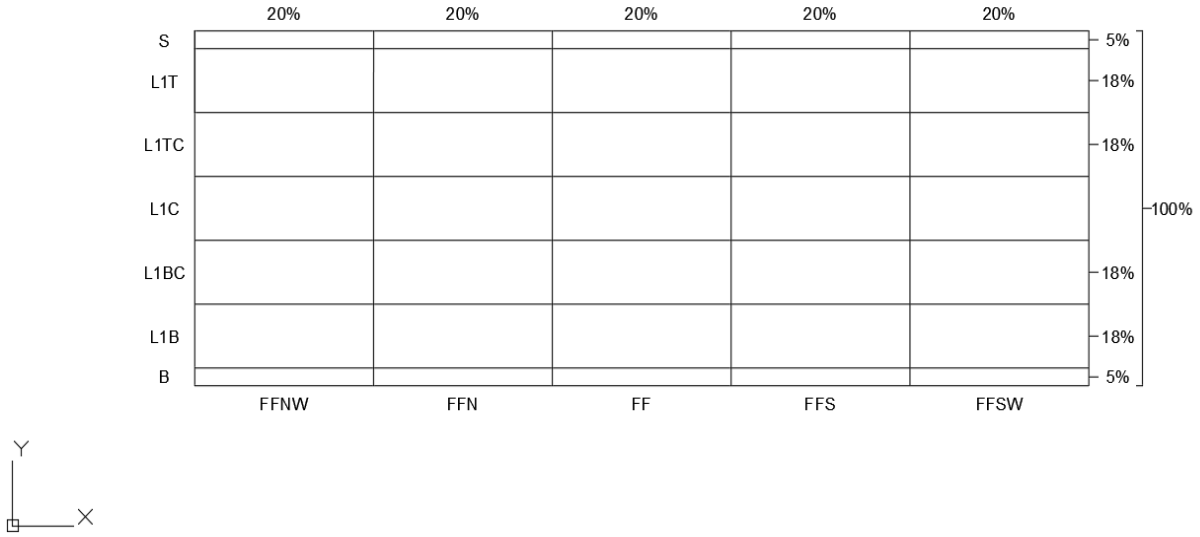

Figure 4.5- Model 1 without building

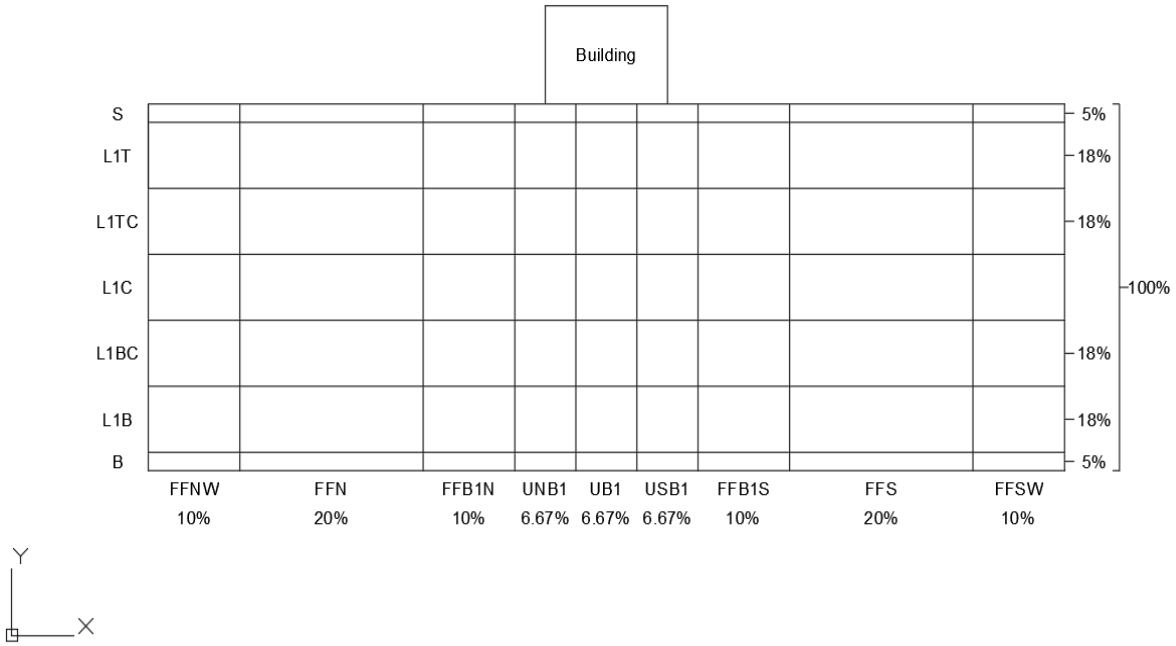

Figure 4.6- Model 1 with building

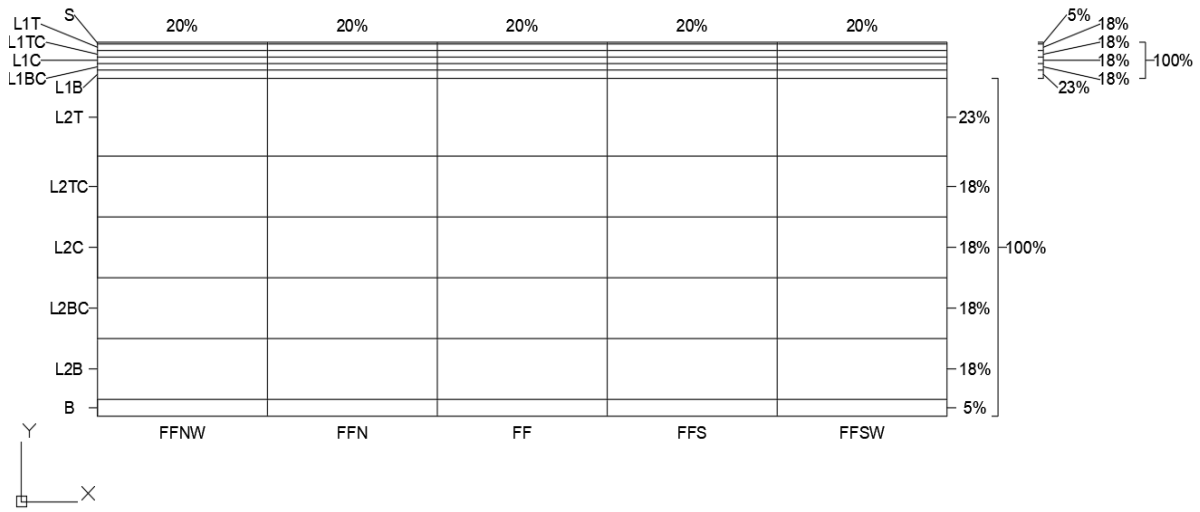

Figure 4.7-Model 2 without building

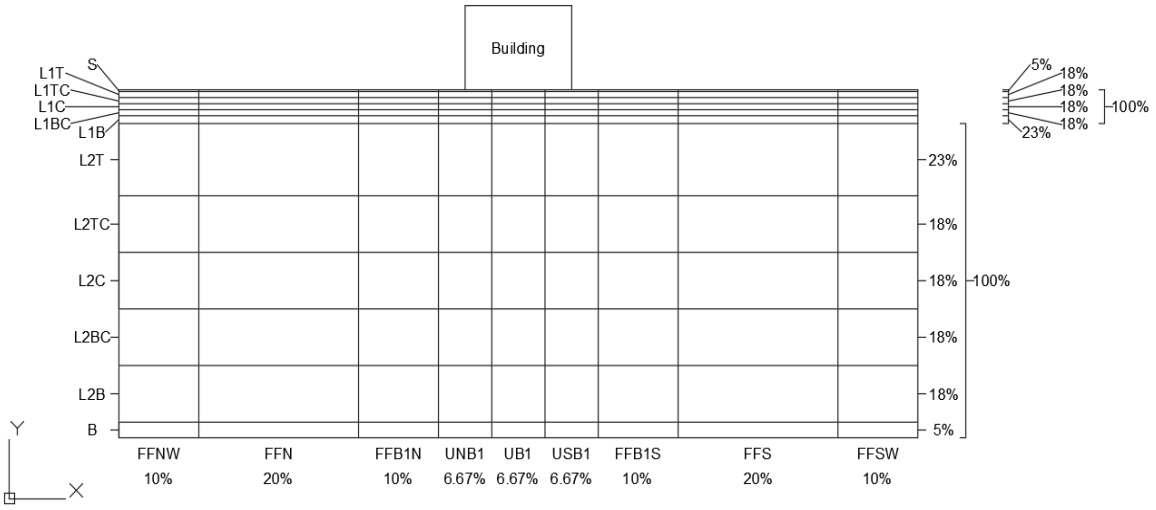

Figure 4.8-Model 2 with building

Concerning the Z coordinates, most of the sensors were arranged along a plane crossing the middle of the models' width. In the models with a building there were also 3 more displacement sensors added: one in the front of the ESB container, two in its back. On the Table 7 it is shown the convencion for the Z coordinates and in the Figure 4.9 it is shown a top view of the model with the Z coordinates.

Table 4.7- Convention for the Z coordinate codes

Z Coordinates	
B	Back
M	Middle
F	Front

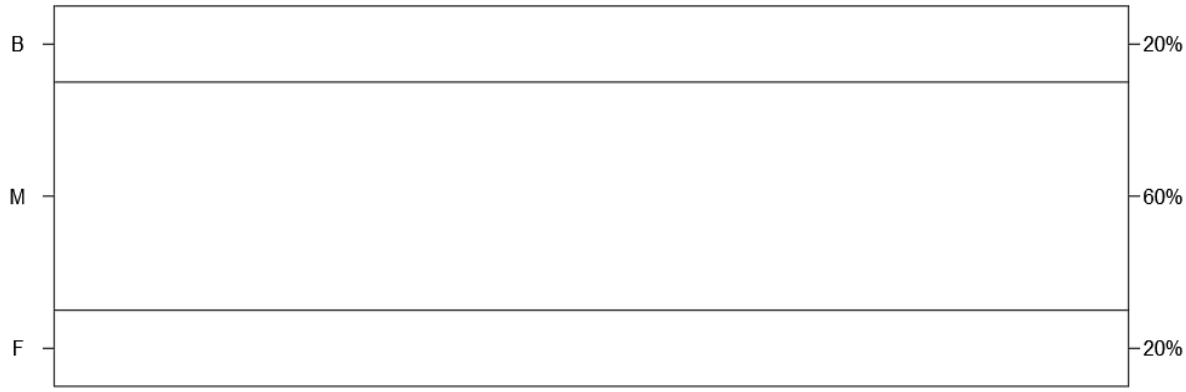

Figure 4.9- Top view of the model with the Z coordinates

4.7 Instrumentation of the mitigation techniques

As it was referred on the introduction of this chapter, 2 mitigation techniques are analysed in the test plan: Drains and Induced Partial Saturation (IPS).

4.7.1 Drains

There are 2 distinct configurations for the drains, one vertical and one horizontal.

The drains were simulated using silicone pipes with an external diameter of 6 mm and an internal diameter of 4 mm. In each pipe, a pair of holes with 0.5 mm diameter was made, along its length, spacing 5 mm between themselves.

The vertical drains were disposed in square arrangements, spaced 5 or 10 times their diameter (30 or 60 mm in the model, corresponding to 1.5 or 3 m in the prototype scale), depending on the test. Figure 4.10 shows a sketch of the vertical drains arrangement while Figure 4.11 shows the top view of a model with the vertical drains, accompanied by the main dimensions.

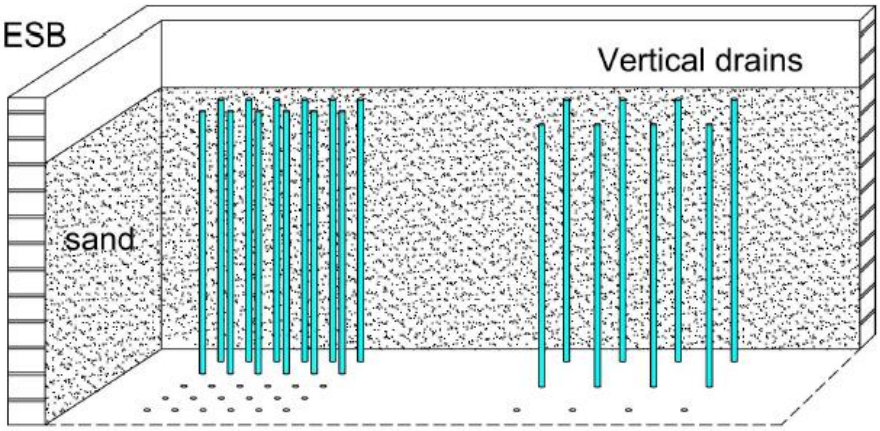

Figure 4.10- Sketch of a model with vertical drains (Airoldi et al., 2018)

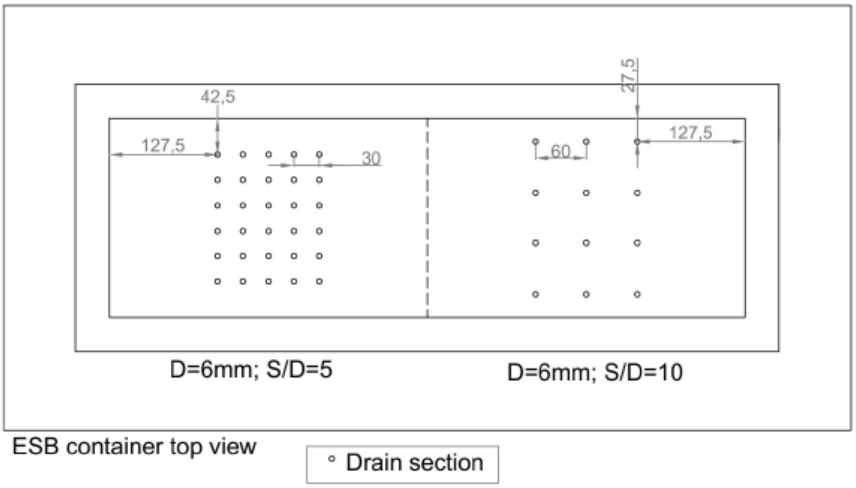

Figure 4.11- Top view of a model with vertical drains (Airoldi et al., 2018)

The horizontal drains were installed at a predefined depth and connected to three horizontal header pipes, with 12 mm, installed along the model's width, perpendicularly to the main drains. These header pipes were in turn connected to four vertical columns located in the corners of the models and filled with gravel up to the ground surface.

The disposition of the horizontal drains was according to a quincunx mesh, spaced 5 or 10 times their diameter (30 or 60 mm in the model, corresponding to 1.5 or 3 m in the prototype scale), depending on the test. Figure 4.12 shows a sketch of the horizontal drains and Figure 4.13 shows the frontal view of a model with the horizontal drains, accompanied by the main dimensions.

In this work the named of the drains is going to be simplified as shown in the Table 4.8.

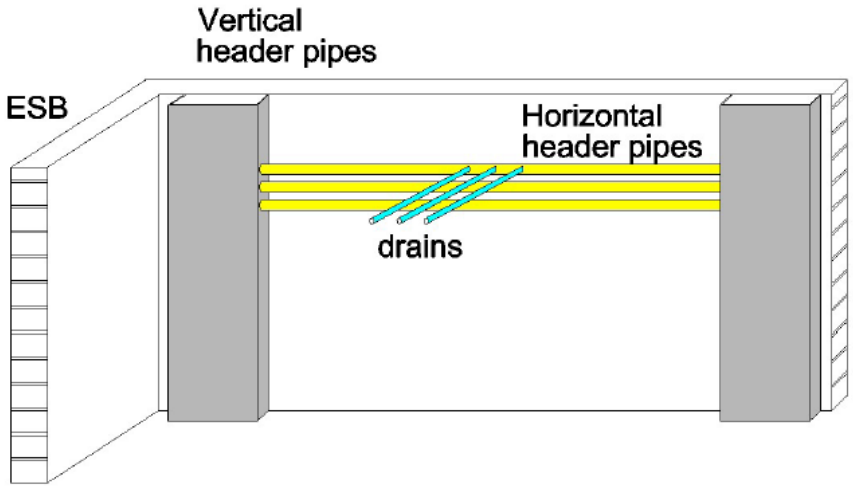

Figure 4.12- Sketch of a model with horizontal drains (Airoldi et al., 2018)

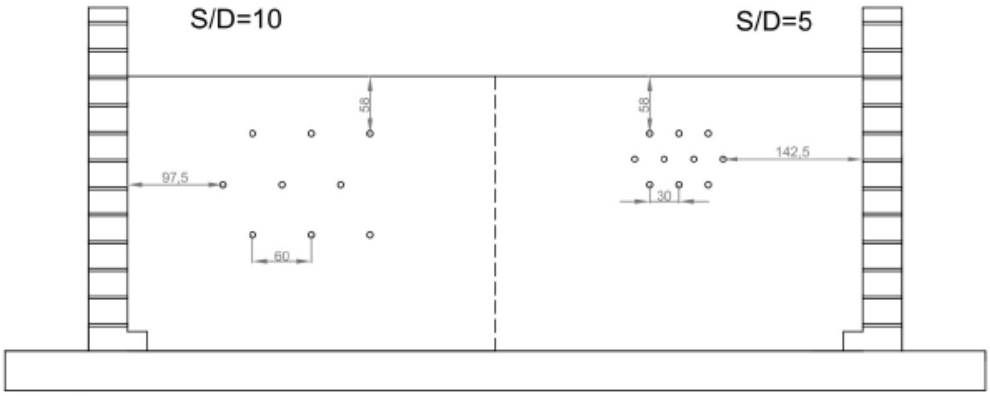

Figure 4.13- Side view of a model with horizontal drains (Airoldi et al., 2018)

Table 4.8-Convention for the drains codes

Drains	
V1	Dense arrangement of vertical drains
V2	Loose arrangement of vertical drains
H1	Dense arrangement of horizontal drains
H2	Loose arrangement of horizontal drains

4.7.2 Induced Partial Saturation

The system to simulate the air injection was composed by two air reservoirs, an air pressure transducer, a solenoid valve and connection pipes that go down to the injectors placed in the base of the model, as shown in Figure 4.14.

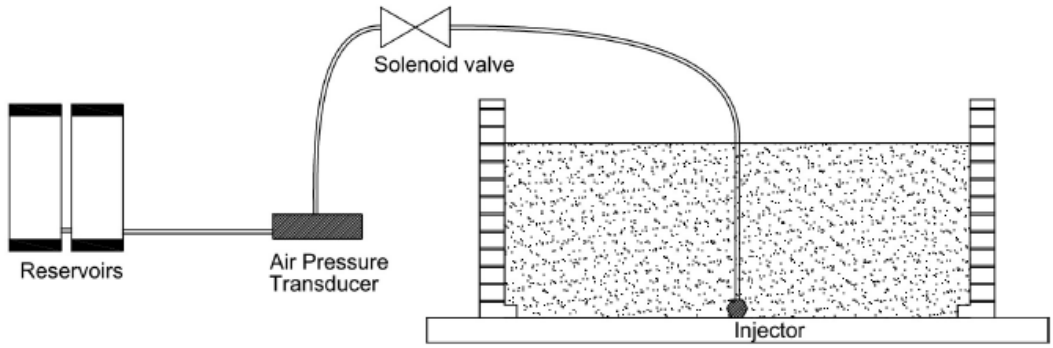

Figure 4.14- Sketch of a model with IPS (Airoldi et al., 2018)

There were two configurations for the air injection system, single injector and multiple injector array. In this work, both configurations have their names simplified as shown in Table 4.9.

The single injector consisted in a nozzle with 1.3 cm in diameter and an injection surface of 1.33 cm². This injector was placed in the centre of the model.

The multiple injector array was composed of 4 nozzles with a effective diameter of 0.9 cm, spaced 6 cm from each other and with a global surface injection of 2.54 cm². The array was placed along the length of the model, spread 18 cm along the central part.

Table 4.9- Convention for the IPS

Induced Partial Saturation (IPS)	
IPS1	1 injector
IPS4	4 injectors

4.8 Input ground motions

A specific site response analysis was carried out by the university UNIPV in order to obtain a series of representative ground motions, each one with an intensity corresponding to a particular return period. In order to obtain a better estimation of the representative shock, the seismic motions were evaluated at a depth of 15 m, i.e. the approximate depth of the soil profile in the prototype.

Then the computed recordings needed to be modified in order to be adapted to the shaking table, i.e. the maximum frequency and the acceleration values were limited to 10 Hz and 0.3g respectively, which are reasonable limit values of a seismic event.

The selected input motions were subsequently scaled and finally applied to the models to investigate the liquefaction triggering conditions. Full liquefaction conditions were achieved only with GM31, corresponding to a return period T_R of 2475 years and a moment magnitude M_w of 6.9. In some cases, in order to lead the model to the liquefied condition it was necessary to increase the amplitude of the input shocks, obtaining one more motion, called GM31+. A summarized version of the ground motion characteristics is provided on Table 4.10.

Table 4.10- Ground motion characteristics

Return period T_R (years)	Ground motion ID	Moment magnitude M_W
475	GM17	6.1
975	GM23	5.9
2475	GM31	6.9
2475	GM31+	6.9
2475	GM34	6.93

4.9 Treatment of the data

4.9.1 Application of the scaling law

Acceleration, pore pressure and displacement values were registered for a given period of time. These values are subjected to the scaling law described in detail in Chapter 2, Section XXX, whose scaling factor is N=50 (i.e. 1 second in the prototype corresponds to 0.02 s in model). Table 4.11 shows the parameters subjected to the scaling law, alongside with the ratio for each one. The values of all these parameters were all changed to their respective SI units during the conversion.

Table 4.11- Parameters subjected to the scaling law

Parameter	Model	Prototype
Time (s)	t	t x N
Acceleration (m/s²)	a	a / N
Pore pressure (kPa)	σ	σ
Displacement (m)	d	d x N

4.9.2 Calibration of the data

In the treatment of the registered acceleration records, the average was removed in the first 5 seconds to fix issues related to the zero-calibration of the equipment and tilt of the sensor before the cyclic event. In addition, a high pass filter at 0.1Hz and a low pass filter at 20Hz were used. The former aims at removing issues caused by sensor tilting during the event, and the latter removes any unwanted high frequency noise related to the recording equipment. Since

the main background noise is at 4Hz, shown in Figure 4.15, cannot be removed, so only frequencies well above the important frequency content of the ground motion are cleaned.

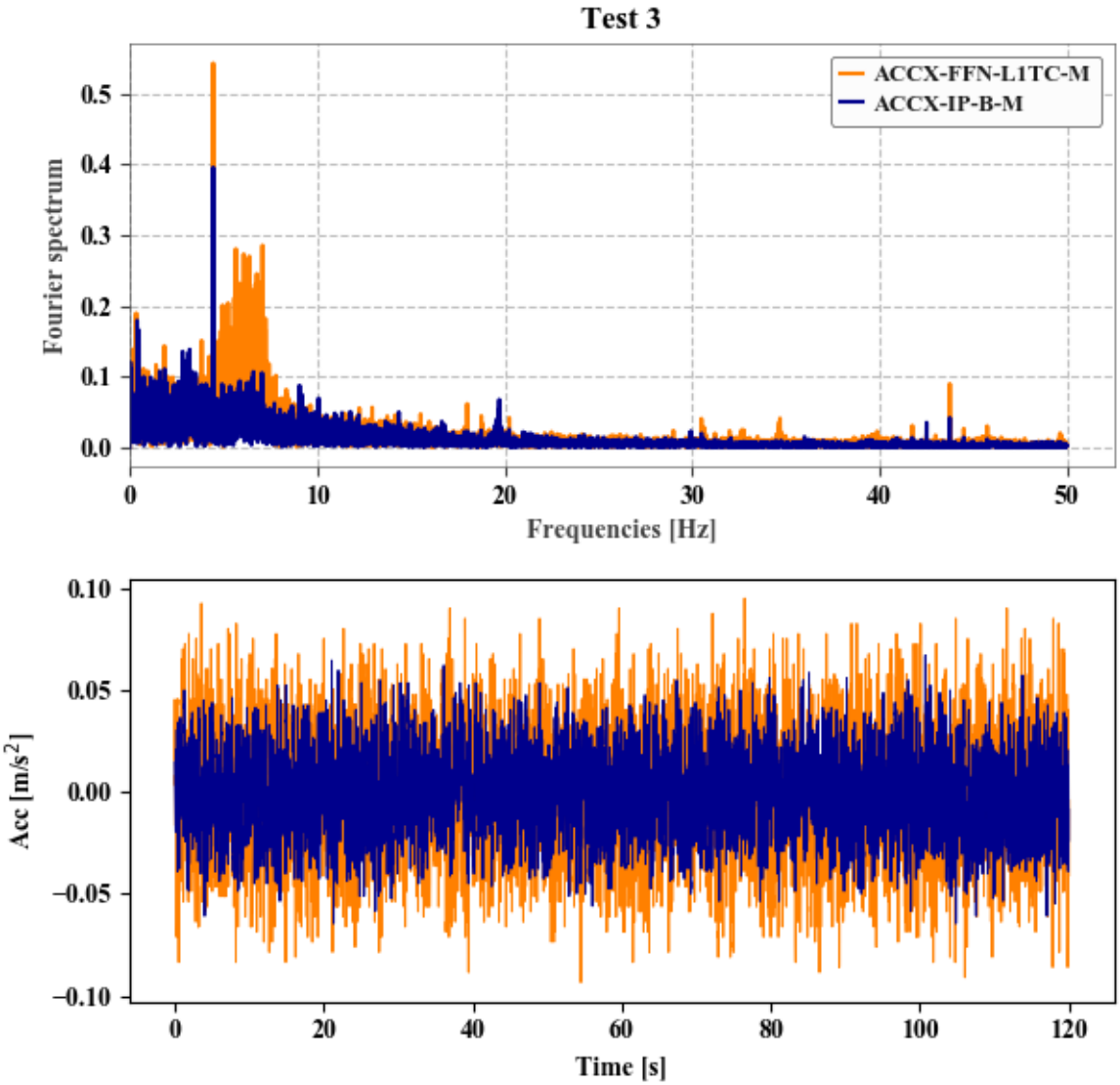

Figure 4.15-Noise of the acceleration records

The records were also trimmed to leave only the significant part of the event together with 10 seconds before and 20 seconds after. Since the record had a faint oscillating background acceleration, this trimming at the start caused a bias acceleration at the start, resulting in a non-zero average velocity. This was removed by calculating the acceleration, and then removing it over a two second window at the start of the record. In this two second window the acceleration was set zero at the start so that the record can be used in numerical modelling (which require records with zero at the start).

Moreover, in the case of test 14, there was clear evidence of sensor failure in the base acceleration sensor for short time durations (<0.03s) where the acceleration values would spontaneously go to values of approximately 45 m/s^2, far exceeding the maximum negative value of -1.57m/s^2 (and these acceleration spikes were not observed in the other acceleration sensors), these values were replaced through linear interpolation before filtering to obtain a physically realistic time series.

5. DATA ANALISYS

5.1 Introduction

In this chapter, the centrifuge results presented in the previous chapter and converted to the prototype scale are analysed. The most relevant aspects will be described in the following.

From the 37 tests provided, only 21 are treated in depth in order to simplify the analyses. As there were several tests with more than one variable between them, it was needed to crop the tests to 21 so that each variable difference could be clearly noticed in the results. Following this idea, the test results are obtained using ground motions GM31 for the free-field condition and GM31+ in the presence of a building (building condition).

In the free-field condition (Table 5.1), the following tests are treated: 1 test with no mitigation techniques, 4 tests with drains (2 vertical, with dense and loose arrangements, and 2 horizontal, with dense and loose arrangement) and 2 tests with IPS (1 injection and 4 injections), for both model 1-b and model 2, introduced in the previous chapter on Section 4.4.

Table 5.1-Test numbers corresponding to the treated tests in free-field condition

Free-Field Analyses							
Models	No Mitigaton Techniques	Mitigation Techniques					
		Drains				IPS	
		V1	V2	H1	H2	IPS1	IPS4
Model 1 - b	3	16	17	18	19	28	30
Model 2	11	20	21	22	23	32	34

As for the building condition (Table 5.2), the analysed tests are: 1 test with no mitigation techniques, 2 tests with drains (one vertical and one horizontal, both with dense arrangements), for both model 1-b and model 2, and 1 last test with IPS (1 injection) for model 1-b. There was no test with a building and IPS on model 2 from the 37 tests carried out.

Table 5. 2-Test numbers corresponding to the treated tests where a building is placed on the model

Building Analyses				
Models	No Mitigaton Techniques	Mitigation Techniques		
		Drains		IPS
		V1	H1	IPS1
Model 1 - b	14	24	25	36
Model 2	15	26	27	-

In this chapter, three main variables are treated, corresponding to the three types of sensors used in the models: acceleration, pore pressure and settlements.

An analysis of the ground motion change from bottom to surface due to ground response is described in order to compare with the behaviour that has already been theoretically described in the Chapter 2. This analysis has been carried out only in the free field condition since it was considered the most adapted for the analyses. For the analysed tests, the focused shaking parameters are: acceleration history, Fourier spectrum and Stockwell transform. At first, the analysis is carried out in terms of Fourier spectra by means of the *Fourier amplification function*; subsequently, the variation of the frequency content during the ground motion is studied on the Stockwell function.

The pore pressure analysis is carried out in three sections: initially, a model validation is performed by means of the comparation between the initial values of the pore pressure in the model and the theoretical hydrostatic pore pressure distribution on the site; then, the pore pressure build-up is evaluated through the pore pressure ratio (r_u); finally, the seepage in the box during and after the motions is described as well.

Concerning the settlements, a comparison between different models is shown in order to demonstrate the effectiveness of the mitigation measure in terms of settlement attenuation.

5.2 Analysis of the ground motions

5.2.1 Fourier *Amplification Function*

The way in which a ground motion is modified passing through a liquefied soil (as presented in the Figure 2.18) is practically showed by means of the comparison between the *Fourier Amplification Function* calculated for the tests number 11 and 20.

Both models are composed by 14 m of Ticino Sand covered by 1.5 m of Pontida clay and the acceleration history applied to the model is GM31.

These two tests were selected as representative: in the first one (Test 11), without mitigation measures, the pore pressure ratio raised during the motion, achieving a maximum value of r_u=0.86; on the second (Test 20), the presence of a dense arrangement of vertical drains prevented the increase of pore pressure.

To obtain the *Fourier Amplification Function*, the acceleration time series at the bottom and near to the surface and the corresponding *Fourier Spectra* are required. Thus, these two shaking parameters are shown in Figures 5.1 and 5.2 for both tests.

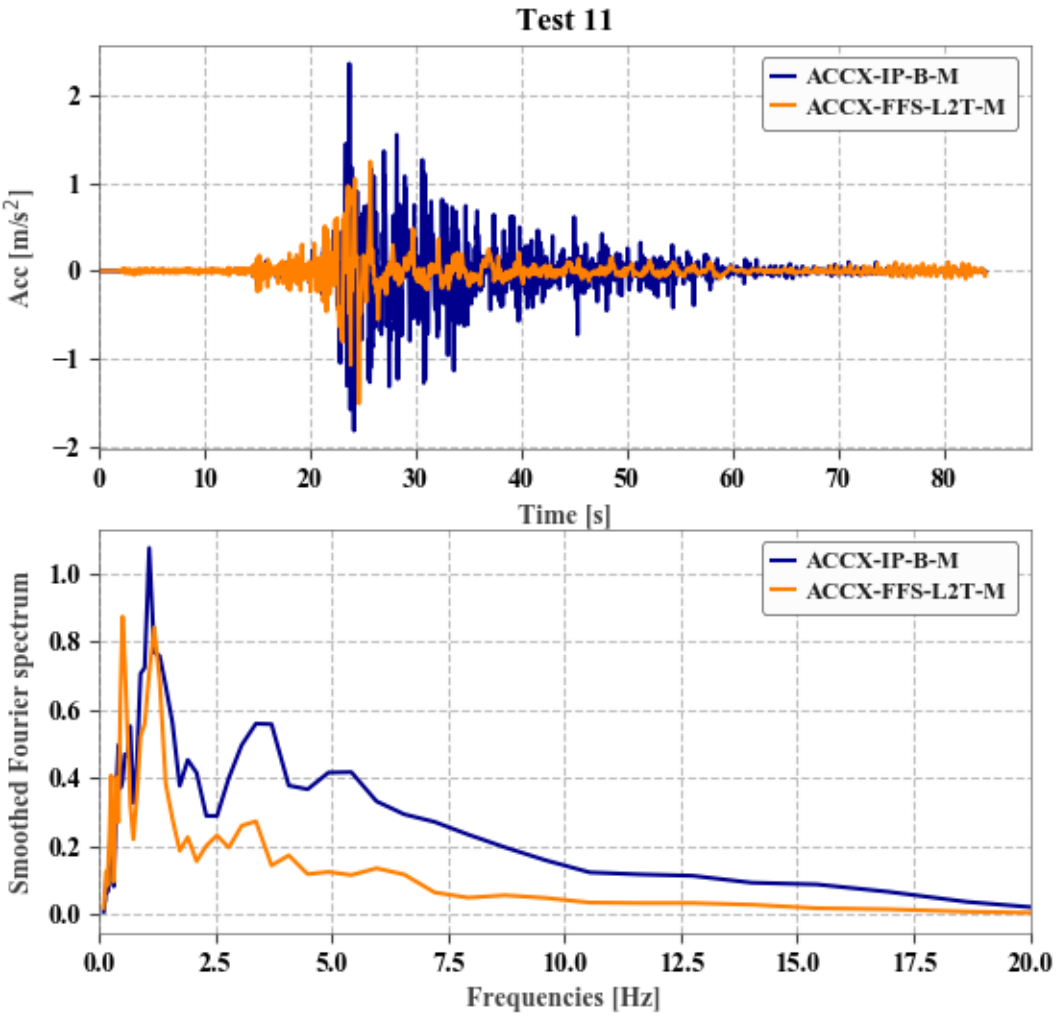

Figure 5.1- Acceleration series and Fourier spectrum of Test 11

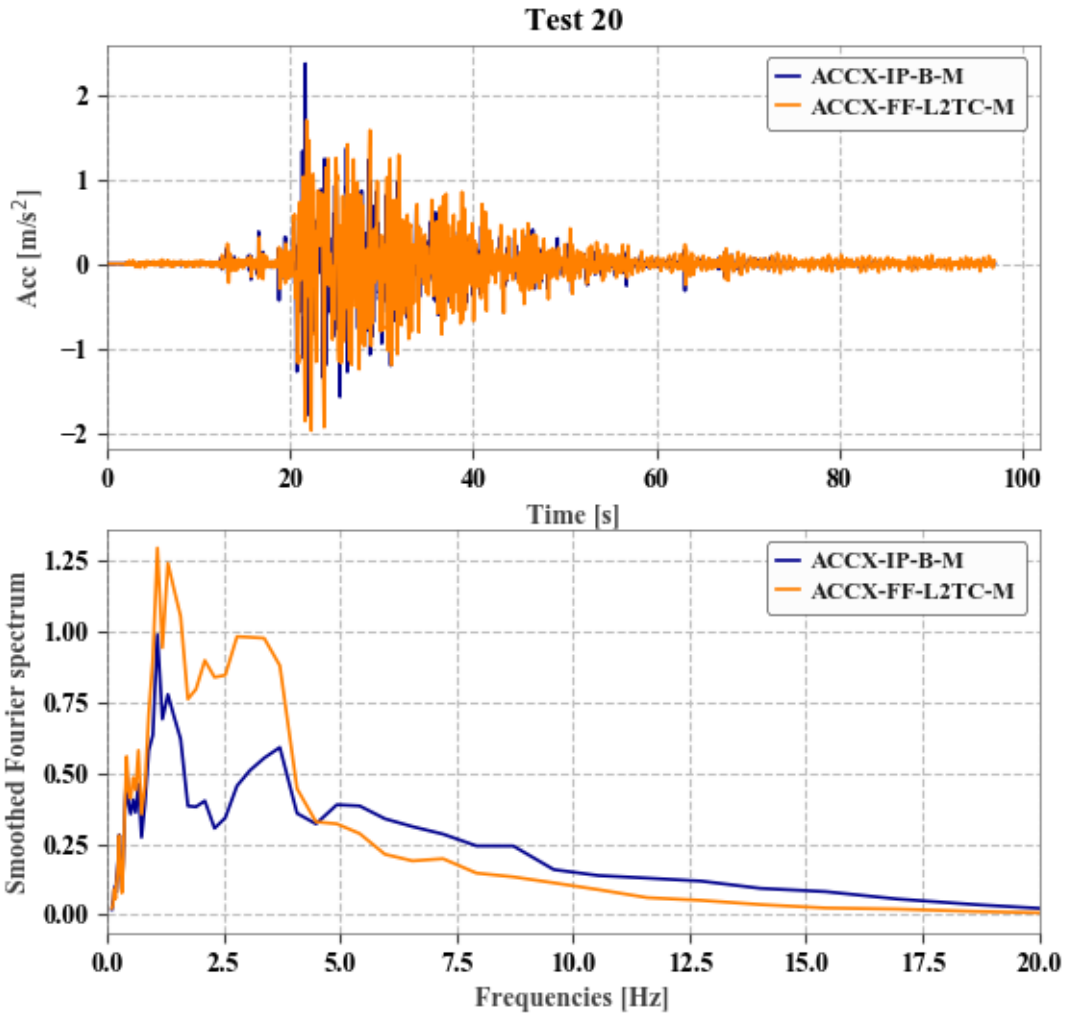

Figure 5.2-Acceleration series and Fourier spectrum of Test 20

Concerning the Fourier spectra, the peak's amplitudes are attenuated where the soil liquefies. The reason for the attenuation can be found in the high value reached by the Damping ratio of the soil during the motion (>20%) due to the increase of the shear strains.

The *Fourier Amplification function* (*FAF*) is calculated by means of the ratio (point by point) of the Fourier Spectra calculated near the ground surface and the one calculated at the bottom. The two *FAF* are shown in Figure 5.3, superimposed in order to better show the difference between them.

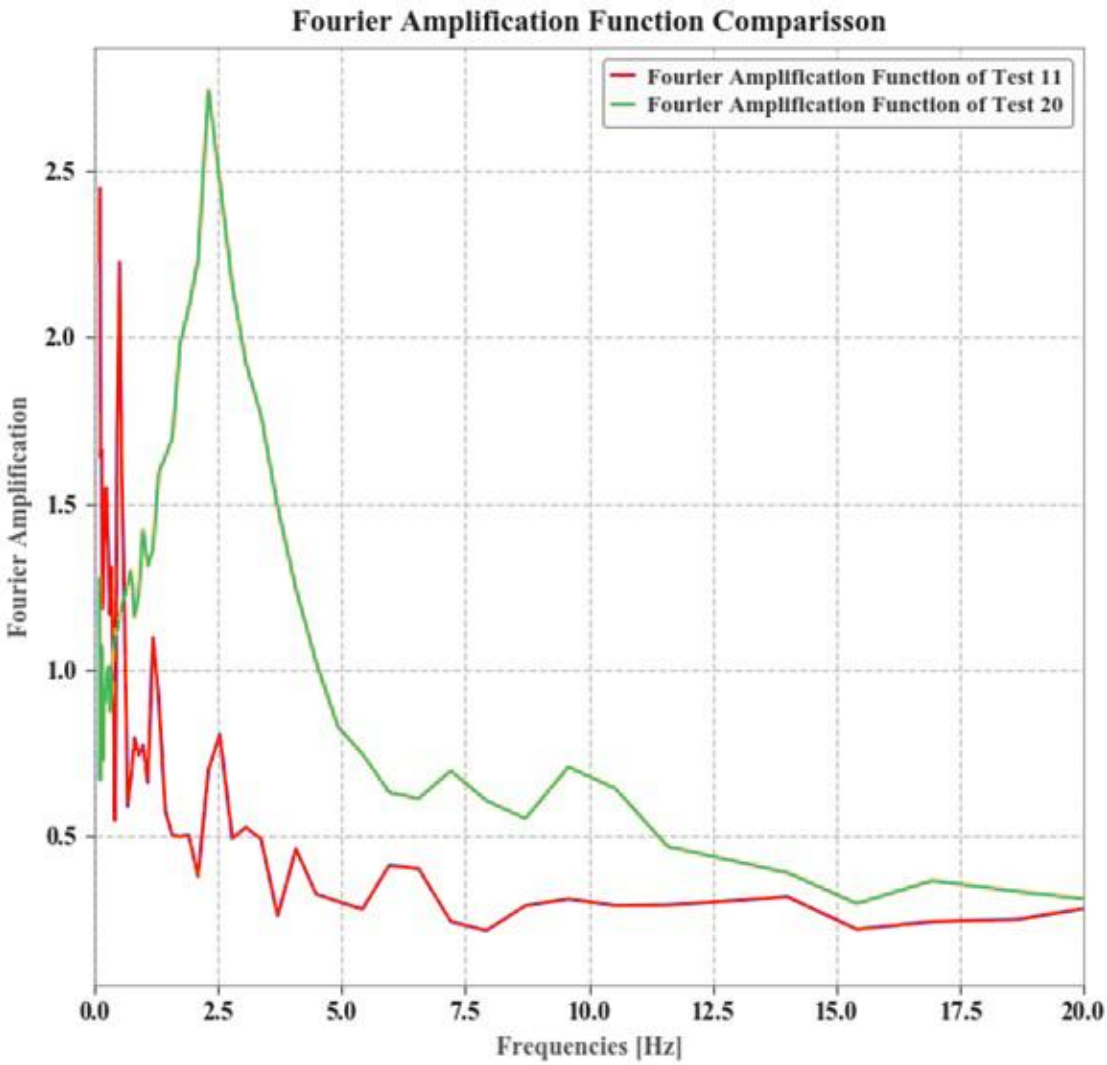

Figure 5.3- Representation and comparison of the two FAF

The behaviour described in section 2.5.4 was expected: the amplitude of the FAF is modified as well as the frequency content. Particularly, observing the FAF of the soil that developed high ru values, the peaks are translated towards lower values of frequency and, at the same time, the amplitude of the peaks is affected by an attenuation. As it has been previously described, this behaviour is produced by the simultaneously decrease of the shear modulus G and increase of the damping ratio D which develops during the cyclic shearing and, particularly, it is more pronounced if the soil is affected by liquefaction.

5.2.2 *Stockwell transform*

The Fourier amplification function analysed in 5.2.1 is not completely suitable for the analysis of non-stationary systems, such as the seismic motions. In fact, Fourier amplification function is based on the hypothesis that a single harmonic wave is characterized by constant amplitude, phase and frequency. All these reasons lead to look for an alternative shaking parameter, which is more suitable for the analysis of a seismic signal, i.e. the Stockwell transform or "S-transform". Such transformation function provides the local spectrum of a signal and is also consistent for a non-stationary system, allowing to evaluate the dynamic behaviour of a system in the time-frequency domain, which is not provided by the Fourier spectrum.

For these reasons, the S-transform functions are more effective to describe how liquefaction modifies the appearance of the ground motion. As mentioned on the Chapter 2, Section 2.5.4, when liquefaction occurs, the appearance of the time series changes dramatically. Particularly, as soon as the soil liquefies, the transfer function of the deposit makes all the high frequency components null and then, after the triggering of liquefaction, the motion contains only low frequency components (of reduced amplitude).

The change of the input motion passing through a liquefied soil is shown by means of the double comparison of two shaking parameters (i.e. acceleration series and S-transform) measured at the bottom of the model (input) and the same parameters measured near the surface of the model (output). As in the chapter 5.2.1, the selected tests analysed are Test 11 and Test 20.

In Test 11, as soon as it reaches a high level of r_u, i.e. at t=16s, the acceleration series (Image 4a) undergoes a dramatic de-amplification: the peaks are suddenly cut down, thus, the ground motion gets smoother. This change in shape can be better seen in the S-transform (Image 5.4b) registered near the surface: while the first part of the function (10-16s) contains high frequency peaks (presence of light blue shades at high frequencies), after it reaches a high level of r_u, all the high frequencies disappear (absence of light blue shades at high frequencies), and the motion contains only low frequency components. The S-transform calculated on the bottom is also shown (Image 5.4c) to prove that the original ground motion contained high frequency components for its whole duration, i.e. until t=43s.

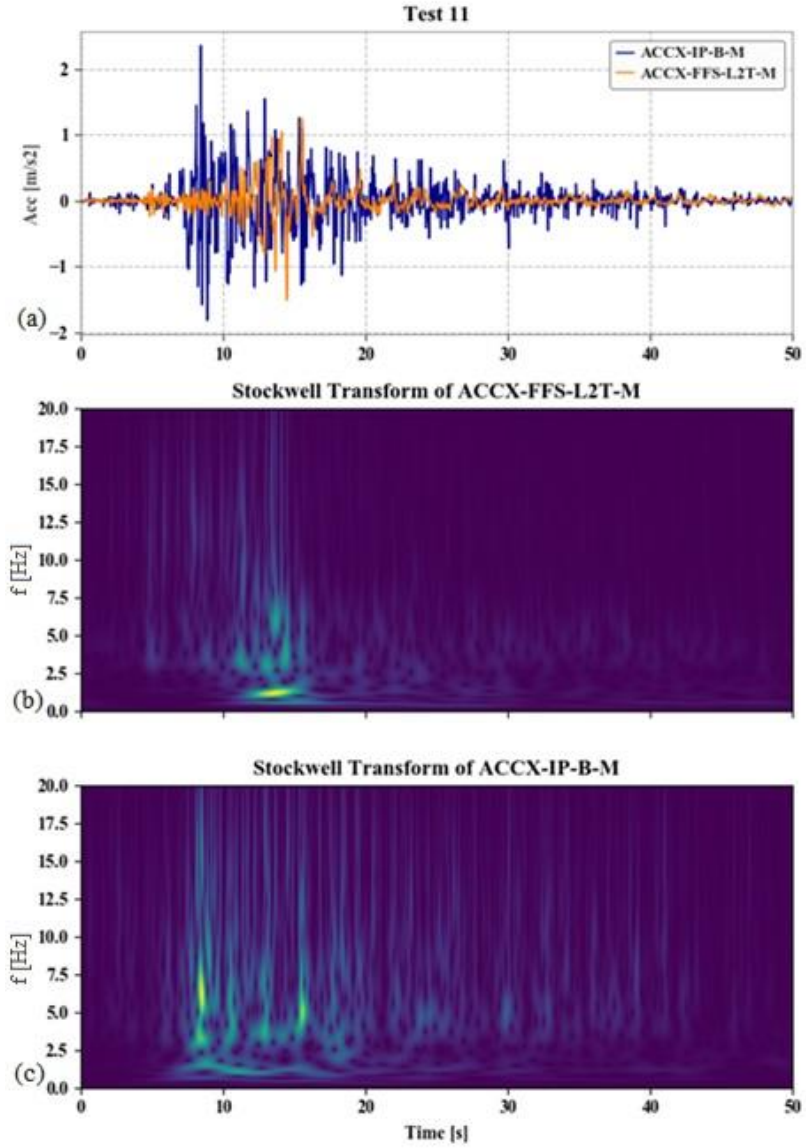

Figure 5.4- Influence of pore pressure increase on surface acceleration

Additionally, the same analysis is carried out for a test in which the increase of pore pressure is prevented by mitigation measures (Test 20). The original aspect of the Stockwell function, i.e. the one calculated on the bottom of the model, is shown in Figure 5.5c. As it is expected, the acceleration series (Figure 5.5a) near the surface does not undergo any sudden change and the frequency content of the motion is not modified by the soil; thus, high frequency components are still present in the S-transform calculated near the surface (Figure 5.5b).

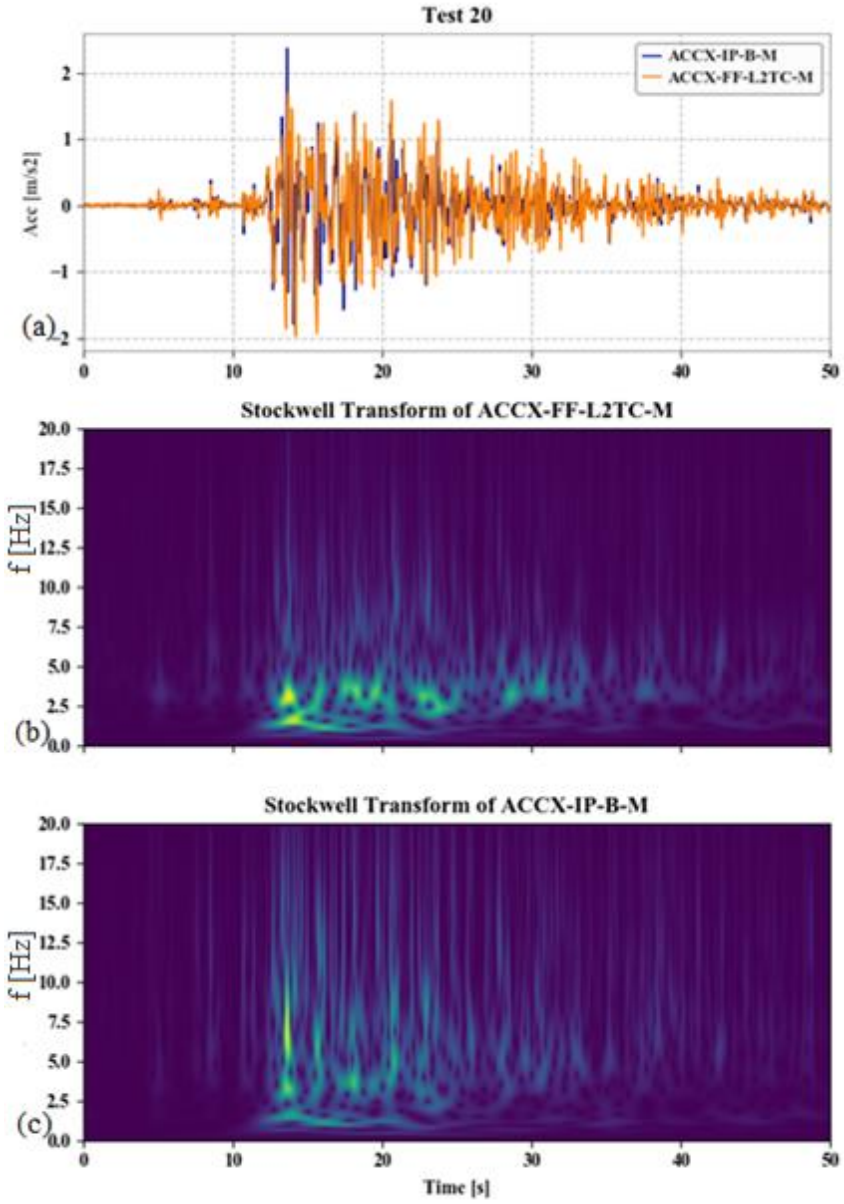

Figure 5.5- Effectiveness of vertical drains on pore pressure increase prevention

5.3 Pore pressure analysis

5.3.1 Hydrostatic distribution

Six tests representative of model 1-b and model 2 (all in free-field condition, 1 without mitigation techniques, 1 with drains and 1 with IPS, for each model) were analysed, being that the Test 11, whose model is shown in Figure 5.6, as the most representative results obtained.

On Figure 5.7, the initial values of the pore pressure time series are represented for the depth of the model, and a tendency line then links the points. As described in the following, the

prototype pore pressure distribution is mainly following a hydrostatic distribution, except for a small difference. In fact, the prototype pore pressure distribution is, in all the cases, smaller than the theoretical one. The reason of this behaviour can be found on the fact that the centrifuge acceleration of $50g$ is referred to the bottom of the box, where the centrifuge radius is maximum (R=2172mm). On the other hand, on the rest of the box, as the centrifuge radius is smaller, the N is also smaller (eq. 44) and the value of pore pressure will be lower.

As an example, the ideal value of pore pressure is calculated considering the variation of the centrifuge acceleration along the model, due to the variation of the centrifuge radius. Table 3.3 presents the values obtained in each transducer and the calculated theoretical hydrostatic pressure (constant and radius dependant), except ppt2 due to an error in the transducers data acquisition.

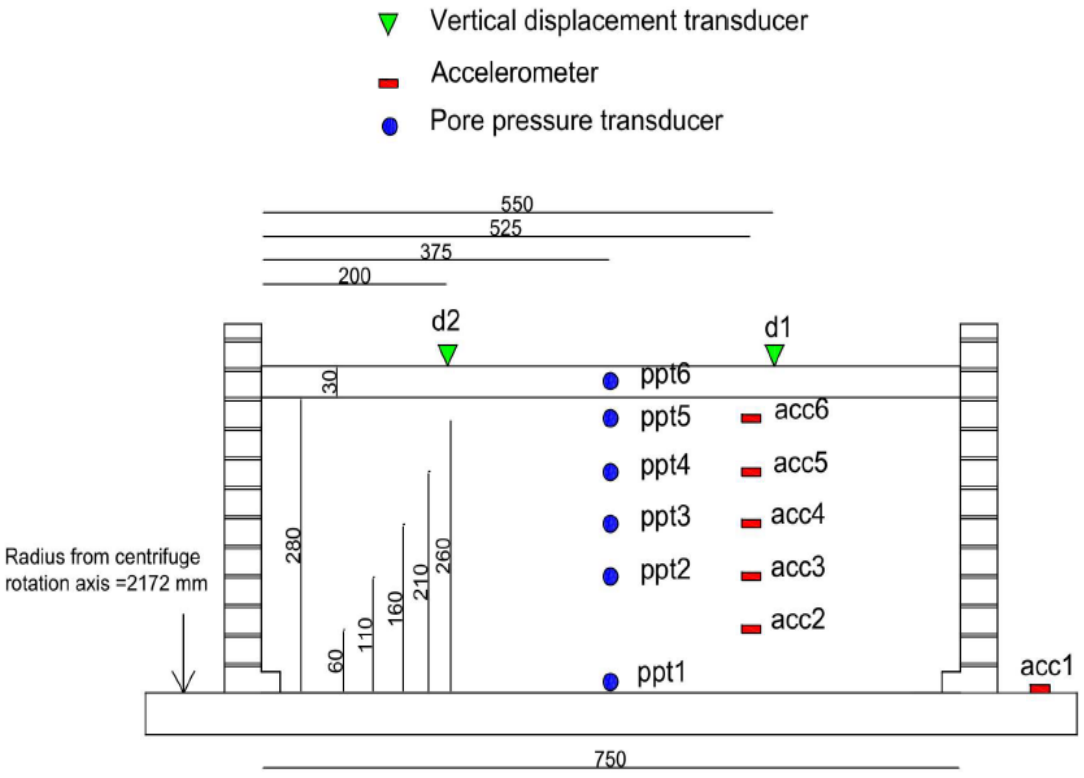

Figure 5.6- Profile of test 11

Table 5.3- Prototype and Hydrostatic pore pressure values for test 11 transducers

Transducer	Prototype depth (m)	Prototype pore pressure (kPa)	Theoretical pore pressure (kPa)	Centrifuge radius (m)	Angular velocity (rad/s)	N (g)	Theoretical pore pressure radius dependant (kPa)
ppt1	15.50	124.6	155	2.17	15.08	50	156
ppt2	10.00	(-)	100	2.07	15.08	48	95.7
ppt3	7.50	49.8	75	2.02	15.08	47	70.1
ppt4	5.00	42.7	50	1.97	15.08	46	45.6
ppt5	2.50	19.2	25	1.92	15.08	44	22.2
ppt6	0.75	1.2	7.5	1.89	15.08	44	6.5

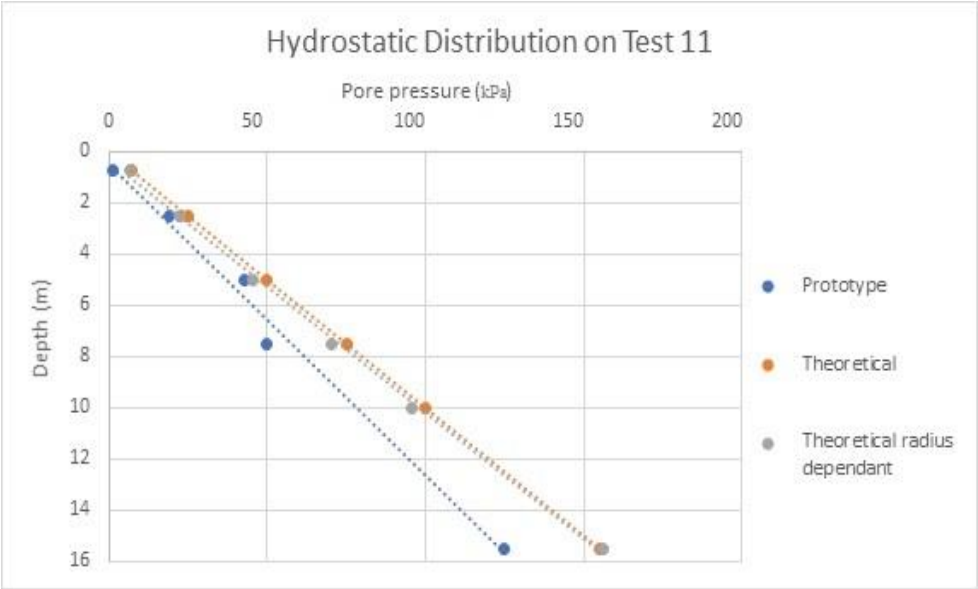

Figure 5.7- Graph of the hydrostatic pore pressure distribution for both the prototype and the theoretical model

Finally, a significant difference (83%) is met in the first clayey layer, this difference is probably due the fact that the soil layer is not completely saturated.

5.3.2 Pore pressure build-up

Another comparison is made in terms of the excess of pore pressure. Particularly, the pore pressure build-up is analysed in terms of the pore pressure ratio obtained by the pore pressure in the transducer closer to the ground surface (at the "top centre of the first layer" PPT-FF-

L1TC-M), since the highest value of r_u presented in the model is in that position for most tests (sometimes there is no “top-centre” transducer).

In this analysis, three tests were examined, all concerning the free-field analyses in model 1-b: one without any mitigation technique (Test 3), one with a dense arrangement of horizontal drains (Test 18) and one with four injectors of IPS (Test 30).

Concerning Test 3 (Figure 5.8) and Test 18 (Figure 5.9), it is possible to observe that the presence of the horizontal drains has a double effect on the model. The main one concerns the halving of the pore pressure amplitude peak measured by the transducers, which turns from a value really close to 1, on Test 3, to a value of 0.48, in Test 18. Additionally, a more rapid decrease of the pore pressure peak values along a vertical axis in the box is generated by the presence of the dense arrangement in the drains.

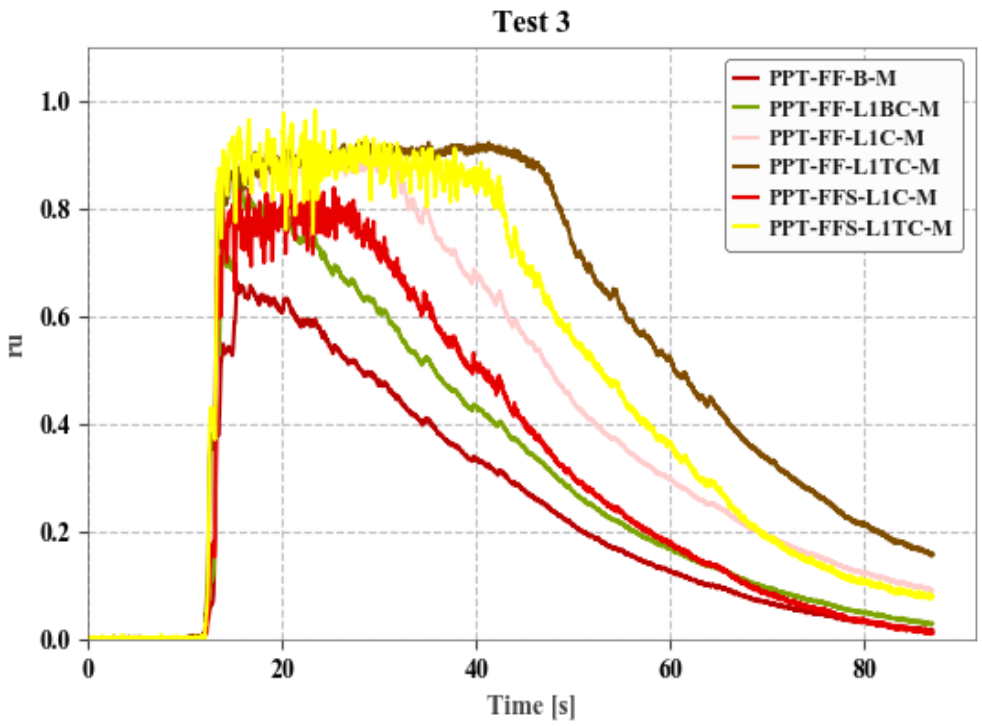

Figure 5.8- Ru values through time for test 3

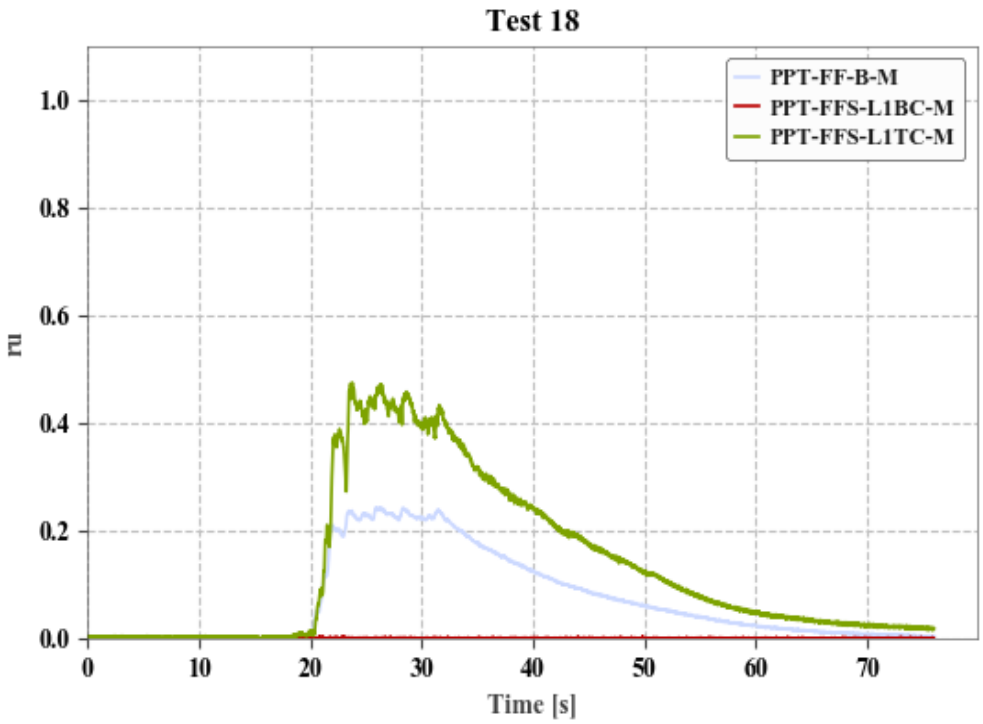

Figure 5.9- Ru values through time for test18

In order to show the effect of the IPS on the pore pressure build-up, the Test 30 (Figure 5.10), where 4 air bubbles injection are used, is analysed. As expected, in the depths from the bottom to the centre of the model there is a noticeable reduction of the pore pressure ratio. On Test 3, it was ranging from 0.6 to 0.8 and, on Test 30, the mitigation technique reduced from 0.2 to 0.4. Although the improvement is significant at higher depths, it is believed that the air injection isn't enough to reach the "top-centre" part of the model, where the maximum values of pore pressure ratio are reached (ru = 1) on both tests.

In conclusion, although IPS is effective in most of the model, it still leaves the top-most part of the model in liquefiable condition, so it could be interesting to evaluate the effect of several injectors, not only spread in the bottom of the model but also closer to the top-centre area, where liquefaction happens.

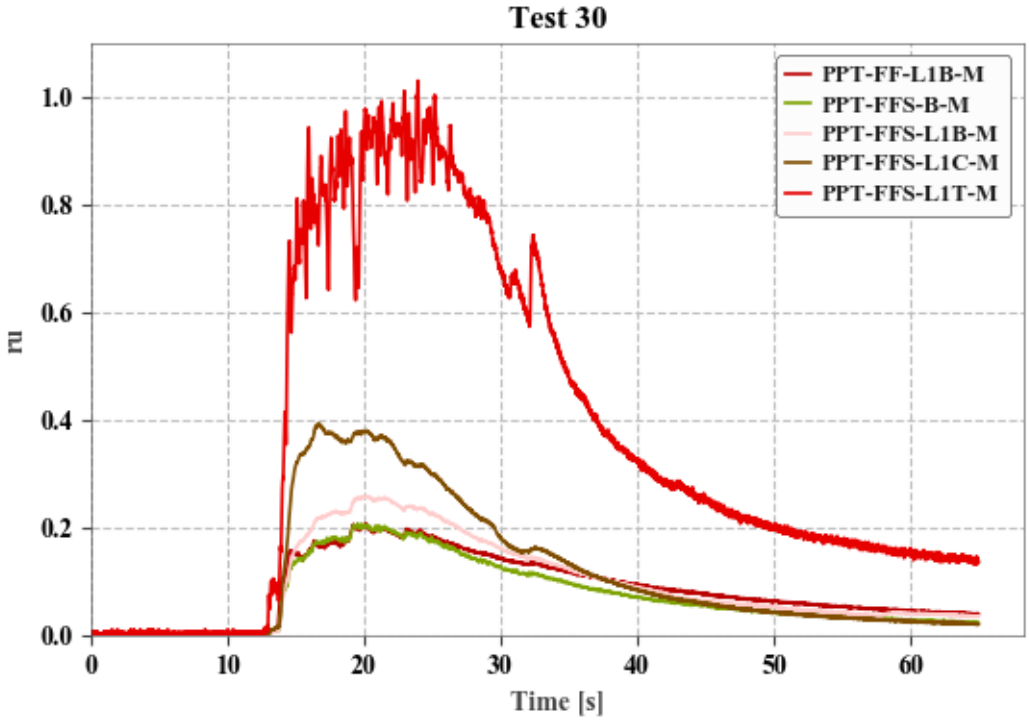

Figure 5.10- Ru values through time for test 30

The maximum values of the r_u for the 21 tests, for both the free-field condition (Table 5.4) and the building condition (Table 5.5) are shown below.

Table 5.4- Ru values corresponding to the treated tests in free-field condition

Free-Field Analyses							
Models	No Mitigaton Techniques	Mitigation Techniques					
		Drains				IPS	
		V1	V2	H1	H2	IPS1	IPS4
Model 1 - b	0.98	0.61	0.75	0.48	0.48	0.52	1
Model 2	0.86	0.27	0.48	0.21	0.25	1	0.66

Table 5.5- Ru values corresponding to the treated tests in building condition

Building Analyses				
Models	No Mitigaton Techniques	Mitigation Techniques		
		Drains		IPS
		V1	H1	IPS1
Model 1 - b	0.99	1	1	0.73
Model 2	0.98	0.77	1	-

5.3.3 Seepage analysis

A seepage analysis is carried on the test 3 in order to better understand why liquefaction develops always around the transducer located in the top-centre part of the model.

Initially, a graphic representation of the pore pressure builds up on the test 3 is provided again. In Figure 5.11, unlike Figure 5.8, only the curves of the 4 transducers placed along a vertical axis are shown, as they are the only ones analysed for the seepage. As mentioned above, the highest r_u is obtained in the closest pore pressure transducer closer to the surface (PPT-FF-L1TC-M).

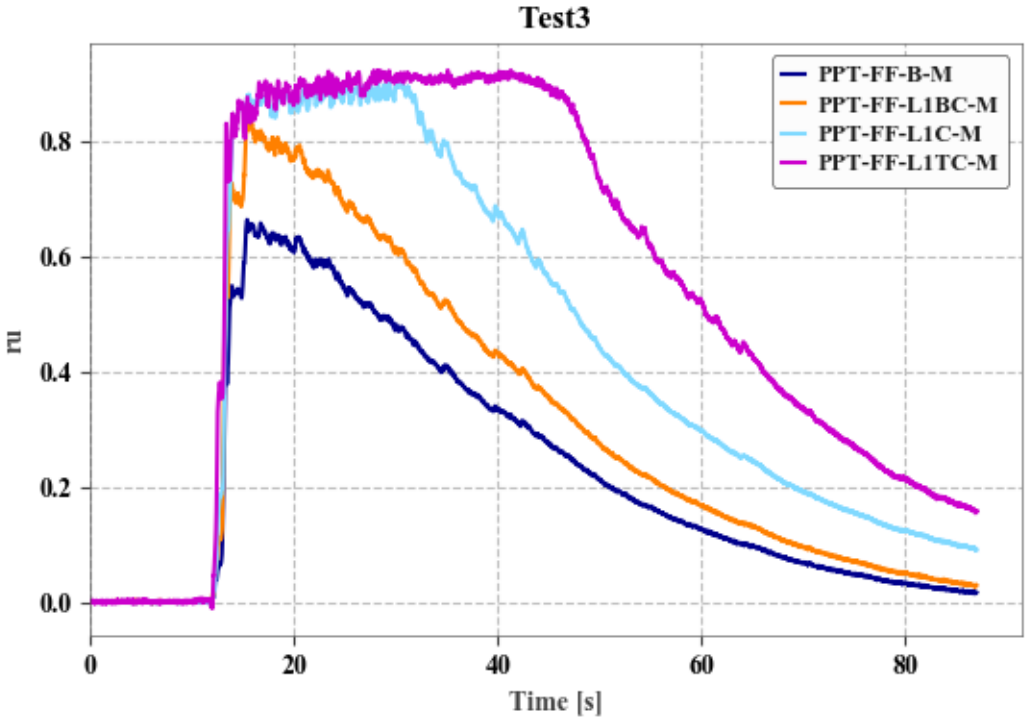

Figure 5.11- Ru build-up through time on the different transducers

In Figure 5.12, the increase of excess pore pressure along the depth is shown. The different curves represent the Δu profiles at different time frames, where:

- 12 s represents the hydrostatic condition before the ground motion;
- 13-17 s correspond to the timeframe from the first peak of the acceleration series, correspondent to the initial part of the pore pressure build-up, until it reaches its maximum value of pore pressure build-up;
- 25 s represents an initial decrease of the pore pressure build-up with depth as the ground motion's intensity is halved;
- 45 s corresponds to the end of the ground motion.

These observations are coupled with Figure 5.13 where the input ground motion of Test 3 is shown.

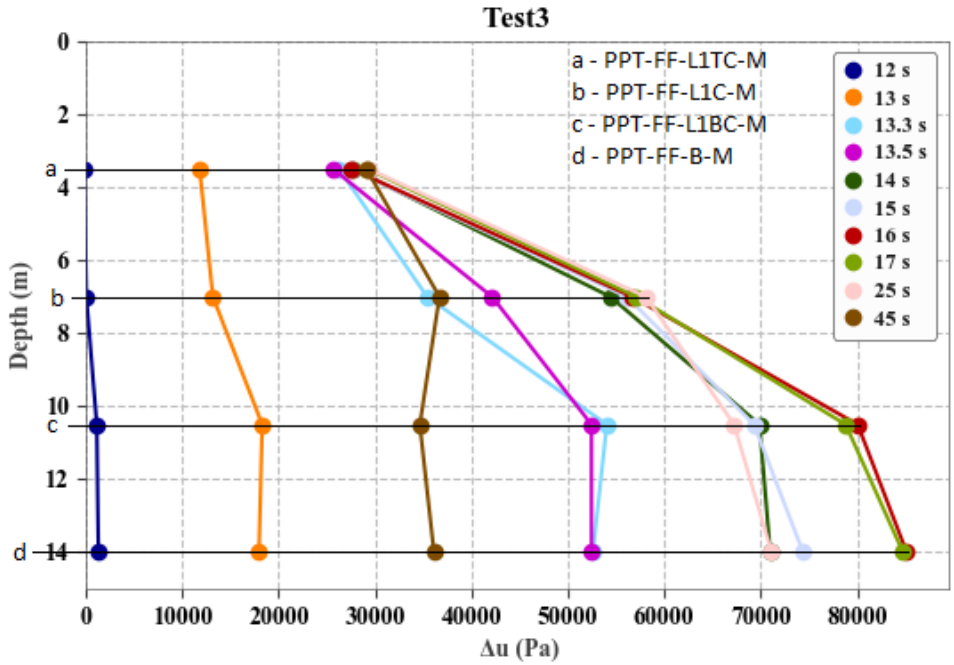

Figure 5.12- Excess pore pressure with depth evaluated at different time instants

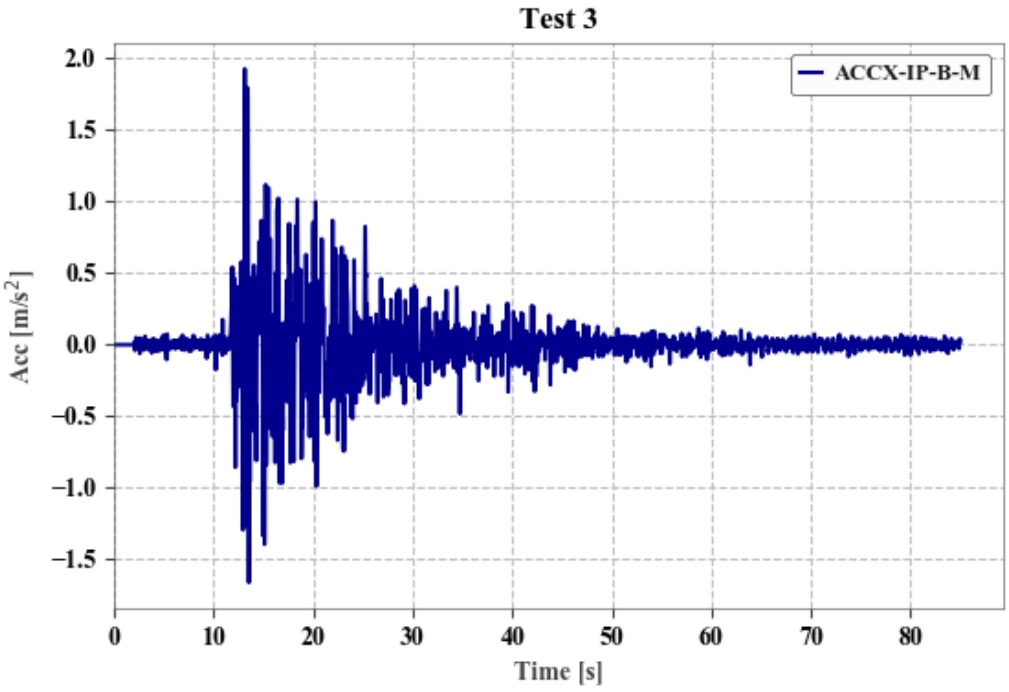

Figure 5.13- Input ground motion of Test 3

An increase of Δu build-up with the depth can be observed. The rate of pore pressure increase with depth is more significant on the upper part of the box and less pronounced on the bottom part. This trend of Δu can be justified by a seepage which goes from the bottom of the site toward the ground surface. The water flow can be analytically explained by the hydraulic gradient, calculated between two different points on the box. This analysis will be carried out between the point (a) (close to the surface) and (d) at time t=16s, as it is a representative time of the water behaviour along the whole box during the triggering of liquefaction. As it is showed in the following the hydraulic gradient is positive, i.e. the hydraulic head is highest on the bottom part and the water flows toward the surface:

$$i = \frac{\Delta h}{l} > 0 \tag{51}$$

Where Δh is the difference in hydraulic head and l is the distance between the two pore pressure transducers; since l is a distance, the equation can also be written as:

$$\Delta h > 0$$

$$\frac{u_d - u_a}{\gamma_w} + z_d - z_a > 0$$

$$\frac{u_d - u_a}{\gamma_w} > z_a - z_d$$

where u_a and u_d are the value of pore pressure registered by the pore pressure transducers on the points "a" and "d" at the time t=16s, while z_a and z_d are the respective distance of the transducers from the bottom of the box. So, an upward flow will be installed if the difference in piezometric heights, $\frac{\Delta u}{\gamma_w}$, is higher that the difference between the geometric heights. Finally, the actual numbers obtained from the numerical analysis are then replaced in the previous formula:

$$\frac{(185.62 - 47.48)\ kPa}{9.81\ \frac{kN}{m^3}} > (11.5 - 0)m$$

$$14.06m > 11.50m$$

In Figure 5.14, the r_u with depth for different time instants is shown.

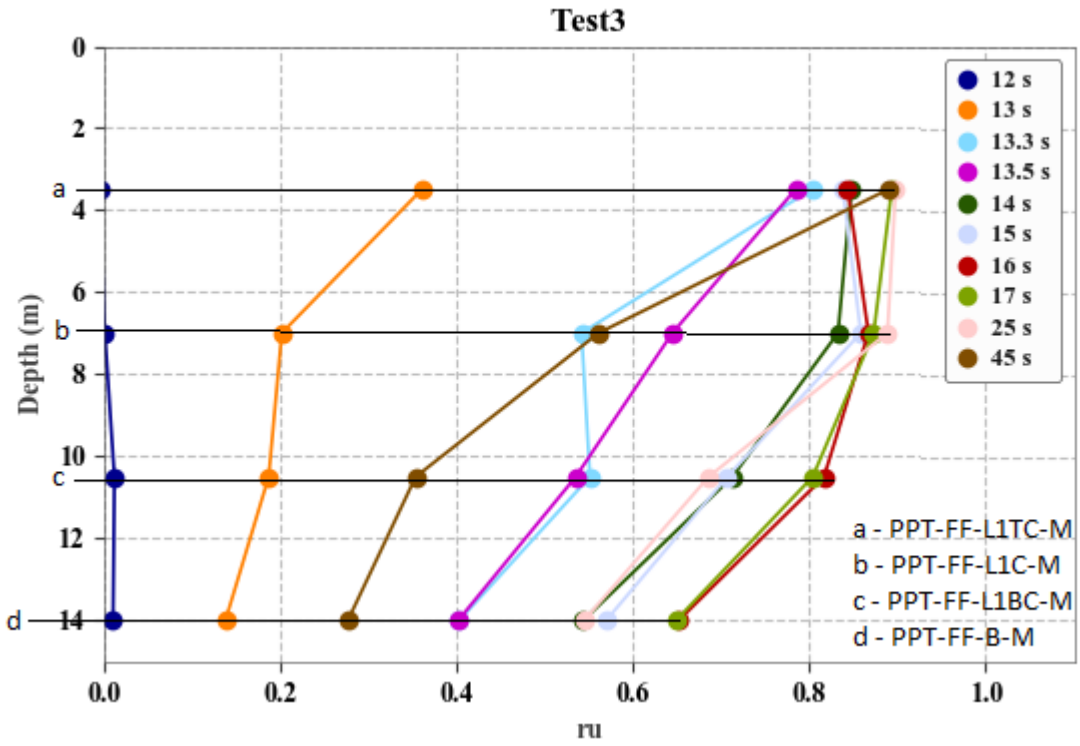

Figure 5.14- Ru with depth for different time instants

The most relevant feature in this graph is given by the fact that, after the end of the motion (t=45s), while the r_u is decreasing on the middle-bottom of the box, the surface layer stays with high ru values for a larger period of time. This behaviour could be explained by:

- the upward seepage previously described;
- the total reflection of the seismic waves close to the surface, which increase the duration of energy input on the superficial layer.

It is also important to highlight the difference between the trend of the curves of Figures 5.12 and 5.13, respectively for the excess pore pressure build-up and the pore pressure ratio. This difference can be explained by a smaller increase of excess pore pressure with depth in comparison to the increase of the effective stress with depth.

5.4 Model settlements

The different model behaviours in terms of settlements are shown in the following. The tests shown in Figure 5.15 (Test 3) and Figure 5.16 (Test 18) are characterized by a homogeneous layer of Ticino Sand of 14 m at the prototype scale; the applied ground motion is also the same in the two tests, i.e. GM31. The only relevant difference is given by the presence of a dense arrangement of horizontal drains in the Test 18.

In Test 3 a significant differential settlement (10 cm) can be noticed: this behaviour could be due liquefaction occurring only in certain parts of the soil, i.e. the presence of the heterogenous areas into the model.

In Test 18, there is a significant decrease in the model settlement, which reaches values such as one third of the settlement occurred in absence of mitigation measures.

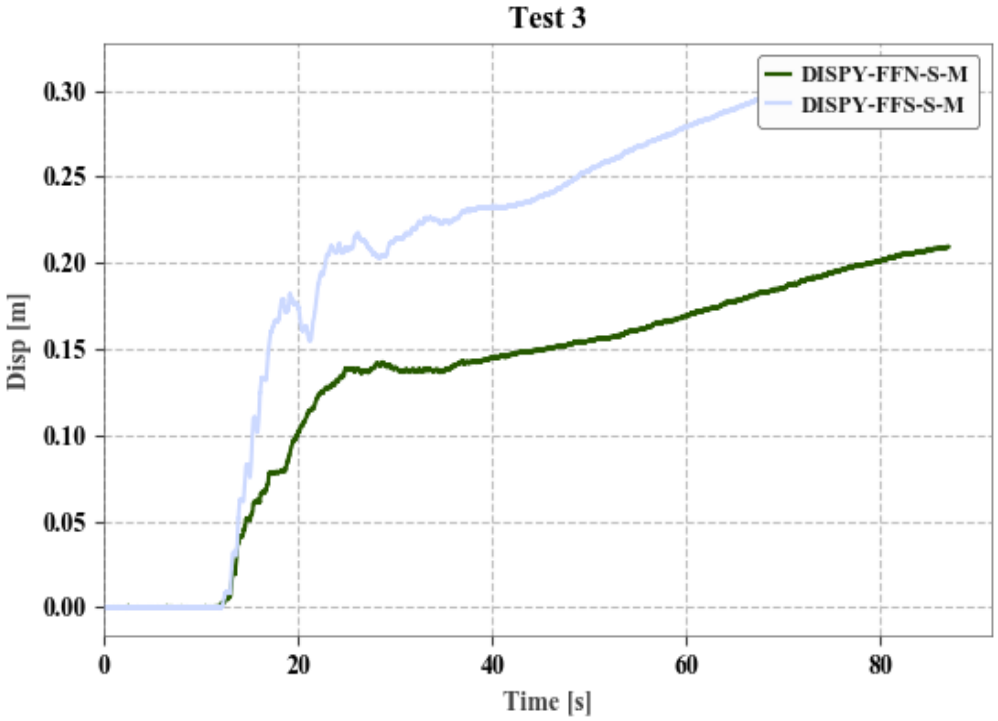

Figure 5.15- Ru with depth for different time instants

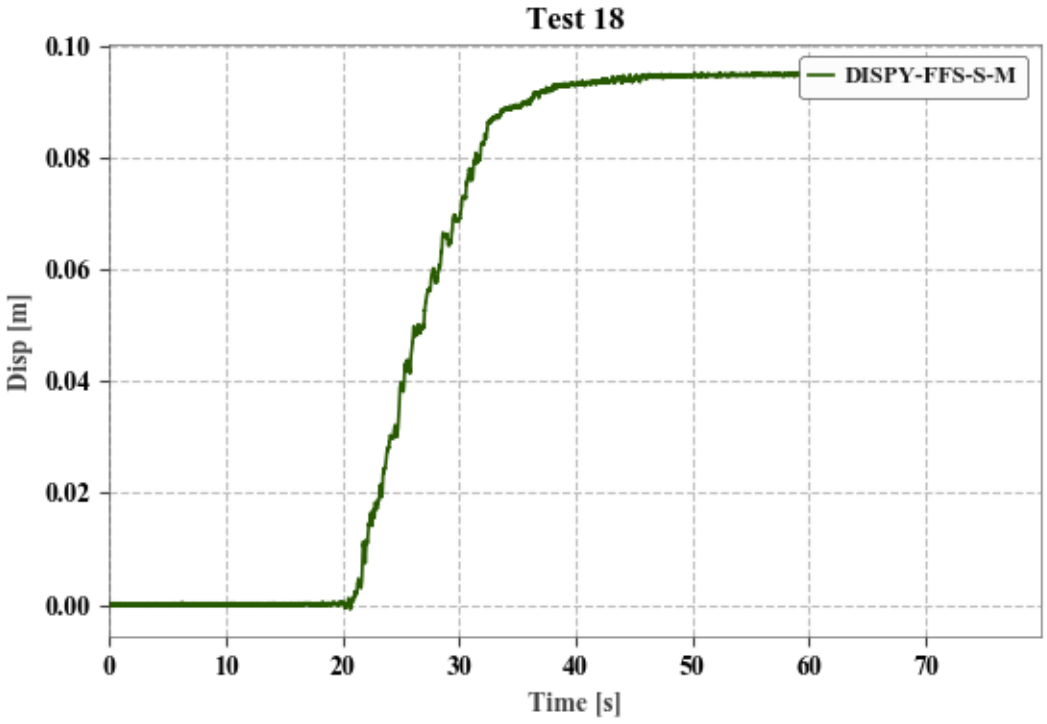

Figure 5.16- Displacement values through time for Test 18

The effectiveness of the Induced Partial Saturation is showed in Figure 5.17 (Test 30). In that model, a 14 m sandy layer is characterized by 4 air bubbles injection. The settlement reduction in the model is significant and nearly as effective as the introduction of horizontal drains.

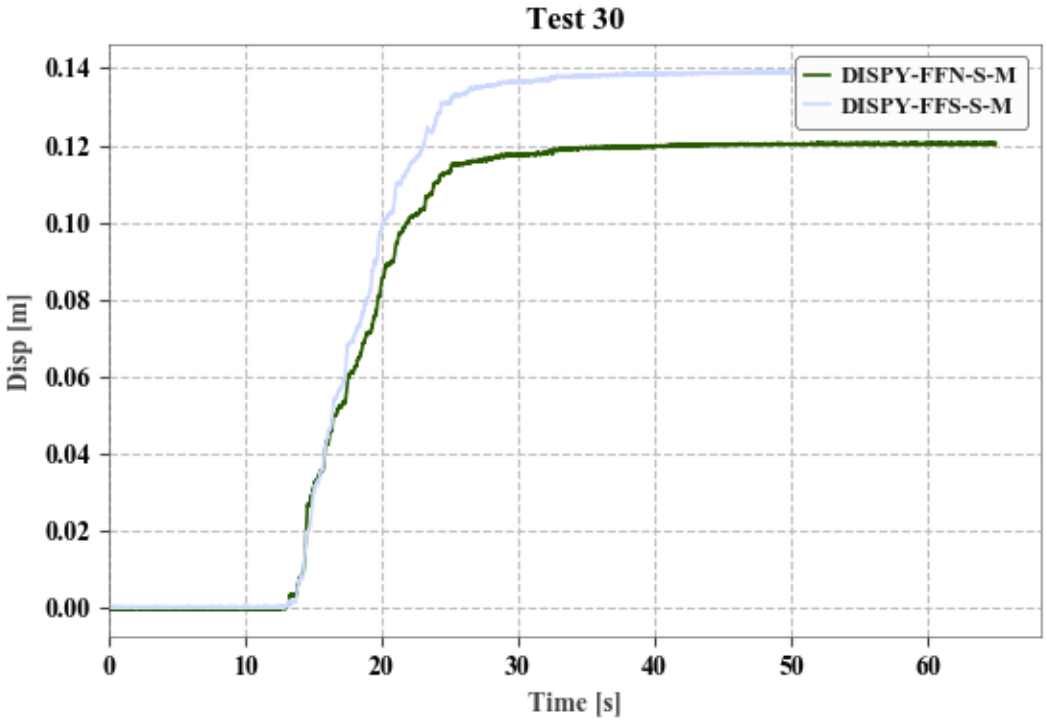

Figure 5.17- Displacement values through time for Test 30

The maximum values of the displacements for the 21 tests, for both the free-field condition (Table 5.6) and the building condition (Table 5.7) are shown below.

Table 5.6- Displacement values corresponding to the treated tests in free-field condition

Free-Field Analyses							
Models	No Mitigation Techniques	Mitigation Techniques					
		Drains				IPS	
		V1	V2	H1	H2	IPS1	IPS4
Model 1 -b	0.31	0.43	0.25	0.1	0.13	0.33	0.14
Model 2	0.27	0.03	0.05	0.03	0.03	0.15	0.04

Table 5.7- Displacement values corresponding to the treated tests in building condition

Building Analyses				
Models	No Mitigation Techniques	Mitigation Techniques		
		Drains		IPS
		V1	H1	IPS1
Model 1 -b	0.85	0.6	0.44	0.09
Model 2	0.31	0.27	0.24	-

6. COMPARISON OF THE CENTRIFUGE DATA WITH SIMPLIFIED METHODS TO ESTIMATE PORE PRESSURE BUILD UP

6.1 Introduction

In chapter 5 it was needed to select 21 out of the 37 tests, for consistency purposes in the analyses between several tests. However, in chapter 5, all the 37 tests are treated; in fact, the main goal is to analyse the accuracy of the Seed et al. (1985) Stress-Based Method (SBM) and Strain Energy Based Method (SEBM) proposed by Millen et al. (2019) both described in chapter 3 section 3.2 by comparing it to the centrifuge model results.

The SBM and the SEBM are simplified methods to evaluate the pore pressure build-up in free field. Unfortunately, a large number of sensors are not in free field and, thus, these sensors were taken out of the analysis. In addition, these methods were developed to estimate pore pressure build up in the middle of the liquefied layer, being less accurate near the surface or close to the bottom of the model. Particularly, the data excluded from the analysis are the ones obtained from:

- Sensors placed at the bottom of the model
- Sensors placed on the clayey layer
- Sensors placed under the building or near mitigation measures
- Sensors placed at a depth correspondent to $\sigma_v' < 15\ kPa$
- Sensors registering a ru_{max}<0.2
- Sensors with a null output

The calculation of the behaviour predicted by the SBM and the SEBM is performed taking as reference the centrifuge reduced model (CRM) results.

6.2Strain energy-based method

In this section, the validation of the Strain-energy-based method implemented by Millen et al. (2019) is performed. Initially, the r_u build up predicted by Millen et al. (2019) in equation 43 is analysed. Where:

- $r_{u,liq}$ is defined as (equation 51):

$$r_{u,liq} = \frac{\sigma'_{v.i} - \sigma'_{v,liq}}{\sigma'_{v,i}} \quad (51)$$

being $\sigma'_{v,i}$ the initial vertical stress and $\sigma'_{v,liq}$ the vertical stress reached during the test at which liquefaction is predicted, fixed at 5 kPa.

- $NCASE_{liq}$ is calculated from the closed form equation 44, where the values S_r and κ (which is the value of the integral) were respectively assumed equal to 40 (Millen et al., 2019) and 1 (Kramer et al., 2016); the CSR values for Ticino and Pieve di Cento sands were obtained from tests carried out on the same sand by Mele et al. (2019). Since the CSR value changes with density, the CSR_{15} value taken for each soil is the average for the range of relative densities used in the centrifuge tests (Table 1). As the data for Clean Pieve di Cento sand was not available, its CSR was considered equal to the one of Natural Pieve di Cento Sand.

Table 6.1- CSR values

	D_R	CSR
Ticino Sand	40-57%	0.24
Natural Pieve di Cento Sand	46-70%	0.14
Clean Pieve di Cento Sand	46-70%	0.14

- $NCASE_i$ is calculated for each cycle from equation 45. It is increasing cycle by cycle due to the decrease of the Shear Modulus during shearing and also due to the accumulation of strain energy in each cycle.

In order to better estimate the error included in the closed form relationship, a non-linear calibration of the value $NCASE_{liq}$ was performed. For this purpose, the $r_{u,max}$ present in equation 43 was replaced by the $r_{u,max}$ obtained in the centrifuge test results so that $NCASE_{liq,i}$ is determined for each test (equations 53, 54):

$$r_{u,max.centrifuge,i} = \sqrt{\frac{NCASE_{max,i}}{NCASE_{liq,i}}} \cdot r_{u,liq,i} \quad (53)$$

$$NCASE_{liq,i} = NCASE_{max,i} \cdot \left(\frac{r_{u,liq,i}}{r_{u,max.centrifuge,i}}\right)^2 \quad (54)$$

Once the calibrated $NCASE_{liq,i}$ is obtained, the average value between all the tests of a specific sand ($NCASE_{liq,average}$) is calculated for n tests in equation 55:

$$NCASE_{liq,average} = \frac{\sum_{i=0}^{n} NCASE_{liq,i}}{n} \tag{55}$$

Finally, $NCASE_{liq,average}$ is used in equation 55 and the calibrated non-linear results are obtained (equation 56:

$$r_{u,predict,i} = \sqrt{\frac{NCASE_{max,i}}{NCASE_{liq,average}}} \cdot r_{u,liq,i} \tag{56}$$

The mentioned equation (41) proposes a square root relationship. However, when plotting the r_u versus the NCASE/$NCASE_{liq}$ of the centrifuge data it seems that the relationship is not always of that type. In fact, in some cases, it seems closer to a linear relationship (Figure 6.1). So, the same calibration was performed again using a linear form of the equation (41), between r_u and $\frac{NCASE}{NCASE_{liq}}$, resulting in the $NCASE_{liq}$ given by a linear form (equation 57)

$$NCASE_{liq,i} = NCASE_i \cdot \frac{r_{u,liq,i}}{r_{u,max.centrifuge,i}} \tag{57}$$

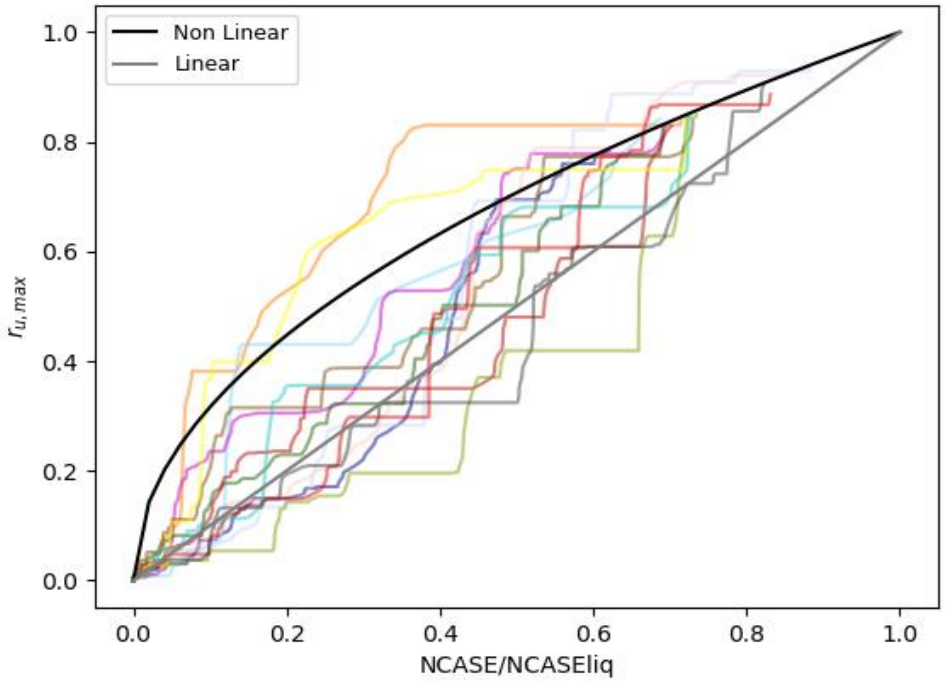

Figure 6.1- Centrifuge data plotted in a graph with NCASE/$NCASE_{liq}$ in abscissas and $r_{u,max}$ in ordinates

6.2.1 Validation of the model

The comparison between the pore pressure build-up calculated by the three different implementations of the SEBM and the one obtained by the centrifuge test results is shown in Figure 6.2. The only difference between these three implementations is the $NCASE_{liq}$ value: in the SEBM closed form this value is calculated by equation (40), in the SEBM non-linear this value is the calibrated $NCASE_{liq}$ obtained with the square root relationship, in the SEBM linear the value is the calibrated $NCASE_{liq}$ obtained with the linear relationship. Test 1 was selected as representative since it is performed in free-field condition. In this case, the implementation that best fits the centrifuge results is the linear calibration, however, as will be subsequently shown, the best fitting method changes from case to case.

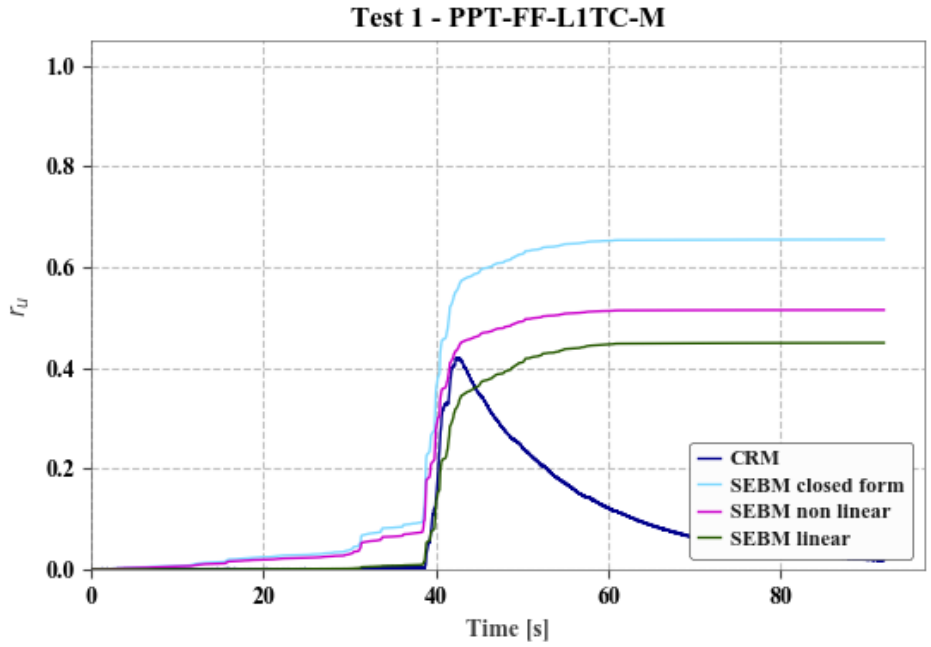

Figure 6.2- Comparison between ru build-up of the three SEBM predictions and the centrifuge results.

It should be noted that the methods do not account for the seepage and so, after the centrifuge results reach their peak, the models have unrealistic values. Nevertheless, it does not affect the analyses as the main parameters (t_{liq} and r_u) will be determined before and at the centrifuge peak, as will be explained next.

Once the behaviour of the selected transducers was evaluated for each test, each r_u prediction was compared to the one obtained from the centrifuge tests. For this purpose, a clear distinction

was carried out: tests where liquefaction happened were separately studied from the ones unaffected by the phenomenon.

6.2.1.1 Test-cases affected by liquefaction

The test cases affected by liquefaction are the ones where the maximum of r_u obtained in the centrifuge data is higher than $r_{u,liq}$ determined according to equation (51). For each transducer that register $r_u > r_{u,liq}$, t_{liq} was compared in both the predicted method and the actual centrifuge results. The mentioned time t_{liq} was considered a measure of the accuracy of the prediction. Thus, a graphical representation of the discrepancy between t_{liq} obtained, predicted by the mentioned methods and the one obtained from the centrifuge results is shown in Figure 6.3.

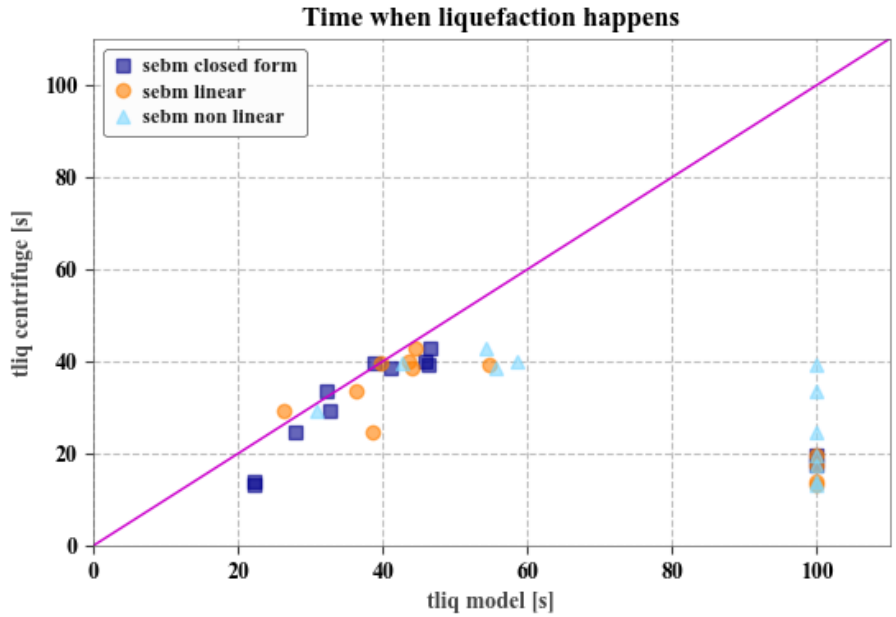

Figure 6.3- Comparison between predicted tliq by the three SEBM curves and centrifuge test results

The t_{liq} estimated by the closed-form is rather accurate when compared to the centrifuge one, i.e., the model predicted the liquefaction triggering almost at the same time. Comparing the calibrated values, the results obtained from the linear calibration are better than the non-linear, although they are still worse than the closed form. As it is obvious, if the calibrated

$NCASE_{liq}$ for each case was taken (instead of the average for each soil), a perfect match would have been obtained, and therefore 100% correct estimations.

Additionally, in table 6.2, two statistical parameters are shown: the first one is the averaged error ($\overline{\chi}$) of the t_{liq} parameter, with the error (χ) determined as indicated in equation 58; the second is the percentage of correct estimations (CE), determined by the ratio between the number of results with an error lower than 20% and the total number of results, as indicated in equation 59. It should be noted that, given these statistical parameters, the best prediction would be the one with the lowest ($\overline{\chi}$) and highest (CE).

$$\chi(\%) = \frac{t_{liq,pred} - t_{liq,centrif}}{t_{liq,centif}} . 100 \quad (58)$$

$$CE(\%) = \frac{n_{\chi<20\%}}{n} . 100 \quad (59)$$

Table 6.2- Statistical results of the tliq in the three SEBM predictions

	T_{liq} SEBM		
	Closed-form	Non-linear	Linear
$\overline{\chi}$(%)	71	210	152
CE (%)	66	17	50

A huge value in the average error of the t_{liq} results can be noticed in the calibrations: the reason of this misbehaviour can be found in the underprediction of the t_{liq} values by the SEBM in some tests affected by liquefaction, i.e. the ones in which liquefaction occurs but it is not predicted by the model. Particularly, when the $r_{u,max}$ of the predicting model is less than the $r_{u,liq}$, the t_{liq} result of the model is the time correspondent to the maximum r_u of the SEBM, given at the last time instant. Additionally, when the t_{liq} of the SEBM is predicted as the last time instant, it is also influenced by the duration of the ground motion.

As it has been observed, this misprediction introduced some outliers on the estimation, which raised the actual value of the average error, and therefore the other parameter (CE) may be more appropriate to measure the accuracy of the method as it indicates the percentage of good predictions. Additionally, in the comparison of the t_{liq}, it is considered that the cases where this behaviour is noted should be distinguished, by showing them graphically as $t_{liq,model}$=100s,

without affecting the statistical analyses. In figure 6.4, one of transducers where the r_u value in the SEBM is underpredicted is shown, with the respective t_{liq} highlighted.

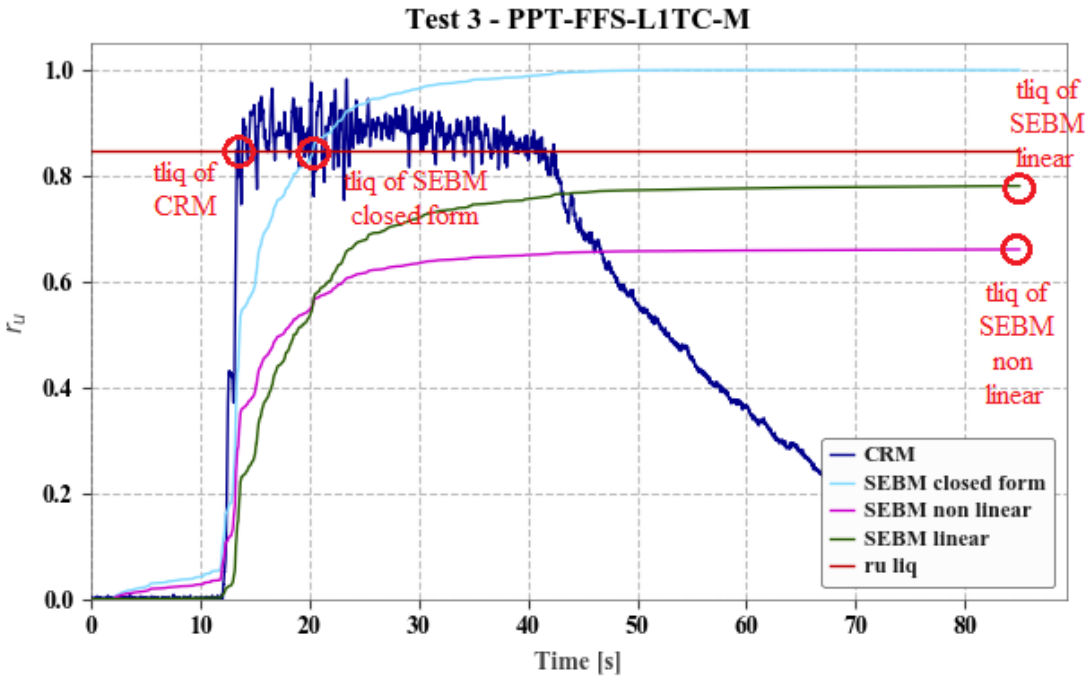

Figure 6.4- Underprediction of the SEBM leading to the tliq difference

6.2.1.2 Test-cases unaffected by liquefaction

In the transducers where liquefaction was not observed, $r_{u,max}$ was selected to estimate the accuracy of the predicting method. The $r_{u,max}$ of the centrifuge test results is obtained and compared to the r_u predicted by the SEBM for the same time. Thus, a graphical representation of the discrepancy between r_u estimated for the SEBM and the $r_{u,max}$ obtained from the centrifuge results is shown in Figure 6.5.

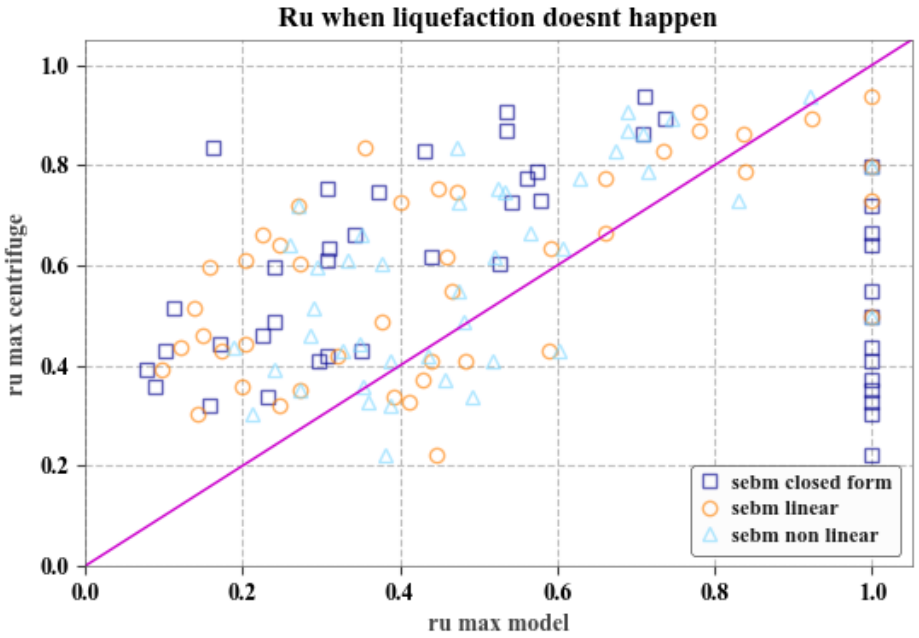

Figure 6.5- Comparison between ru predicted by the SEBM and the $ru_{,max}$ of centrifuge test results

The r_u parameter is mostly underpredicted by the closed-form (except for some cases where the model predicts full liquefaction and the centrifuge shows relatively low values). As for the non-linear and linear approaches, there are more results similar to the centrifuge, although they are still fairly scattered. In this parameter the two calibrations show an improvement in the prediction of the maximum r_u when compared to the closed form.

Additionally, in table 6.3, the two statistical parameters determined for the t_{liq} are now determined for the r_u: equation 58 turns to equation 60 while equation 7 stays the same.

$$\chi(\%) = \frac{r_{u,pred} - r_{u,max,centrif}}{r_{u,max,,centif}} . 100 \qquad (60)$$

Table 6.3- Statistical results of the ru in the three SEBM predictions

	r_u SEBM		
	Closed-form	Non-linear	Linear
$\overline{\chi}$ (%)	71	29	38
CE (%)	9	36	34

In conclusion, and with the tables 6.2 and 6.3, it can be said that the closed form is the best one for predicting t_{liq} for the cases where liquefaction occurs, whilst for the cases where liquefaction didn't happen the best case is the non-linear case. Now there are two possible findings: if the t_{liq} is considered the most relevant statistical parameter, the closed form is the best for the prediction, while if the r_u is considered the most relevant statistical parameter, it is the non-linear case. As the purpose of this work is to accurately predict when liquefaction does happen, it is safe to say that the closed form is the most suitable.

It should also be highlighted that in a real case scenario the $NCASE_{liq}$ value could be determined by laboratory tests (if available) increasing the accuracy of the prediction.

6.2.2 Analysis of the most suitable sensor specifications

This method was developed for points in the middle layer of a sand deposit, out of the disturbance associated to the surface and the bottom. Thus, this analysis was now performed solely for the sensors located between a depth equivalent to $\sigma'_v = 50\ kPa$ from the surface and 3 m from the bottom. By doing this, a lot of transducers located in the top-most area of the models where eliminated, reducing the sample size but increasing the accuracy. The reason why $\sigma'_{v,min}$ is increased from 15 kPa to 50 kPa is because it is difficult for the methods to have good predictions near the top. The reasons for this are: the stiffness of the soil near the surface is more difficult to evaluate, as can be seen by the change in shear wave velocity (figure 6.6); the r_u changes due to the change in effective stress not being followed by identical change in pore pressure at shallow depths. In fact, close to the surface, it shows sudden variation in these parameters due to the dependence of G and r_u on the effective vertical stress.

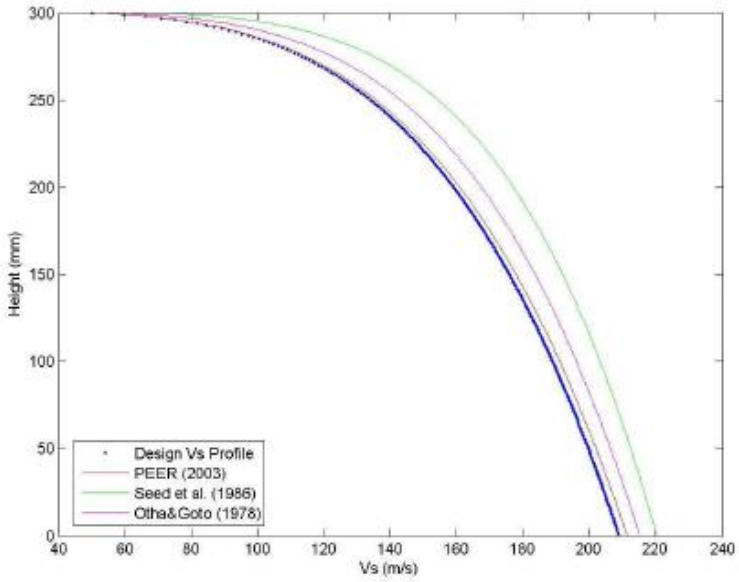

Figure 6.6- Shear velocity with depth in the model scale (Airoldi et al., 2018)

6.2.2.1 Test-cases affected by liquefaction

As it is now shown in figure 5.5 and table 6.4, by reducing the size of the sample, both the average error and the correct estimations of the t_{liq} improve for all predictions: in both the closed-form and the linear case the correct estimations rise to 100%, whilst the non-linear case merely rises to 33%. As they have the same CE, the only defining parameter is the averaged error, where the linear shows the best results for t_{liq}.

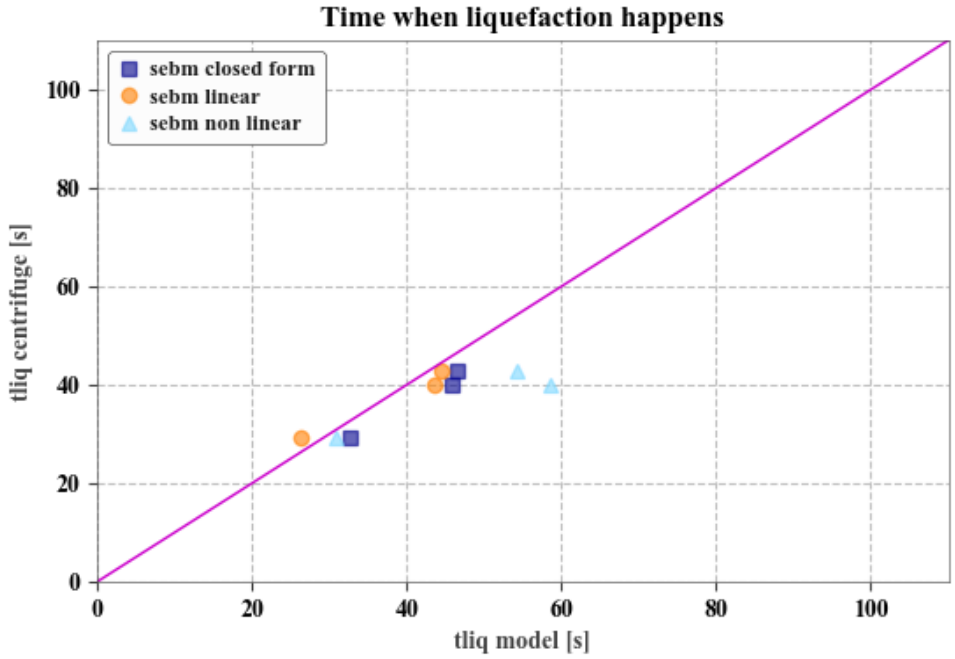

Figure 6.7- Comparison of tliq prediction considering only the most reliable sensors

Table 6.4- Statistical results of the tliq prediction considering only the most reliable sensors

	T_{liq} SEBM		
	Closed-form	Non-linear	Linear
$\overline{\chi}$ (%)	12	26	8
CE (%)	100	33	100

6.2.2.2 Test-cases unaffected by liquefaction

Concerning the r_u, as is shown in figure 6.8 and table 6.5, the changes are not as significant. This is due to the fact that the transducers where liquefaction did not happen are mainly located in the middle of the soil profiles, where the SEBM is already rather accurate. As for the quality of the results, the change is better in all three predictions, with the non-linear having the highest CE and the linear approach having the lowest $\overline{\chi}$.

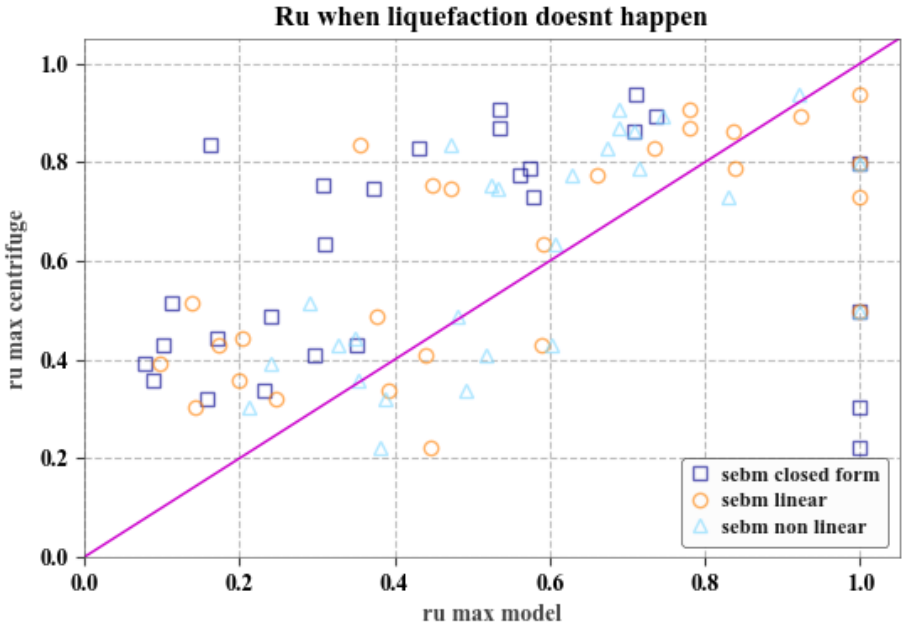

Figure 6.8- Comparison of ru prediction considering only the most reliable sensors

Table 6.5- Statistical results of the ru prediction considering only the most reliable sensors

	r_u SEBM		
	Closed-form	Non-linear	Linear
$\bar{\chi}$ (%)	65	27	35
CE (%)	11	37	41

While the test results where liquefaction occurs predict the linear approach as the most accurate, the test results where liquefaction does not occur consider both the non-linear and the linear approaches as fitting of the centrifuge results. As the t_{liq} is more important than the results of the r_u because it is the main parameter on the cases where liquefaction occurred, the linear approach is most fitting to evaluate the triggering of liquefaction.

6.3 Stress-based method

In this section, the validation of the stress-based method, idealized by Seed et al. (1975) and later simplified by Booker et al. (1976), is performed. Initially, the r_u build up predicted by Booker (in equation 25) is analysed. Where the ratio $\frac{N_L}{N}$ is calculated as (equation 61):

$$\frac{N_L}{N} = \sum N_{ref} \cdot \left(\frac{CSR_{15}}{CSR}\right)^{1/b} \quad (61)$$

Being,

N_{ref} the reference number of uniform cycles, equal to 15 for a magnitude equal to 7.5

CSR_{15} provided in Table 1

CSR calculated with equation (62) where a peak counting method was used to identify the acceleration peaks (acc_{peaks}), counting the largest peak between successive zero crossing.

$$CSR = \left|acc_{peaks}\right| \cdot \frac{\sigma_{v0}}{\sigma'_{v0}} \cdot r_d \quad (62)$$

Additionally, in order to better estimate the error in the closed form relationship, a calibration of the value CSR_{15} was performed. For this purpose, the $r_{u,max}$ predicted by the SBM in equation (25) and the $r_{u,max}$ obtained from the centrifuge test results are compared and $\left(\frac{N}{N_L}\right)_{max}$ is determined for each case (equations 63, 64):

$$r_{u,max.centrifuge,i} = \frac{2}{\pi}\, arc\sin\left[\left(\frac{N}{N_L}\right)_{max,i}^{\frac{1}{2\beta}}\right] \quad (63)$$

$$\left(\frac{N}{N_L}\right)_{max,i} = \sin\left(\frac{\pi}{2} \cdot r_{u,max.centrifuge,i}\right)^{2\beta} \quad (64)$$

As the $\left(\frac{N}{N_L}\right)_{max,i}$ is obtained, $CSR_{15,i}$ is calculated for each case from equation (61) using the value $\left(\frac{N}{N_L}\right)_{max,i}$ obtained from the equation 64 as follows (equation 65):

$$CSR_{15,i} = \sum\left[\frac{1}{N_{ref}} \cdot \left(\frac{N}{N_L}\right)_{max,i}\right]^b \cdot CSR_i \quad (65)$$

Once the value of $CSR_{15,i}$ obtained in (65), the average value of $CSR_{15,i}$ is calculated for all the *n* cases in equation (66) resulting in the CSR displayed in table 6.6. When comparing these results with table 6.1, a small reduction of the CSR values of the Ticino Sand and a significant increase for both the values of Pieve di Cento Sand can be noticed.

$$CSR_{15,average} = \frac{\sum_{i=0}^{n} CSR_{15,i}}{n} \quad (66)$$

Table 6.6- $CSR15_{,average\ values}$

	CSR
Ticino Sand	0.23
Pieve di Cento sand	0.28
Clean Pieve di Cento Sand	0.30

Then, $CSR_{15,average}$ is used in equation (26) and the new value of the ratio $\frac{N_L}{N}$ is obtained (equation 67):

$$\frac{N_L}{N} = \sum N_{ref} \cdot \left(\frac{CSR_{15}}{CSR_{15,average}}\right)^{1/b} \quad (67)$$

Finally, the $\frac{N_L}{N}$ is used in the equation (26) and the calibrated behaviour of r_u is obtained.

6.3.1 Validation of the model

As was done for the SEBM, the comparison between the pore pressure build-up calculated by the two different SBM predictions and the one obtained by the centrifuge test results is shown in Figure 6.8. Test 2 was selected as representative since it is performed in free-field condition and absence of a structure. In this case, the implementation that best fits the centrifuge results is the calibrated solution, however, as will be subsequently shown, the best fitting method changes from case to case.

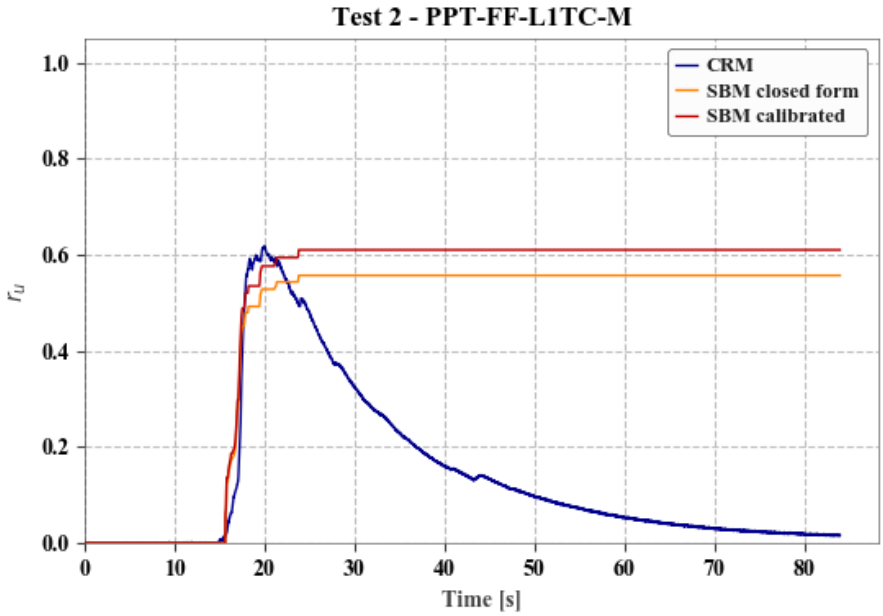

Figure 6.9- Comparison between ru build-up of the two SBM predictions and the centrifuge results.

Once the behaviour of the selected transducers was evaluated for each test, each r_u prediction was compared to the one obtained from the centrifuge tests. For this purpose, the same distinction was carried out: tests were liquefaction happened where separately studied from the ones unaffected by the phenomenon.

6.3.1.1 Test-cases affected by liquefaction

As it is shown in figure 6.9, the t_{liq} of both SBM predictions are almost identical. This is due to the fact that the transducers where liquefaction was achieved being in Ticino Sand models and that there is little change in the CSR of the Ticino Sands between the closed form (0.24) and the calibration (0.23).

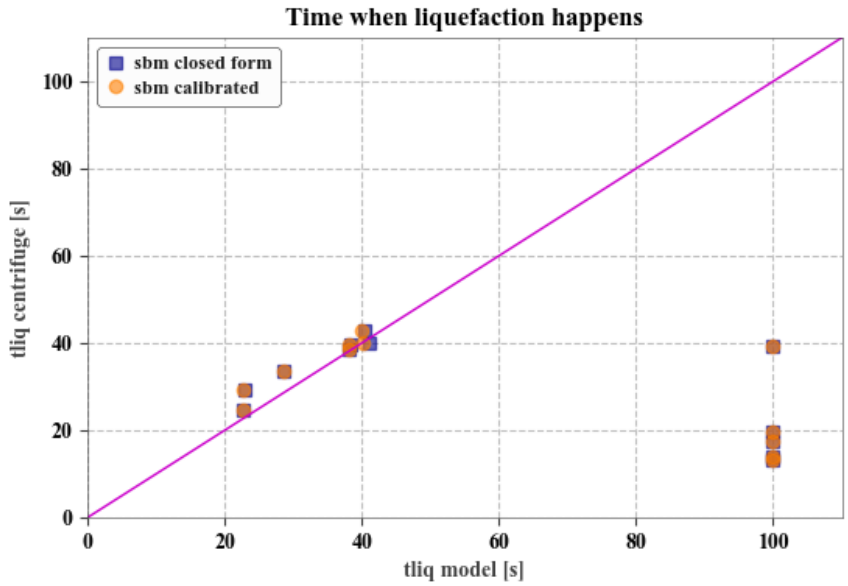

Figure 6.10- Comparison between predicted tliq by the two SBM curves and centrifuge test results

The averaged error ($\overline{\chi}$) of the results and the correct estimations (CE) were also considered as statistical parameters for the SBM (table 7). Both methods show similar predictions due to similar CSR values as mentioned before.

The behaviour explicit in figure 4 can also be seen here, justifying the results where the model and the centrifuge results are very different and the high averaged error, given the acceptable CE.

Table 6.7- Statistical results of the tliq in the two SBM predictions

	T_{liq} SBM	
	Closed-form	Calibration
$\overline{\chi}$ (%)	165	165
CE (%)	42	42

6.3.1.2 Test-cases unaffected by liquefaction

Concerning the r_u, as is shown in figure 6.10 and table 6.8, there are some changes between both predictions. In fact, an improvement of the results passing from the closed form to the calibration can be observed. One reason for this improvement is due to a more accurate

prediction for the transducers located in both Ticino and Pieve di Cento models. Thus, pointing to more accurate results of the CSR used.

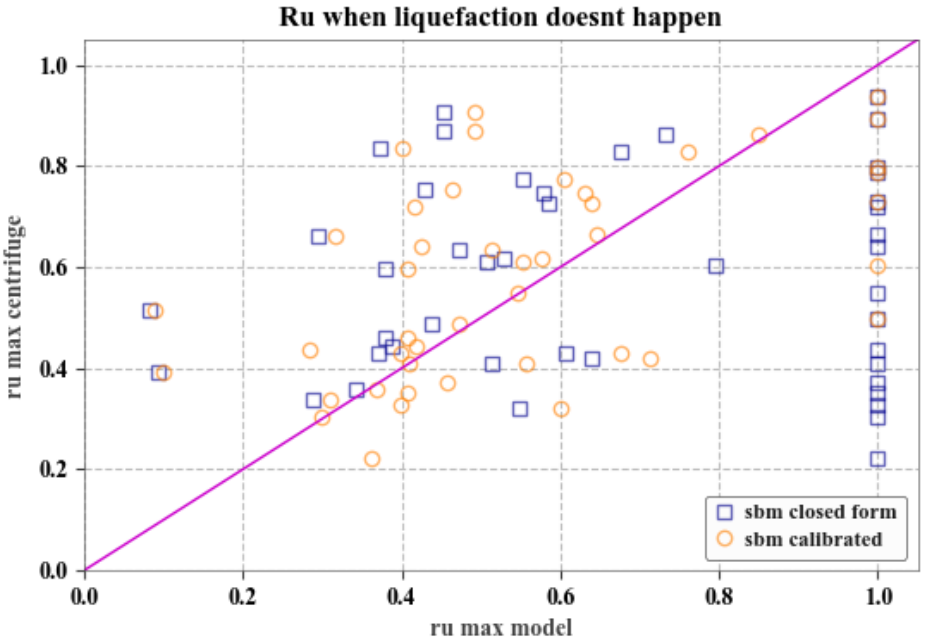

Figure 6. 11- Comparison between predicted ru by the two SBM curves and centrifuge test results

Table 6.8- Statistical results of the ru in the two SBM predictions

	r_u SBM	
	Closed-form	Calibration
$\overline{\chi}$ (%)	63	30
CE (%)	30	45

6.3.2 Analysis of the most suitable sensor specifications

As mentioned for the SEBM, the effectiveness of this model relies on the evaluation of the middle layer of a soil deposit, due to the disturbance at the surface and the bottom. Thus, this analysis was also performed solely for the sensors located between a depth equivalent to $\sigma'_v = 50\ kPa$ from the surface and 3 m from the bottom.

6.3.2.1 Test-cases affected by liquefaction

As it is now shown in figure 6.11 and table 6.8, by reducing the size of the sample, the average error of the t_{liq} drops greatly. Still, as in Section 6.3.1.1, the results of both predictions that were identical are now slightly different, with the calibration being better. The correct estimations have now passed from 43% to 66%.

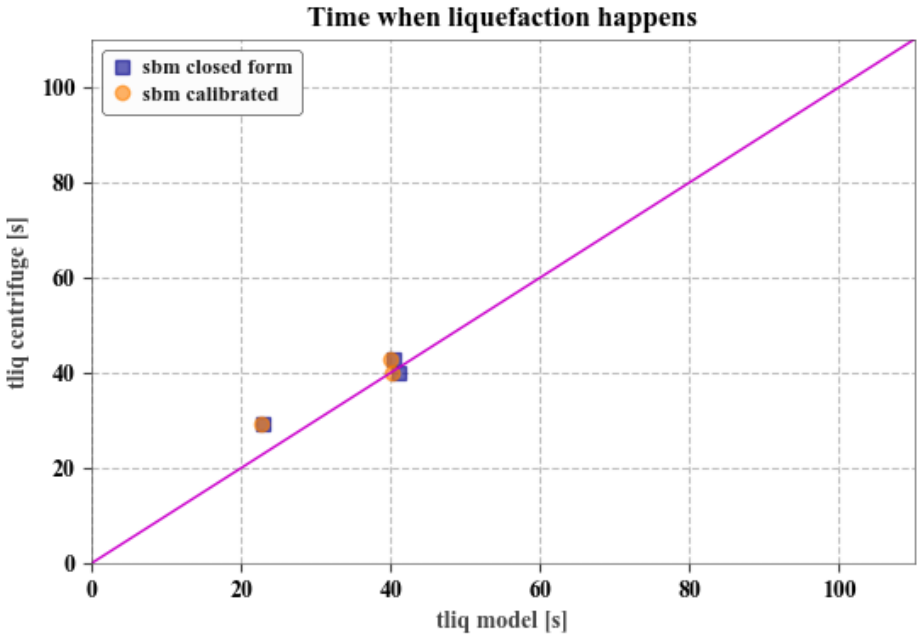

Figure 6.12- Comparison of tliq prediction considering only the most reliable sensors

Table 6.9- Statistical results of the tliq prediction considering only the most reliable sensors

	T_{liq} SBM	
	Closed-form	Calibration
$\overline{\chi}$ (%)	10.5	10.1
CE (%)	66	66

6.3.2.2 Test-cases unaffected by liquefaction

Concerning the r_u, as is shown in figure 6.12 and table 6.10, the changes are not as significant. This is due to the fact that the transducers where liquefaction did not happen are mainly located in the middle of the soil profiles. As for the quality of the results, the change was for the better in both predictions, with the calibration being clearly better.

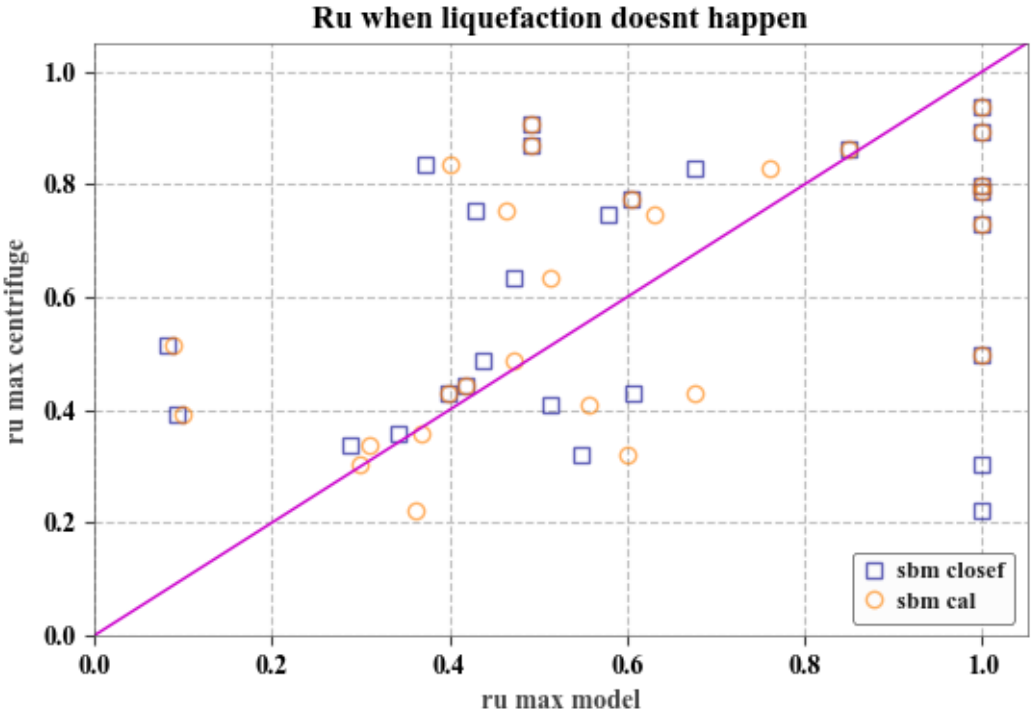

Figure 6. 13- Comparison of ru prediction considering only the most reliable sensors

Table 6.10- Statistical results of the ru prediction considering only the most reliable sensors

	r_u SBM	
	Closed-form	Calibration
χ (%)	54	33
CE (%)	33	44

As it was expected, due to the t_{liq} results being very similar in both predictions, it leaves the r_u results as the only pondering factor, pointing to the calibration as the best prediction of the SBM and the necessity of getting accurate CSR results for each analysis. As mentioned to the SEBM, in a real case the CSR could be determined by laboratory tests (if available) which would improve the prediction.

6.3 Comparison of the two methods

In this section, the increase of pore pressure of the SEBM and the SBM are compared in their closed-form. In Figure 6.13 are shown r_u predictions of both methods together with the centrifuge results. Test 2 was selected as representative since it is performed in free-field condition.

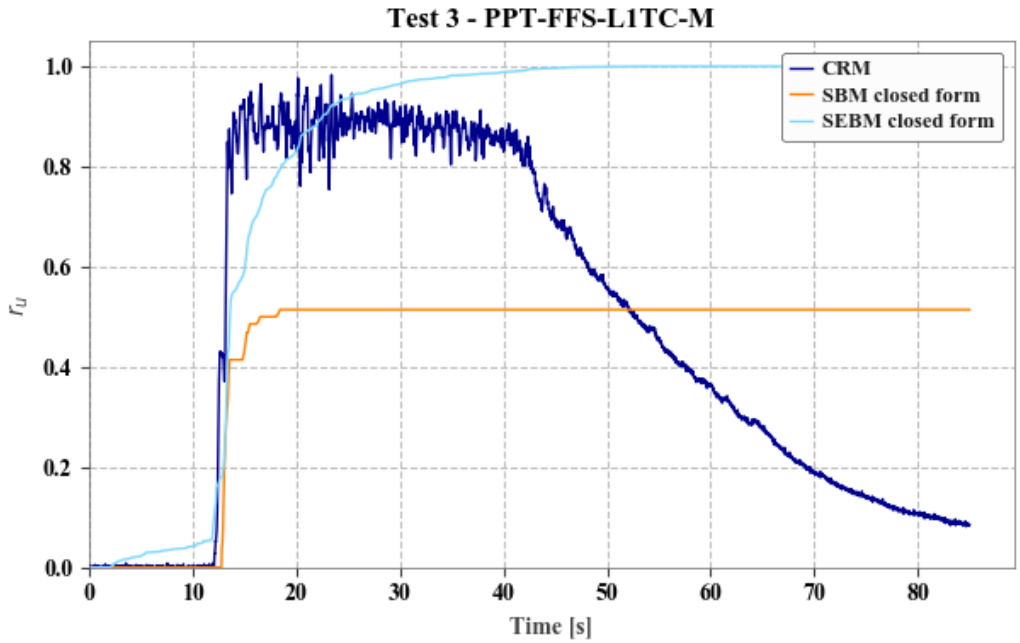

Figure 6. 14- Comparison between ru build-up of the stress-based method, energy-based method and centrifuge result

6.4.1 Validation of the models

The same statistical analysis previously performed, by determining the average error and CE of the t_{liq} and the r_u , is carried out.

6.4.1.1 Test-cases affected by liquefaction

As it is shown in figure 6.14, the t_{liq} of both SBM and SEBM predictions are fairly different. In fact, the SEBM is more accurate when not accounting for the calibration. A visual feedback is shown in table 6.11: as stated in both previous analyses there are huge errors due to the

misprediction of liquefaction, nevertheless, the error was found more often in the SBM., and therefore the number of correct estimations is also lower in the SBM.

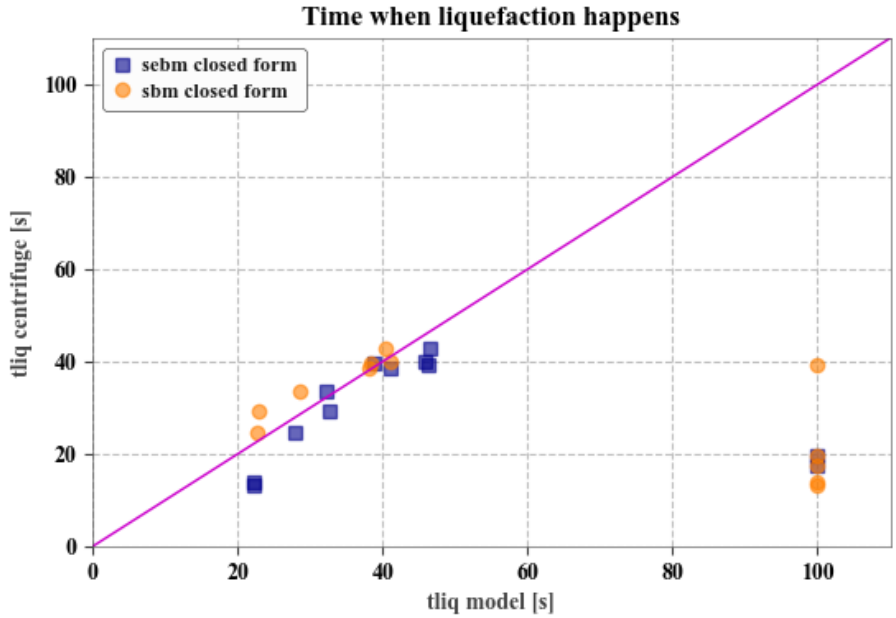

Figure 6.15- Comparison between predicted tliq by the SBM and SEBM curves and centrifuge test results

Table 6.11- Statistical results of the tliq in the two method predictions

	t_{liq}	
	SEBM	SBM
χ (%)	71	165
CE (%)	67	42

6.4.1.2 Test-cases unaffected by liquefaction

Concerning the r_u, as is shown in figure 6.15 and table 6.12, there are some differences between both predictions. Particularly, the SBM is observed to give a better prediction of the r_u build-up. Although the SBM also has more cases where it wrongly predicts full liquefaction, in most cases, where both methods underpredict the r_u build-up, the SBM results are better.

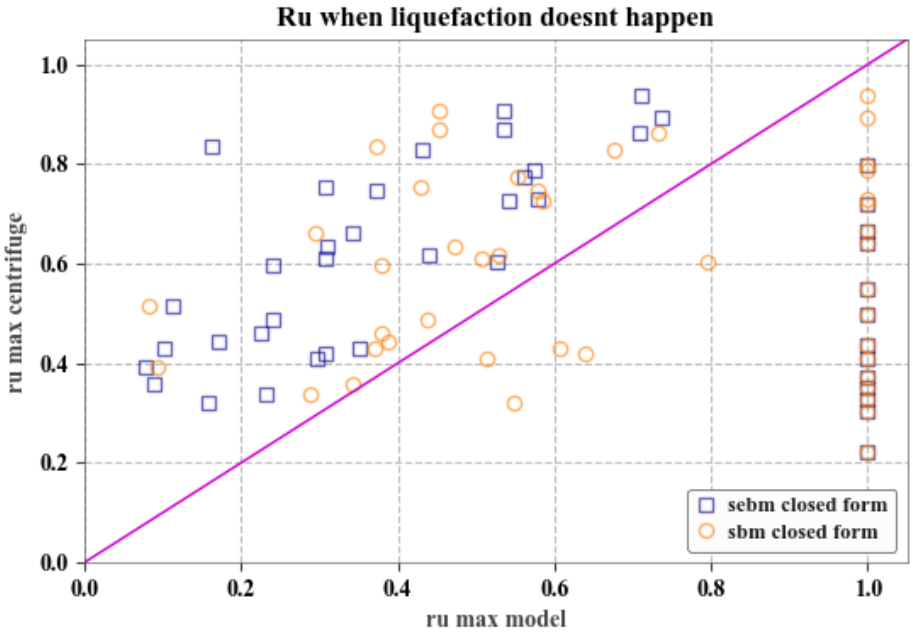

Figure 6.16- Comparison between predicted ru by the SBM and SEBM curves and centrifuge test results

Table 6.12- Statistical results of the tliq in the two method predictions

	r_u	
	SEBM	SBM
χ (%)	71	63
CE (%)	9	30

6.4.2 Analysis of the most suitable sensor specifications

As mentioned for both methods, the effectiveness of these models relies on the evaluation of the middle layer of a soil deposit, due to the disturbance at the surface and the bottom. Thus, this analysis was also performed solely for the sensors located between a depth equivalent to $\sigma_v' = 50\ kPa$ from the surface and 3 m from the bottom.

6.4.2.1 Test-cases affected by liquefaction

As it is now shown in figure 6.16 and table 6.13, by reducing the size of the sample, the average error of the t_{liq} drops greatly in both the SBM and the SEBM. This highlights the

effectiveness of the SEBM accuracy due to its reduced average error (12%) and high CE (100%).

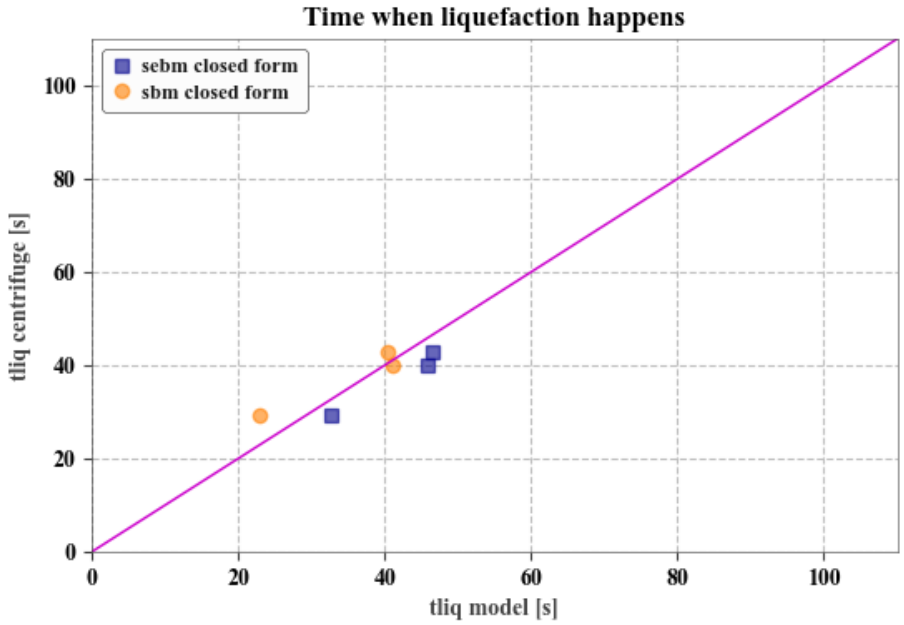

Figure 6.17- Comparison of tliq prediction considering only the most reliable sensors

Table 6.13- Statistical results of the tliq in the two method predictions considering only the most reliable sensors

	t_{liq}	
	SEBM	SBM
χ (%)	12	10.5
CE (%)	100	67

6.4.2.2 Test-cases unaffected by liquefaction

Concerning the r_u, as is shown in figure 6.17 and table 6.14, the changes are not as significant. This is due to the fact that the transducers where liquefaction did not happen are mainly located in the middle of the soil profiles. As for the quality of the results, the change was for the better in both predictions, with the SBM still being clearly better.

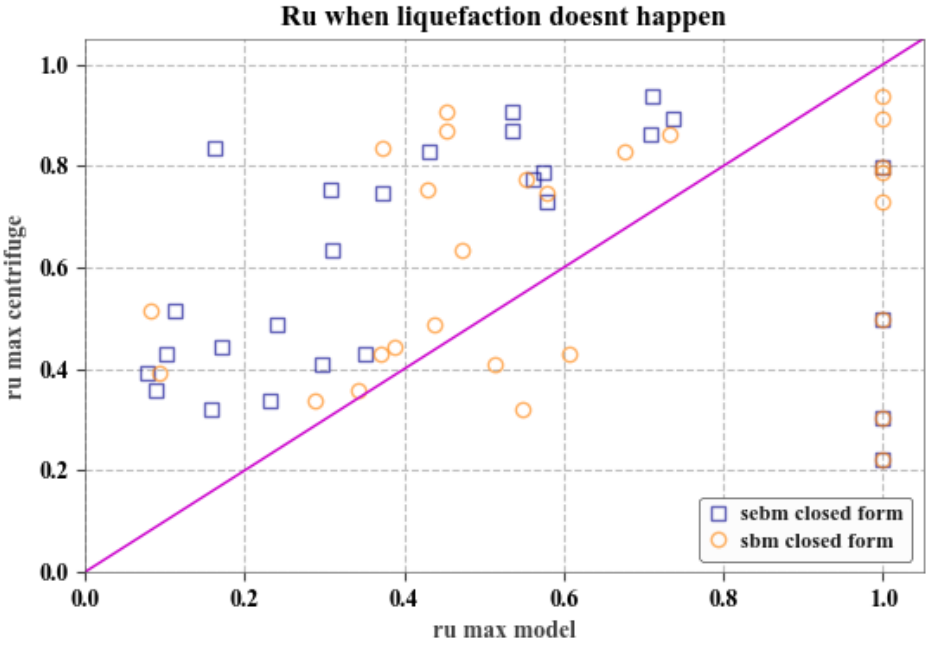

Figure 6.18- Comparison of ru prediction considering only the most reliable sensors

Table 6.14- Statistical results of the ru in the two method predictions considering only the most reliable sensors

	r_u	
	SEBM	SBM
χ (%)	65	54
CE (%)	11	33

As the t_{liq} is more important than the results of the r_u because it is the main parameter on the cases where liquefaction occurred, the SEBM can be considered more accurate than the SBM in predicting the triggering of liquefaction.

6.5 Adjustment of $r_{u,liq}$

It was observed that some transducers, which recorded a value of r_u higher than 0.9 did not reach the imposed value of $r_{u,liq}$, mispredicting the occurrence of liquefaction. This behaviour is due to the linear increase of $r_{u,liq}$ with depth, which leads to a high values of $r_{u,liq}$ at high depths.

In order to avoid values of $r_{u,liq}$ higher than 0.9, a constant value $r_{u,liq}$=0.9 was imposed and the analysis was performed again. The obtained results are shown in Figure 6.18, where the theoretical value of $r_{u,liq}$ along the depth resulting from equation 1 is plotted together with the constant one ($r_{u,liq,adjusted}$ = 0.9). Also, on the same graph, the points representing centrifuge test with an $r_{u,max}$ higher than 0.9 are shown (Table 6.15): it is possible to observe that two points which did not represent the triggering of liquefaction with the previous criterion for $r_{u,liq,}$, are now considered indicators of liquefaction occurring.

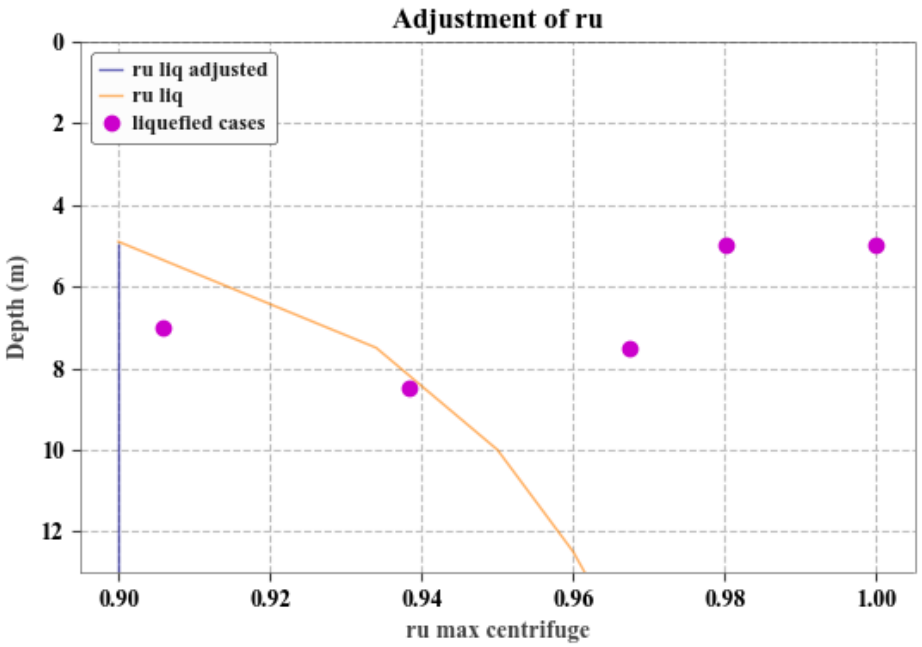

Figure 6.19- Adjustment of ru,liq

Table 6.15- New liquefied cases

Depth z (m)	Max pore pressure (kPa)	Initial pore pressure (kPa)	σ'_v [kPa]	ru
5.00	82.812	30.602	53.272	0.98
5.00	91.942	38.413	53.269	1.00
7.00	105.150	45.941	65.367	0.91
7.50	135.173	61.258	76.411	0.97
8.50	144.769	63.815	86.276	0.94

6.5.1 Test-cases affected by liquefaction

The same statistical analysis performed for the SEBM and SBM in their closed forms, for the selected sensors affected by liquefaction. The results for the t_{liq} are shown in figure 6.19 and table 6.16. As desired, the sample not only grew in size, but the results of the SEBM also improved, whilst the results of the SBM worsened.

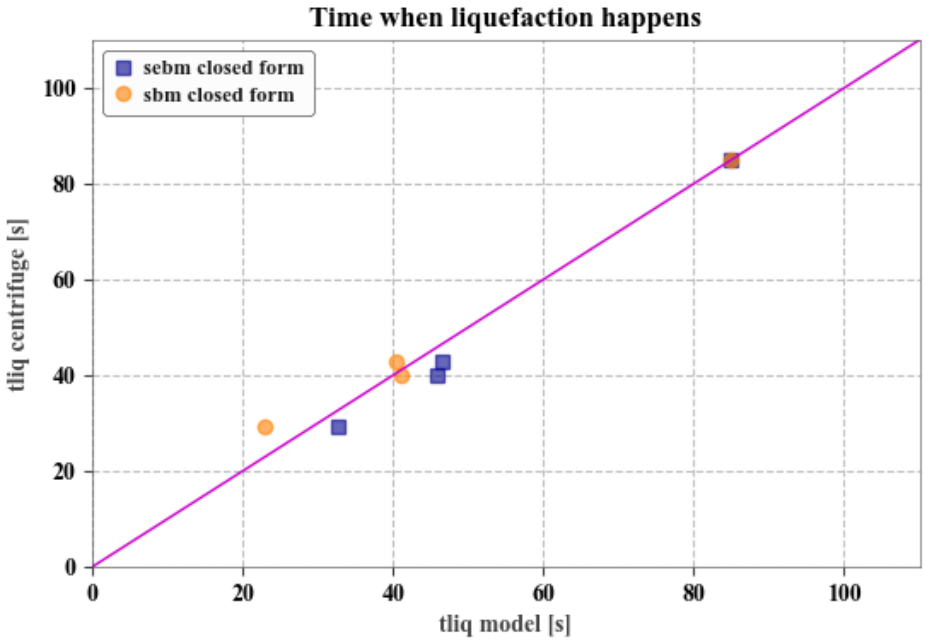

Figure 6. 20- Comparison of tliq prediction considering only the most reliable sensors

Table 6.16- Statistical results of the tliq in the two method predictions considering only the most reliable sensors

	t_{liq}	
	SEBM	SBM
χ (%)	7	21
CE (%)	100	60

6.5.2 Test-cases unaffected by liquefaction

The same statistical analysis performed for the SEBM and SBM in their closed forms, for the selected sensors unaffected by liquefaction. The results for the r_u are shown in figure 6.20 and table 6.17, where the results of both SEBM and SBM worsen.

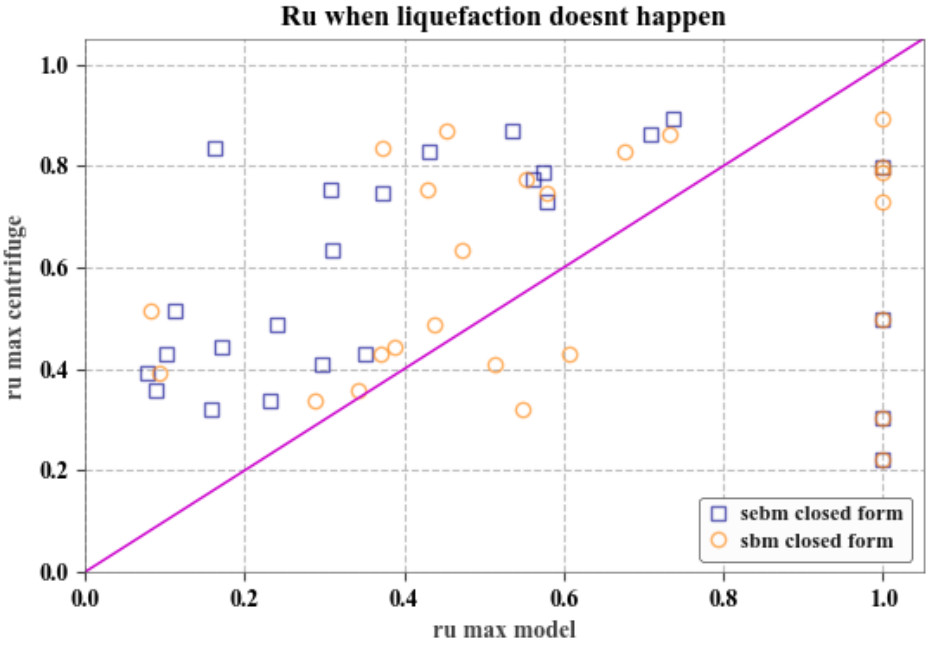

Figure 6.21- Comparison of ru prediction considering only the most reliable sensors

Table 6.17- Statistical results of the tliq in the two method predictions considering only the most reliable sensors

	r_u	
	SEBM	SBM
χ (%)	68	56
CE (%)	12	32

In conclusion, by adjusting the $r_{u,liq}$ limit, some of the sensors which did not indicate the occurrence of liquefaction are now showing its triggering, leading to a slightly wider sample for the t_{liq} analysis. Additionally, there was an improvement of the results on the SEBM, whilst the results of the SBM worsened.

6.6 Evolution of r_u along a model

From the analyses carried out in Section 6.4, both SEBM and SBM often underpredicted the occurring of liquefaction. In this section, some key aspects of the porewater behaviour inside the model are shown trough the evolution over time of the r_u along a vertical axis. Since only the most suitable sensors are analysed, the pore pressure transducer placed at the bottom of the model was taken out from the analysis. Test 3 is shown as a representative model, since it is

performed in free-field condition. Figure 6.21 shows the acceleration series at the base of Test 3 and in Figures 6.22, 6.23 and 6.24 can be seen the curves of the SEBM, SBM and centrifuge results for the three transducers further analysed in this section.

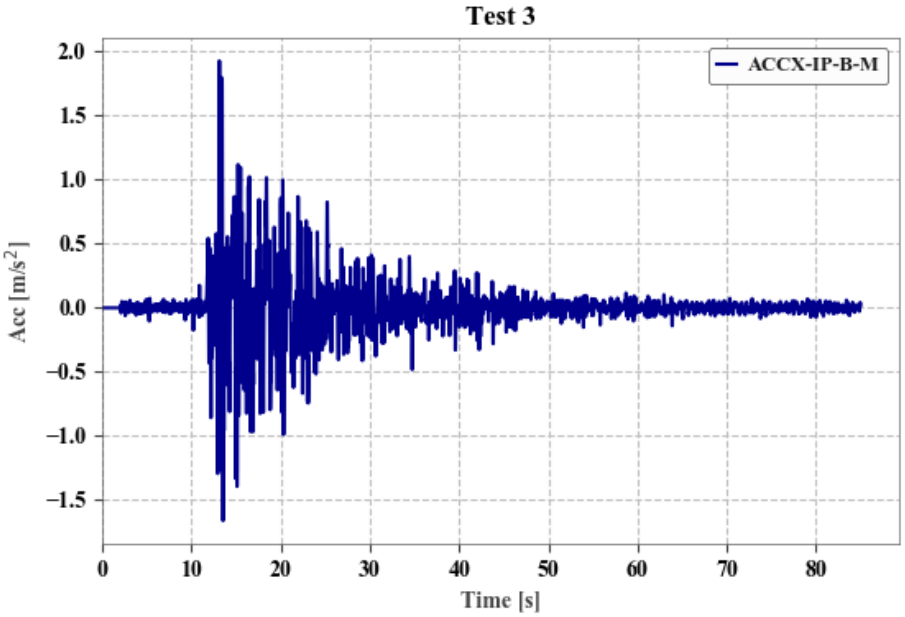

Figure 6.22- Input ground motion of Test 3

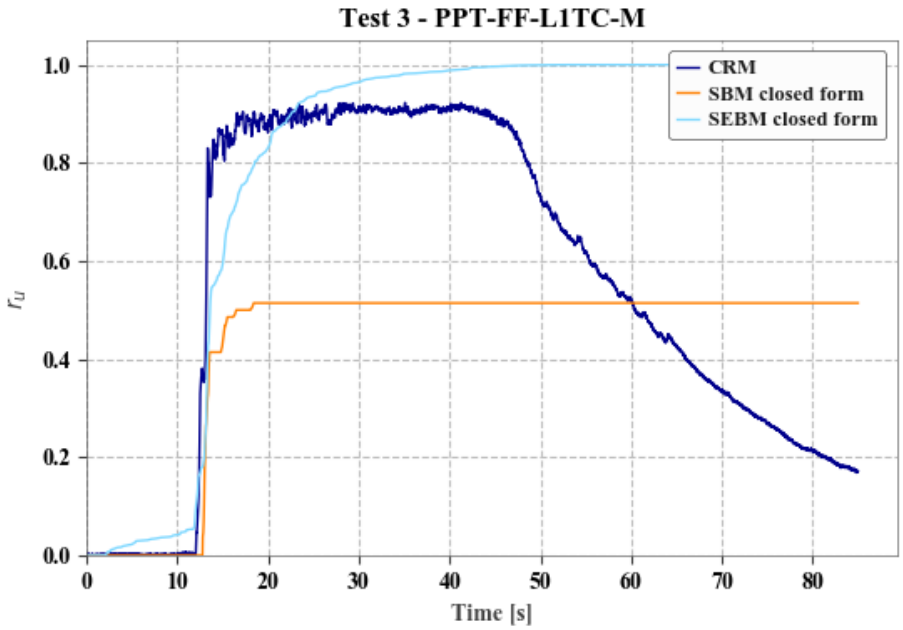

Figure 6.23- Comparison between ru build-up of the SEBM, SBM and centrifuge results of the top-centre transducer of Test 3

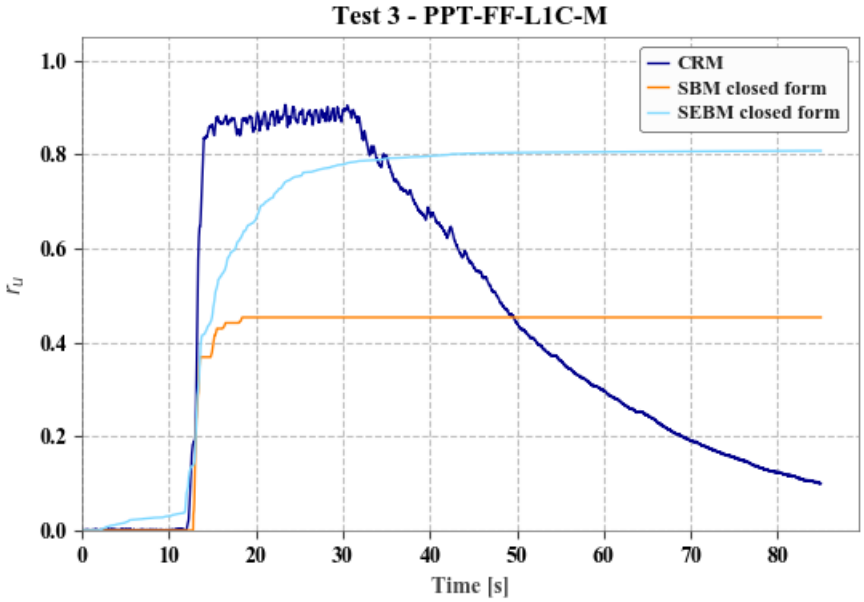

Figure 6.24- Comparison between ru build-up of the SEBM, SBM and centrifuge results of the centre transducer of Test 3

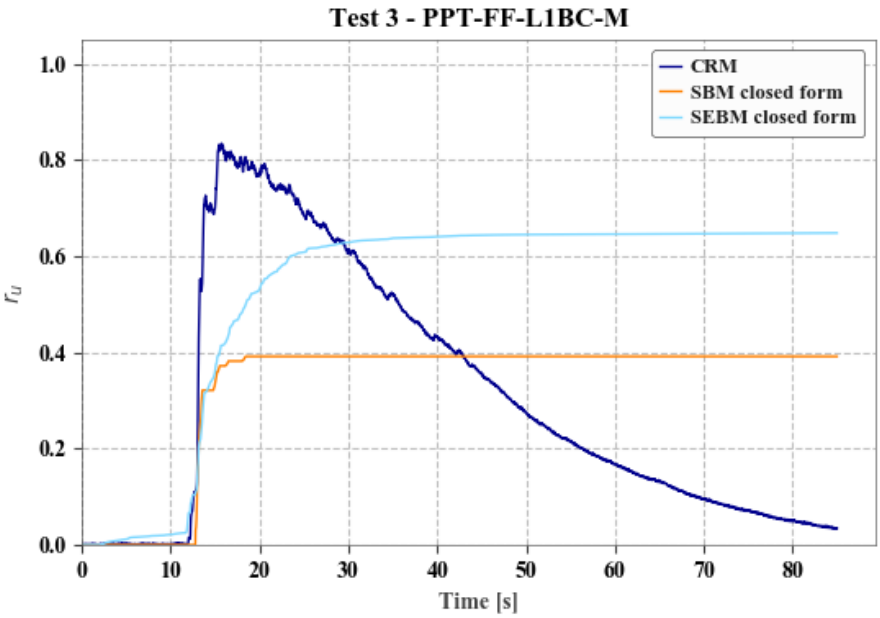

Figure 6.25- - Comparison between ru build-up of the SEBM, SBM and centrifuge results of the bottom-centre transducer of Test3

The trend of r_u along the model (Figure 6.25) is represented at four critical time frames:

- In the initial part of the test (t=12s), when the pore water is in hydrostatic conditions: while the trend predicted by the SBM faithfully follows the empirical distribution, the SEBM slightly overpredicts the centrifuge results;
- Right after the first acceleration peak (t=14s): both SEBM and EBM are underpredicting the r_u values along the model, while the centrifuge results show a high value of r_u along the whole soil deposit. On the centrifuge distribution, a similar value of r_u is measured on the top and the centre of the model, and as the σ'_v is higher with depth, the obtained trend is explained with a seepage toward the centre of the box.
- In correspondence to the timeframe where, on average, the soil reaches its maximum value of r_u (t=25s), the trend previously obtained (t=14s) is now slightly accentuated. Also, in this case the prediction of the r_u is much lower than the SBM prediction, while the SEBM trend is closer to the empirical trend. Obviously, since the water flow is not provided by the prediction, r_u shows a linear decrease with depth.
- When the ground motion is over (t=40s), both the theoretical predictions show the same trend (SBM) or a further increase (SEBM) of r_u along the model, which is not physically coherent. A drop of r_u is observed on the bottom and centre of the deposit due to the dissipation of the pore pressure. On the other hand, the top keeps a higher value of r_u for longer. As it has been previously said, this is due both to the upward seepage previously described and to the total reflection of the seismic waves close to the surface, which increase the duration of energy input on the superficial layer.

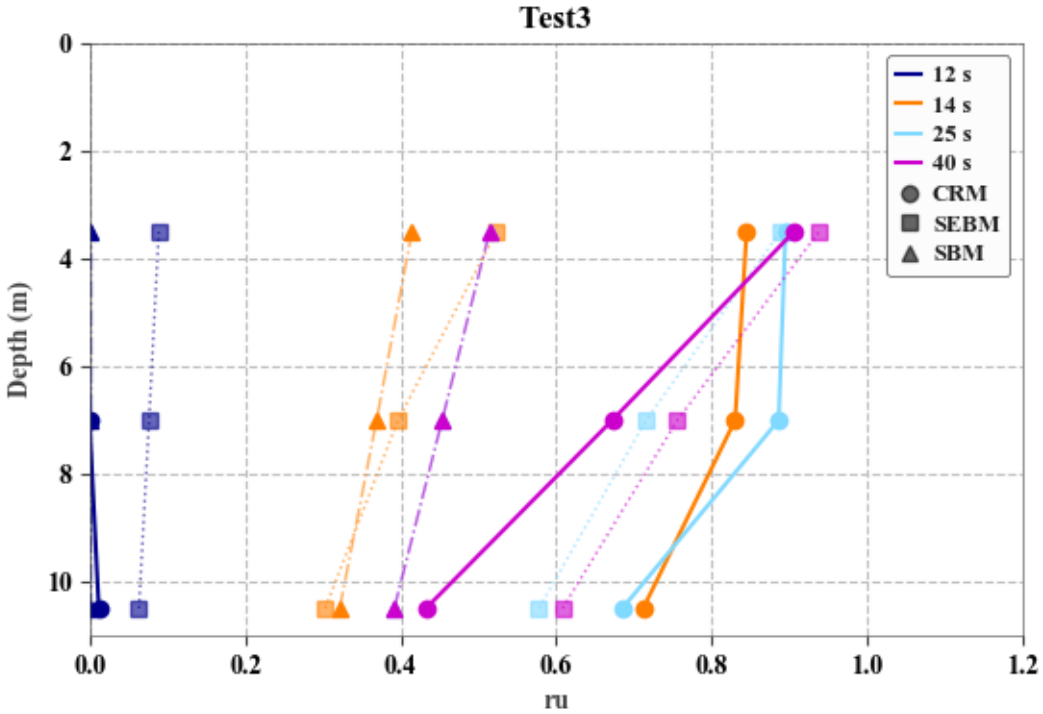

Figure 6.26 -Evolution of r_u over time along a vertical axis

As previously stated, the methods can only predict accurate results up to the time where liquefaction first occurs. Furthermore, as not all transducers reach the $r_{u,liq}$, the methods results turn out not to be as accurate, due to the method's difficulty in being precise when liquefaction does not happen. Finally, as the methods do not account for seepage (a rather impactful phenomenon in liquefaction analyses), it is understandable that they often underpredict the excess pore pressure.

7. FINAL CONCLUSIONS

In this thesis, data resulting from physical geotechnical modelling activities performed at ISMGEO are treated. Indeed, a set of thirty-seven reduced-scale centrifuge tests are analysed, with the following outputs:

- a database of results converted to prototype units is created and made available for the analysis performed in this document and to be used as a benchmark for future analyses. Particularly, during the conversion phase, the name of the sensors in the models is standardised so that the user can easily understand where the sensor is, improving communication between different researchers as defended by Millen et al. (2018) and Rios et al. (2019).
- The ground motion change due to liquefaction is observed in the centrifuge results by analysing the *Fourier Amplification Function* (FAF) and the frequency content. In fact, in the *FAF* of the soil characterized by a high value of pore pressure ratio, the peaks are translated towards low values of frequency and, at the same time, the amplitude of the peaks is affected by an attenuation. The mentioned drop of the high frequency content is also highlighted on the *Stockwell transform*. In addition, on the *S-transform*, the decreasing of the high frequency content along time is shown.
- The presence of horizontal drains has a double effect on the model. The pore pressure amplitude peak measured by the transducers is halved and a sudden decrease of the pore pressure peak values along the vertical axis of the box is generated, especially if the drain arrangement is dense.
- The use of induced partial saturation (IPS) on the models produces a noticeable reduction of the pore pressure ratio in the area close to the bottom where the injection is made up to the centre of the model. Although the improvement is significant at higher depths, it is believed that the air injection is not enough to reach the "top-centre" part of the model, where the maximum values of pore pressure ratio are reached (r_u = 1) on the analysed tests. In conclusion, even though IPS is effective in most of the model, it still leaves the top-most part of the model in liquefiable condition, so it could be interesting to evaluate the effect of several injectors, not only spread in the bottom of the model but also closer to the top-centre area, where liquefaction happens.

- The presence of seepage in the box during the motion is verified: the water flows from the bottom of the model towards the ground surface. Moreover, after the end of the motion, the surface layer stays with high pore pressure ratio values for a larger period of time. This behaviour could be explained by the upward seepage previously described and the total reflection of the seismic waves close to the surface, which increases the duration of energy input on the surface layer.
- The settlement in presence of mitigation measures is observed to be up to one third compared to the one occurred in absence of countermeasures.
- The Strain-energy based method (Millen et al., 2019)-SEBM is validated using its closed form as well as a linear calibration and a non-linear calibration of the parameter $NCASE_{liq}$, which represents the normalised strain energy at liquefaction.
- The Stress based method (Seed et al., 1975) is validated in its closed-form and along a calibration of the parameter CSR_{15}. The analysis proves an improvement of the results passing from the closed-form to the calibrated solution. This finding emphasizes the necessity of getting accurate CSR results for each analysis. In a real case the CSR could be determined by laboratory tests (if available) which would improve the prediction.
- When comparing both methods in their closed-form, in was concluded that, although both methods have very accurate results, the SEBM still has more accurate predictions.

7.1 Future Development

This work was right at the start limited by the size of the centrifuge results analysed. With more time it could have been possible to construe other centrifuge analyses where several other mitigation techniques are employed or merely in a different way. With this, it could have been possible to reach a better understanding of how recent techniques, such as IPS, affect the soil.

Regarding the Strain Energy Based Method, since it as recent method, more validation is needed with other centrifuge results. In particular, further improvements can be made testing other relationships for the calculation of the normalised strain energy at liquefaction, or using other pore pressure models instead of the square root relationship selected in the present version of the method.

Both simplified methods used in this work rely on the value of CSR_{15}. For the Clean Pieve di Cento Sand it was assumed that this value was equal to the value of the natural Pieve di Cento

sand, disregarding the influence of the fine content on CSR_{15}. In addition, since it is known that CSR_{15} depends on the relative density, a more realistic estimation of this parameter could be achieved by obtaining the value of CSR_{15} from laboratory tests for each soil and for each relative density.

The centrifuge tests can be considered as one of the most advanced form of site investigation. Unfortunately, performing centrifuge tests is not straightforward, due to the large time and high cost needed to their execution. For this reason, a study aimed to the calibration of a 3D numerical model (for instance in PLAXIS) using these centrifuge tests could be useful to reach a better understanding how the soil behaviour varies by changing some parameters, for example with a different drain arrangement or a variation of the air injector position.

REFERENCES

A. Flora, E. Bilotta, V. Nappa, A. Chiaradonna, G. Fasano, S. Lirer, J. Quintero, M.D.L. Millen, A. Viana da Fonseca, C.G. Lai, G. Andreotti, A.G. Özcebe, F. Bozzoni, E. Zuccolo (2019). Database of calibrated numerical modelling results. *LIQUEFACT Project Deliverable D4.1, Horizon 2020 European Union funding for Research & Innovation Project ID:* 700748 (www.liquefat.eu)

Airoldi, S., Fioravante, V., Giretti, D., and Moglie, J. (2018). Report on validation of retrofitting techniques from small scale models. *LIQUEFACT Project Deliverable D4.2, Horizon 2020 European Union funding for Research & Innovation Project ID:* 700748 (www.liquefat.eu)

Allard, M.A. and Schenkeveld (1994) The Delft Geotechnics model pore fluid, Centrifuge 94. Leung, Lee & Tan (eds), Balkema, Rotterdam

Ambraseys (1988) NN. "Engineering Seismology: Part I." *Earthquake engineering & structural dynamics* 17, no. 1: 1-50.

Berrill, JB, and RO Davis. (1985) "Energy Dissipation and Seismic Liquefaction of Sands: Revised Model." *Soils and Foundations* 25, no. 2: 106-18.

Booker, John R, M Shamimur Rahman, and Harry Bolton Seed. (1976) "Gadflea: A Computer Program for the Analysis of Pore Pressure Generation and Dissipation During Cyclic or Earthquake Loading."

Boulanger, Ross W, and IM Idriss. (2006) "Liquefaction Susceptibility Criteria for Silts and Clays." *Journal of geotechnical and geoenvironmental engineering* 132, no. 11: 1413-26.

Boulanger, Ross W, and IM Idriss. (2015) "Magnitude Scaling Factors in Liquefaction Triggering Procedures." *Soil Dynamics and Earthquake Engineering* 79: 296-303.

Boulanger, Ross W, and IM Idriss. (2015) "Cpt-Based Liquefaction Triggering Procedure." *Journal of Geotechnical and Geoenvironmental Engineering* 142, no. 2: 04015065.

Bray J.D., Sancio R.B. (2016) “Assessment of the Liquefaction Susceptibility of Fine-Grained Soils”. *ASCE Journal of Geotechnical and Geoenvironmental Engineering*

Bray, J. and J. Macedo (2017). 6th Ishihara lecture: Simplified procedure for estimating liquefaction induced building settlement. *Soil Dynamics and Earthquake Engineering* 102, 215–231.

Eng-tools. https://eng-tools.github.io/naming-conventions.html (Consultado em Abril de 2019) (2010)

Foti, Sebastiano, CG Lai, and Maria Rota. (2009) "Input Sismico E Stabilità Geotecnica Dei Siti Di Costruzione." *Collana di manuali di Progettazione Antisismica* 6.

Garnier, J., C. Gaudin, S.M. Springman, P.J. Cullingan, D. Goodings, D. Konig, B. Kutter, R. Phillips, M.F. Randolph and L. Thorel. (2007) *IJPMG*, Vol. 3

Gingery, James R, Ahmed Elgamal, and Jonathan D Bray. (2015) "Response Spectra at Liquefaction Sites During Shallow Crustal Earthquakes." *Earthquake Spectra* 31, no. 4: 2325-49.

Green, RA, JK Mitchell, and CP Polito. (2000) "An Energy-Based Excess Pore Pressure Generation Model for Cohesionless Soils." *Paper presented at the Proceedings of the John Booker Memorial Symposium*, Sidney Australia, AA Balkema Publishers, Rotterdam, Netherlands.

Idriss, IM. (1999) "An Update to the Seed-Idriss Simplified Procedure for Evaluating Liquefaction Potential." *Proc., TRB Worshop on New Approaches to Liquefaction, Pubbl. n. FHWA-RD-99-165, Federal Highway Administation* .

Ishihara, Kenji. (1984) "Post-Earthquake Failure of a Tailings Dam Due to Liquefaction of Pond Deposit."

Ishihara, Kenji. (1985) "Stability of Natural Deposits During Earthquakes." *Proc. of 11th ICSMFE, 1985* 1: 321-76.

Ishihara K, Yoshimine M. (1992) "Evaluation of settlements in sand deposits following liquefaction during earthquakes". *Soils and Foundations*

Iwasaki, T. (1978) "A Practical Method for Assessing Soil Liquefaction Potential Based on Case Studies at Various Sites in Japan." *Paper presented at the Proc. Second Int. Conf. Microzonation Safer Construction Research Application*

Karamitros, D. K., Bouckovalas, G. D., and Chaloulos, Y. K. (2013a). Seismic settlements of shallow foundations on liquefiable soil with a clay crust. *Soil Dynamics and Earthquake Engineering*, 46, 64-76

Karamitros, D.K., Bouckovalas, G.D. and Chaloulos, Y.K. (2013b). Numerical analysis of liquefaction-induced bearing capacity degradation of shallow foundations on a two-layered soil profile. *Soil Dynamics and Earthquake Engineering*, 44:90-101

Karamitros, D. K., Bouckovalas, G. D., and Chaloulos, Y. K. (2013c). Insight into the Seismic Liquefaction Performance of Shallow Foundations. 139(4):599–607, DOI: 10.1061/(ASCE)GT.1943-5606.0000797.

Kishida, T., & Tsai, (2014) C.-C. Seismic Demand of the Liquefaction Potential with Equivalent Number of Cycles for Probabilistic Seismic Hazard Analysis. *Journal of Geotechnical and Geoenvironmental Engineering*, 140(3), 04013023. https://doi.org/10.1061/(ASCE)GT.1943-5606.0001033

Kokusho, Takaji. (2017) *Innovative Earthquake Soil Dynamics.* CRC Press.

Kokusho, Takaji. "Liquefaction Potential Evaluations: Energy-Based Method Versus Stress-Based Method." *Canadian Geotechnical Journal* 50, no. 10 (2013): 1088-99.

Kokusho, T. and Fujita, K. (2002) "Site investigation for involvement of water films in lateral flow in liquefied ground". *Journal of Geotech. and Geoenv. Eng.*

Kramer, SL, SS Sideras, and MW Greenfield. (2016) "The Timing of Liquefaction and Its Utility in Liquefaction Hazard Evaluation." *Soil Dynamics and Earthquake Engineering* 91: 133-46.

Kramer, Steven Lawrence. (1996) Geotechnical Earthquake Engineering. *Prentice-Hall International Series in Civil Engineering and Engineering Mechanics. Upper Saddle River, N.J.: Prentice Hall*.

Kusaka, T. (2012) Liquefaction characteristics of sand containing non-plastic fines with initial shear stresses: Investigation by Cyclic and Monotonic Loading Torsional Shear Test. *Master's Thesis (in Japanese), Graduate School of Science & Engineering, Chuo University*, Tokyo.

Liu, A. H., Stewart, J. P., Abrahamson, N. A., & Moriwaki, Y. (2001). Equivalent Number of Uniform Stress Cycles for Soil Liquefaction Analysis. *Journal of Geotechnical and Geoenvironmental Engineering*, 127(12), 1017–1026. https://doi.org/10.1061/(ASCE)1090-0241(2001)127:12(1017)

Martin G.R. "Geotechnical aspects of seismic design". *Lecture notes for the course given at the Roseschool,* Pavia, Italy

Mele L., Lirer S. and Flora A. (2019) "The effect of densification on Pieve di Cento sands in cyclic simple shear tests".VII *Convegno Nazionale dei Ricercatori di Ingegneria Geotecnica (CNRIG)*, Lecco.

Jefferies M., Been (2016) *"Soil liquefaction a critical state approach"*. CRC press

Millen, M., Viana da Fonseca, A., Romão, X. (2018). Human-driven Machine-automation of Engineering Research. 9th European Conference on Numerical Methods in Geotechnical Engineering, Porto.

Millen, M., Rios, S., Quintero, J. and Viana da Fonseca, A. (2019). *Soil Dynamics and Earthquake Engineering* (sob revisão)

National Academies of Sciences, Engineering, and Medicine. (2016) "State of the Art and Practice in the Assessment of Earthquake-Induced Soil Liquefaction and Its Consequences." *Washington, DC: The National Academies Press. doi* 1017226: 23474.

Nemat-Nasser, S, and A Shokooh. (1979) "A Unified Approach to Densification and Liquefaction of Cohesionless Sand in Cyclic Shearing." Canadian Geotechnical Journal 16, no. 4: 659-78.

Palmer S. (2006) "Assessment of the Potential for Earthquake Induced Lateral Spreading". *Proceedings of the NZSEE Conference*. Napier. New Zealand. Paper No. 32.

Polito, Carmine P, Russell A Green, and Jongwon Lee. (2008) "Pore Pressure Generation Models for Sands and Silty Soils Subjected to Cyclic Loading." *Journal of Geotechnical and Geoenvironmental Engineering* 134, no. 10: 1490-500.

Rios, S., Millen, M., Quintero, J. and Viana da Fonseca, A. (2019). *Physically-Based Object-Oriented Databases for Geotechnical Engineering*. International Conference on Information Technology in Geo-Engineering, 29 Setembro a 3 de Outubro, Guimaraes, Portugal

Robertson, PK, and CE Wride. (1998) "Evaluating Cyclic Liquefaction Potential Using the Cone Penetration Test." *Canadian Geotechnical Journal* 35, no.3: 442-59.

Schofield, Andrew Noel. (1981) "Dynamic and Earthquake Geotechnical Centrifuge Modelling."

Seed, H Bolton, and Pedro De Alba. (1986) "Use of Spt and Cpt Tests for Evaluating the Liquefaction Resistance of Sands." Paper presented at the Use of in situ tests in geotechnical engineering

Seed, Harry Bolton, and Izzat M Idriss. (1971) "Simplified Procedure for Evaluating Soil Liquefaction Potential." *Journal of Soil Mechanics & Foundations Div*

Seed, Harry Bolton, and Kenneth L Lee. (1965) "Studies of the Liquefaction of Sands under Cyclic Loading Conditions". *Soil Mechanics and Bituminous Materials Laboratory, University of California*

Seed, HB, IM Idriss, F Makdisi, and N Banerjee. (1975) "Representation of Irregular Stress Time Histories by Equivalent Uniform Stress Series in Liquefaction Analyses. Eerc 75-29." *Earthquake Engineering Research Center, University of California, Berkeley*

Sims, John D, and Cristofer D Garvin. (1995) "Recurrent Liquefaction Induced by the 1989 Loma Prieta Earthquake and 1990 and 1991 Aftershocks: Implications for Paleoseismicity Studies." *Bulletin of the Seismological Society of America* 85, no. 1: 51-65.

Standard, British. "Eurocode 8: Design of Structures for Earthquake Resistance." *Part* 1 (2005): 1998-1.

Tokimatsu K. and Seed H.B. (1988) "Evaluation of settlements in sand due to earthquake shaking" *ASCE Journal of Geotechnical Engineering*, ASCE, Vol. 113, No. 8

Wang, Wenshao. (1979) Some Findings in Soil Liquefaction. *Earthquake Engineering Department, Water Conservancy and Hydroelectric Power*

Youd, T Leslie, and Ben L Carter. (2005) "Influence of Soil Softening and Liquefaction on Spectral Acceleration." *Journal of Geotechnical and Geoenvironmental Engineering* 131, no. 7: 811-25.

Youd, T Leslie, and Izzat M Idriss. (2001) "Liquefaction Resistance of Soils: Summary Report from the 1996 Nceer and 1998 Nceer/Nsf Workshops on Evaluation of Liquefaction Resistance of Soils." *Journal of geotechnical and geoenvironmental engineering* 127, no. 4: 297-313.

Youd T.L., Idriss I.M. (1997) Proceedings of the NCEER Workshop on Evaluation of Liquefaction Resistance of Soils, National Center For Earthquake Engineering Research. *State University of New York at Buffalo*

Youd, T. Leslie, Celinda F. Jones, (1991). Liquefaction Hazard Maps for the Portland Quadrangle. Provo, *Utah: Brigham Young University, Dept. of Civil Engineering*

http://www.adbpo.it/download/Sismica/Argini/Present_incorso_opera/11_Aprile_2012_Presentazione_Fioravante_Univ-FE.pdf, 25/08/2019

FIGURES

TABLES